Investigation of Cyclic Combustion Variability & Development of a Predictive Knock Controller

Von der Fakultät Konstruktions-, Produktions- und Fahrzeugtechnik der Universität Stuttgart zur Erlangung der Würde eines Doktor-Ingenieurs (Dr.-Ing.) genehmigte Abhandlung

Vorgelegt von

Nicolas Fajt
aus Ludwigsburg

Hauptberichter:	Prof. Dr.-Ing. M. Bargende
Mitberichter:	Prof. Dr.-Ing. H. Rottengruber
Tag der mündlichen Prüfung:	06.09.2022

Institut für Fahrzeugtechnik
der Universität Stuttgart

2022

Acknowledgements

The presented work was realized during my tenure at the Insitute of Automotive Engineering (IFS) at the University of Stuttgart under the supervision of Prof. Dr.-Ing. Michael Bargende.

First, I would like to acknowledge my gratitude to Prof. Dr.-Ing. Michael Bargende for his guidance and support.

This work would not have been the same without the support from various people at the Institute of Automotive Engineering (IFS) and the Research Institute for Automotive Engineering and Powertrain Systems Stuttgart (FKFS). In particular, I would like to thank my supervisor Dr.-Ing. Michael Grill for guiding my work and his outstanding support during many discussions. I am extremely grateful to all colleagues that contributed to my work through countless fruitful discussions and inspiration, especially M. Hess, S. Welscher and S. Crönert.

I would also like to thank Dr.-Ing. Michael Fischer for leading the working group on the research project "Fast Knocking Prediction for Gasoline Engines" financed by the Research Association for Combustion Engines (FVV) e.V. as well as all the companies that supported the project. My sincere thanks goes to my project partners M. Blomberg and L. Leyens from the Chair of Thermodynamics of Mobile Energy Conversion Systems of the RWTH Aachen University.

Lastly yet importantly, I want to thank my family, friends and everybody who supported me and helped me clear my mind during stressful times.

Böblingen, 12th September 2022 Nicolas Fajt

Kurzfassung

Um einen besseren Einblick in das Klopfphänomen zu erhalten, wurden verschiedene thermodynamische Untersuchungen durchgeführt. Als Erstes wurde der Einfluss von Temperatur- und Gemischinhomogenitäten auf das Auftreten von Klopfen untersucht. Dazu wurde ein neues Trennkriterium eingeführt, welches es erlaubt, klopfrelevante unverbrannte Zellen aus den CFD-Simulationsergebnissen zu isolieren. Dies Kriterium basiert auf der Spezieskonzentration von OH und Iso-Oktan und einem bestimmten Abstand zur Flammenfront. Anschließend wurden zwei unterschiedliche Auswertungen durchgeführt. Zum einen die Auswertung der unverbrannten Zellen mit den global höchsten Temperaturen und fettestem Gemisch und zum anderen eine Auswertung der lokalen Temperatur und der Ladungsbewegung in unmittelbarer Nähe um den Zündkerzenspalt. Aus beiden Untersuchungen ging kein direkter Zusammenhang zwischen Inhomogenitäten und dem Auftreten von Klopfen hervor.

Nachfolgend wurde der Reaktivitätsparameter ε (ursprünglich engl.: reactivity parameter) des Detonationsdiagramms auf eine 0D-Simulationsumgebung angewendet um ε für Einzelarbeitsspiele zum Zeitpunkt der Selbstzündung zu bestimmen. Ziel war dabei ε zu nutzen, um die Klopfneigung vorherzusagen. Um eine realistische Berechnung von ε zu ermöglichen, wurde eine Verteilung der Hotspotgröße mit halbierten Normalverteilungen modelliert. Für die finale Klopfhäufigkeitsberechnung auf Basis der ε-Verteilung wurde ein, im FVV-Projekt „Basismodell Klopfen“ vorgestellter, Berechnungsansatz verwendet. Die Ergebnisse zeigten, dass die allgemeine Klopftendenz zwar vorhergesagt werden kann, jedoch mit geringer Vorhersagegenauigkeit. Dies wurde auf die eingeschränkte Anwendbarkeit des Detonationsdiagramms für Bedingungen nahe der Klopfgrenze sowie fehlenden Validierungsmöglichkeiten für die modellierte Hotspot-Größenverteilung zurückgeführt. In einem weiteren Schritt wurde eine Post-Processing-Methode entwickelt, die es erlaubt, in 3D-CFD-

Simulationen selbstzündende Bereiche (sog. Hotspots) zu identifizieren, die von der fremdgezündeten Flammenfront getrennt sind. Die Anwendung dieser Methode auf die Ergebnisse einer Large-Eddy Simulation mit 100 Motorzyklen ermöglichte die Bestimmung einer Hotspot-Größenverteilung für einen exemplarischen Betriebspunkt. Dazu wurden zwei verschiedene Ansätze verwendet um die Hotspotgröße, auf Basis der identifizierten Hotspotzellen, zu berechnen. Die ermittelte Verteilung deutete auf eine grundsätzliche Eignung des Modellierungsansatzes hin, zeigte aber auch, dass gestreckte Beta-Verteilungen anstelle von halbierten Normalverteilungen besser mit einer realen Verteilung übereinstimmen und genauere Ergebnisse für die Klopfhäufigkeit liefern. Die identifizierte Verteilung an einem einzigen Betriebspunkt war jedoch für eine vollständige Validierung des Ansatzes unzureichend.

Schließlich wurde der Einfluss von Zyklenschwankungen auf die Klopfvorhersage weiter untersucht, indem ein Klopfhäufigkeitsberechnungsansatz verwendet wurde, welcher ebenfalls die zyklischen Variationen einschließt. Für eine vorhersagefähige Anwendung des Berechnungsansatzes, wurden Einzelarbeitsspiele in 0D mit zwei verschiedenen Methoden simuliert, die erhebliche Leistungsunterschiede aufwiesen: Die Modellierung einer Turbulenzpegelverteilung und die Anwendung eines verfügbaren Zyklenschwankungsmodells. Auf Basis der Simulationsergebnisse beider Ansätze war eine präzise Vorhersage der Klopfhäufigkeit möglich. Die Simulationsdauer mit dem Zyklenschwankungsmodell war aufgrund der drastisch reduzierten Anzahl zu simulierender Zyklen und der besseren Integration in das Simulationstool deutlich geringer.

Durch die erfolgreiche Vorhersage der Klopfhäufigkeit konnte ein Regelansatz entwickelt werden der den Zündzeitpunkt basierend auf der Klopfhäufigkeit anpasst. Dieser wurde mittels 0D-Simulationen mit einem konventionellen Klopfregler verglichen. Mit dem neuen prädiktiven Regelungsansatz konnten die zeitliche Variabilität und die Abweichung des Verbrennungsschwerpunkts vom gewünschten Zielwert deutlich reduziert werden. Bei der Simulation instationärer Laständerungen zeigte sich die Bedeutung einer genauen Lastabschätzung und einer genauen Vorhersage aller drei Parameter, die in der Klopfhäufigkeitsvorhersage enthalten sind. Insgesamt ergaben die simulativen Untersuchungen eine maximales Einsparpotential des spezifischen Kraftstoffverbrauchs und der CO_2-Emissionen um jeweils 1% und eine geringe Absenkung der Abgastemperatur.

Abstract

In order to gain better insights into the knocking phenomenon, various thermodynamic investigations have been performed. The influence of temperature and mixture inhomogeneities on knock occurrence was evaluated. Therefore, a new separation criterion was introduced that allows isolation of knock-relevant unburnt cells from CFD simulation results. The separation is based on the species concentration of OH and iso-octane and a specific distance to the flame front. Two different evaluations were performed: one global investigation of unburnt cells with the highest temperatures and lowest air-fuel equivalence ratios and one local investigation of the temperature and charge velocity around the spark plug gap. Both revealed no direct correlation of inhomogeneities to the occurrence of knock.

Subsequently, the reactivity parameter ε of the detonation diagram was applied to a 0D simulation environment to determine ε for single working cycles to predict the knock tendency based on this detonation diagram parameter. To enable a realistic calculation of ε, a hotspot size distribution was modeled based on halved normal distributions. For the knock frequency calculation based on an ε distribution, a calculation approach introduced in the FVV project "Engine knock model" was utilized. The results showed that the general knock tendency could be predicted but with low accuracy. The low accuracy was attributed to a limited applicability of the detonation diagram for conditions close to the knock boundary and the lack of validation possibilities for the modeled hotspot size distribution. Further, a post-processing method was developed to identify auto-igniting volumes (so-called hotspots) separated from the spark-ignited flame front in 3D CFD simulations. Applying this method to Large-Eddy Simulation (LES) results covering 100 engine cycles enabled the determination of a hotspot size distribution for one exemplary operating point. Two different approaches to calculate the hotspot radius based on the determined hotspot cells were employed. The identified distribution indicated a general suitability of the

modeling approach but further revealed that streched beta distributions instead of halved normal distributions agree better with the real distribution and yield more accurate results for the knock frequency. Yet, the identified distribution at a single operating point was insufficient for comprehensive validation of the entire approach.

Lastly, cycle-to-cycle variations were further investigated by applying a knock frequency calculation approach, that includes cyclic variations. For a predictive application of the computational approach, single working cycles were simulated in 0D using two different methods with significant performance differences: Modeling a turbulence level distribution and applying an available cycle-to-cycle variation model. Simulation performance with the cycle-to-cycle variation model was significantly higher due to the much smaller number of cycles that had to be simulated and the better integration in the simulation tool. Based on the simulation results, precise prediction of the knock frequency was possible.

Following the successful knock frequency prediction, a control approach was developed that adjusts the spark timing based on the knock frequency. This new control approach was compared to the conventional knock controller employing 0D simulations. With the new and predictive approach, the variability over time and the deviation of the mean center of combustion to the desired target value at knock-limited conditions could be significantly reduced. Furthermore, simulation of transient conditions revealed the importance of accurate load estimation and accurate prediction of all three parameters in the knock frequency prediction for the subsequent cycle. Overall, the simulative investigations indicated a maximum reduction potential of the specific fuel consumption and the CO_2 emissions by 1%, respectively and a slight decrease of the exhaust gas temperature.

Contents

Acknowledgements **I**

Summary **III**

List of Figures **IX**

List of Tables **XV**

Acronyms **XVII**

Symbols **XIX**

1 Introduction **1**

2 Fundamentals & State of the Art **3**
2.1 Abnormal Combustion - Engine Knock 3
2.2 Engine Knock Control 8
2.3 Resonance Theory and Detonation Diagram 9
2.4 0D Simulation of SI Engines 17
2.4.1 Two-Zone Combustion Modeling 17
2.4.2 Modeling of Cycle-to-Cycle Variations 20
2.4.3 Knock Modeling 22

3 Influence of Temperature and Mixture Inhomogeneities **31**
3.1 Model Sensitivity to Inhomogeneities 31
3.2 Separation of the Unburnt Zone 34
3.3 Evaluation of Inhomogeneities 40

4 Evaluation of Auto-Ignition using the Detonation Diagram **49**

4.1 Application of the Detonation Diagram in 0D Simulations 49
4.2 Identification of Hotspots in CFD Simulation Data 60

5 Influence of Cycle-to-Cycle Variations on the Knock Frequency 75
5.1 Three-Parameter-Approach 75
5.2 Simulation of Single Working Cycles 79
5.3 Results and Discussion of Predicted Knock Frequency . . 84

6 Knock Frequency Based Knock Control 91
6.1 Concept for Predictive Knock Control based on Knock Frequency 91
6.2 Simulative Investigation of Predictive Knock Control . . . 96
6.2.1 Simulation of Conventional / Deterministic Knock Control 96
6.2.2 Simulation of Predictive Knock Control 102
6.3 Evaluation of the Predictive Knock Control Approach . . . 112
6.4 Robustness and Requirements for an Engine Application . 123
6.5 Concept for Knock Sensor Integration 128

7 Conclusions and Outlook 131

A Appendix 135
A.1 Temperature inhomogeneity 135
A.2 Excitation time 139
A.3 Epsilon – constant radius 141
A.4 Epsilon – modeled radius 143
A.5 Simulative controller comparison 145

List of Figures

2.1 Measured cylinder pressure traces of a non-knocking (left) and knocking cycle (right). 4
2.2 Filtered cylinder pressure signal and knock characteristic parameters Knock Amplitude Peak to Peak (KPP) and Maxium Amplitude of Pressure Oscillations (MAPO), in accordance with [15, 16]. 7
2.3 Spark timing progress over time for conventional knock control. 9
2.4 Overview of investigations of the developing detonation regime by various researchers, in accordance with [35]. 15
2.5 Mean and variance of ε for Research Octane Number (RON) (left) and spark timing variation (right), data from [37]. 17
2.6 Schematic structure of the Entrainment model [42, 43]. . . . 18
2.7 Structure of the Cycle-to-Cycle to Variations (CCV) model [42, 50]. 21
2.8 Weighting of results from variations of both parameters of the CCV model to calculate the true variation, schematic view according to [42, 50]. 22

3.1 Effect of a 5% λ and Exhaus Gas Recirculation (EGR) variation on the ignition delay time. 32
3.2 Sensitivity of τ (a) and auto-ignition prediction (b) to a variation of the temperature, λ and the EGR rate. 33
3.3 Temperature rise from unburnt into the burnt zone. 36
3.4 Comparison of maximum temperature and number of cells contained in the unburnt zone for separation by temperature (1500 K threshold) and by chemical species concentration (OH and iso-octane). 37

3.5 Zone separation based solely on chemical species (a) with flame position (b), location of hottest cells following the separation (c) and introdcution of a distance zone (d) – visualized at time step: 725 °CA. 38
3.6 Final zone separation based on chemical species and a distance zone of 2 mm – visualized time step: 725 °CA. 39
3.7 Temperature distribution and average temperature over time – absolute temperatures. 40
3.8 Temperature distribution and progress of 5% mass limit with highest temperatures over time – relative temperatures. . . . 43
3.9 Temperature progress over time of a monitor point and it's location in the combustion chamber. 44
3.10 Temperature and λ inhomogeneity for highest temperatures and lowest λ values: Temperature inhomogeneity for both Operating Point (OP)s with 5% mass limit (a) & (b), OP 1 with 0.5% and 2% mass limit (c) & (d) and λ inhomogeneity for both OPs with 5% mass limit. 45
3.11 Temperature and mixture velocity inhomogeneity for OP 1 for a spherical volume with 1 mm radius around the spark plug gap. 48

4.1 Mean and variance of ε determined from 0D data at the time of auto-ignition for various operating conditions – contained hotspot radius r_0 assumed with 10 mm for all engine cycles in accordance with [66]. 51
4.2 Relation of burnt volume and burnt mass fraction within the Entrainment model and maximum hypothetical radius for a spherical hotspot based on the unburnt volume. 53
4.3 Halved normal distributions to model a hotspot radius distribution – minimum (left) and maximum (right) defined standard deviation to control the maximum ocurring hotspot size. 54
4.4 Unburnt volume (left) and $\Delta\Pi$ (right) at the time of auto-ignition in relation to the knock frequency. 55
4.5 Mean and variance of ε determined from 0D data at the time of auto-ignition for various operating conditions – calculation based on modeled hotspot radius r_0 distribution. 57
4.6 Knock frequency calculated from ε distribution vs. measured knock frequency. 58

4.7 Four-step method to identify auto-igniting hotspots in 3D CFD simulations. 61
4.8 Determination of the knock onset and evaluation range for identification of hotspots, calculation analogous to the method described in [15, 67]. 62
4.9 Evaluation of the flame propagation distance between two time steps of two different engine cycles – cycle one (left) with clear distinction of hotspot cells and cycle two (right) without clear distinction of hotspot cells. 64
4.10 Iterative refinement of potential hotspot cells by evaluation of the minimum distance to the flame front. Hotspot cells with a minimum distance of < 2 mm are re-defined as the flame front. 66
4.11 Final identified hotspot in comparison to the spark ignited flame front. 67
4.12 Hotspot radius distribution of a single OP, determined from 100 simulated engine cycles. Radius determined for a sphere (left) and from maximum distance between two hotspot cells (right). 69
4.13 Modeled hotspot distributions based on a beta distribution and predicted knock frequencies based on ε distribution. 70

5.1 Three-Parameter-Approach for calculation of the knock frequency, according to [15, 67]. 77
5.2 Scaling factor distribution to vary the turbulence level and auto-ignition onset distribution of the simulated Single Working Cycle (SWC)s, according to [69]. 80
5.3 Cylinder pressure of simulated SWCs using a turbulence level distribution in comparison to measured SWCs at 2500 min^{-1} / 16 bar, according to [69]. 81
5.4 Cylinder pressure of simulated SWCs using a CCV-model in comparison to measured SWCs at 2500 min^{-1} / 16 bar, according to [69]. 82
5.5 Calculated knock frequency in comparison to the measured knock frequency for simulation approach using a turbulence level distribution (a) and using a CCV-model, according to [69]. . 85
5.6 Evaluation of the predicted knock frequencies for the simulation approach using a turbulence level distribution (left) and using a CCV-model (right), according to [69]. 86

6.1 Exemplary spark timing adjustment with new knock frequency based knock control concept in comparison to conventional control during stationary operation. 92
6.2 Schematic structure of the new knock frequency based knock controller. 94
6.3 Schematic structure of the new knock frequency based knock controller, according to [77]. 95
6.4 Validation of binomial distribution of knock events by Peyton et al. [25] (left) and measurement data of the single-cylinder engine investigated in this work (right), according to [77]. 98
6.5 Knock event simulation structure, method analogous to [24], according to [77]. 98
6.6 Extrapolation and interpolation method to extend measurement data to higher knock frequencies and higher load resolution – required for the knock frequency interpolation within the knock event simulation. 100
6.7 Calculation of the spark timing for knock frequency based knock control, according to [77]. 105
6.8 Extension of AI_{mean}, σ_{AI} and AI_{Limit} (a)-(c) to consider a ST range that refers to 0.001-100% knock frequency, and exemplary distribution (d) of auto-ignition onsets to explain const. values of the three parameters for STs exceeding the 0.001-100% knock frequency. 107
6.9 Interpolation of AI_{mean}, σ_{AI} and AI_{Limit} to allow knock frequency prediction at engine loads between measured loads. . 110
6.10 Mass Fraction Burnt (MFB)50 over time for conventional and knock frequency based knock control and the underlying calculated knock frequency. Simulation initialized and controller activated at a low knock frequency (top) and at a high knock frequency (bottom), according to [77]. 113
6.11 Initial controller response for controller activation at low knock frequency (left) and high knock frequency (right), according to [77]. 115
6.12 MFB50 distribution for controller activation at low knock frequency (left) and high knock frequency (right), according to [77]. 116

6.13 Comparison of the control response of conventional and knock frequency based knock controller under transient load change, with data from [77]. 118
6.14 Knock frequency prediction during transient load change, according to [77]. 120
6.15 Predicted knock frequency for two cases with different variations of AI_{mean} during a transient load change. 121
6.16 CO_2 emission and fuel consumption reduction potential with knock frequency based knock control. 122
6.17 Comparison of 1 s [77] and 4 s transient load increase indicating the influence of transient duration on knock frequency prediction capability. 125
6.18 Influence of an engine load estimation inaccuracy on the knock frequency prediction, according to [77]. 126
6.19 Knock sensor integration concept. 129

A.1.1 Absolute temperature distribution at the time steps displayed in Figure 3.7. 135
A.1.2 Relative temperature distribution at the time steps displayed in Figure 3.8. 136
A.1.3 Temperature inhomogeneity for 5% mass definition over the entire duration, for OP 1 (top) and OP 2 (bottom). 137
A.1.4 Temperature inhomogeneity for spherical volume around the spark plug gap, varying radii. 138
A.3.1 Mean and variance of ε for ε_{geom} = 10.76 and hotspot radius assumed with 10 mm constant. 141
A.3.2 Mean and variance of ε for ε_{geom} = 11.8 and hotspot radius assumed with 10 mm constant. 142
A.4.1 Mean and variance of ε for ε_{geom} = 10.76 and modeled hotspot radius. 143
A.4.2 Mean and variance of ε for ε_{geom} = 11.8 and modeled hotspot radius. 144
A.5.1 Initial controller response for activation at low knock frequency. 145
A.5.2 Initial controller response for activation at high knock frequency. 146
A.5.3 Comparison for MFB50 distribution for activation at low knock frequency. 147
A.5.4 Comparison for MFB50 distribution for activation at high knock frequency. 148

List of Tables

2.1 Auto-ignition reaction front propagation modes following Bradley et al. [18, 26]. 13

3.1 Covered parameters for investigation of auto-ignition model sensitivity to temperature, air-to-fuel equivalence ration and EGR variation. 34
3.2 Basic engine data and investigated operating conditions. . . 35

5.1 Operating conditions covered by the simulations of single working cycles. 79

A.2.1 Excitation time lookup table – reduced form with limited pressure and temperature resolution and constant $\lambda = 1$, EGR = 4%. . 139

Acronyms

CA	Crank Angle
CCV	Cycle-to-Cycle to Variations
CFD	Computational Fluid Dynamics
CO_2	Carbon Dioxide
DNS	Direct Numerical Simulation
ECU	Electronic Control Unit
EGR	Exhaus Gas Recirculation
EP	Inflammation Phase Duration
FTDC	Firing Top Dead Center
HiL	Hardware in the Loop
IMEP	Indicated Mean Effective Pressure
IMPO	Integral of Modulus of Pressure Oscillations
IVC	Inlet Valve Close

KLSA Knock Limited Spark Advance
KO Knock Onset
KPP Knock Amplitude Peak to Peak

LES Large-Eddy Simulation

MAPO Maxium Amplitude of Pressure Oscillations
MFB Mass Fraction Burnt

NTC Negative Temperature Coefficient

OH Hydroxyl Radical
OP Operating Point

PTA Pressure Trace Analysis

RANS Reynolds-Averaged Navier-Stokes
RMSE Root Mean Square Error
RON Research Octane Number

SF Fluctuating Factor of the Cycle-to-Cycle Variation Model
SI Spark Ignitition
SWC Single Working Cycle

TDC Top Dead Center

Symbols

	Greek Letters	
$\beta_{m,n}$	Bessel Function	-
χ_T	Taylor Length Coefficient	-
ε	Reactivity Parameter of the Detonation Diagram	-
ε_{geom}	Compression ratio	-
ε_{tke}	Rate of Dissipation of Turbulent Kinetic Energy	$m^2\,s^{-3}$
λ	Air-Fuel Equivalence Ratio	-
ν_T	Turbulent Kinetic Viscosity	$m^2\,s^{-1}$
ϕ	Fuel-Air Equivalence Ratio	-
φ	Crank Angle	°CA
χ_{ZS}	Parameter of the Cycle-to-Cycle Variation Model	-
χ_{basis}	Parameter of the Cycle-to-Cycle Variation Model	-
φ_{ZS}	Parameter of the Cycle-to-Cycle Variation Model	-
Π	Parameter of the Knock Model	-
Π_{KB}	Knock Boundary, Parameter of the Knock Model	-
Π_{KO}	Parameter of the Knock Model at Time of Auto-Ignition	-
ρ_{ub}	Density Unburnt Zone	$kg\,m^{-3}$
σ	Standard Deviation	-

σ_{AI}	Standard Deviation of Auto-Ignition Onsets, Parameter of the Three-Parameter-Approach	°CA
τ	Ignition Delay Time	s
$\tau_{1,high}$	High-Temperature Ignition Delay in Low-Temperature Regime of Ignition	s
$\tau_{1,low}$	Low-Temperature Ignition Delay in Low-Temperature Regime of Ignition	s
$\tau_{2,high}$	High-Temperature Ignition Delay in Medium-Temperature Regime of Ignition	s
$\tau_{2,low}$	Low-Temperature Ignition Delay in Medium-Temperature Regime of Ignition	s
$\tau_{3,high}$	High-Temperature Ignition Delay in High-Temperature Regime of Ignition	s
τ_e	Excitation Time	s
τ_{high}	High-Temperature Ignition Delay	s
τ_l	Characteristic Burn-Up Time	s
τ_{low}	Low-Temperature Ignition Delay	s
ξ	Resonance Parameter of the Detonation Diagram	-
ξ_l	Lower Boundary of the Developing Detonation Regime	-
ξ_R	Residual gas fraction exponent	-
ξ_u	Upper Boundary of the Developing Detonation Regime	-

Latin Letters

A	Pre-Exponential Factor	-
a	Acoustic Velocity	$\mathrm{m\,s^{-1}}$

a_0	Acoustic Velocity at 273 K	$\mathrm{m\,s^{-1}}$
A_{fl}	Flame Surface	$\mathrm{m^2}$
AI_{Limit}	Parameter of the Three-Parameter-Approach	°CA
AI_{mean}	Parameter of the Three-Parameter-Approach	°CA
B	Activation Energy Parameter	-
C_1	Temperature Increase Model Parameter	$\mathrm{K^{-3}}$
C_2	Temperature Increase Model Parameter	$\mathrm{K^{-2}}$
C_3	Temperature Increase Model Parameter	$\mathrm{K^{-1}}$
C_4	Temperature Increase Model Parameter	-
C_5	Temperature Increase Model Parameter	K
C_k	Scaling Parameter for the Start Value of the Turbulent Kinetic Energy	-
c_p	Heat Capacity at Constant Pressure	$\mathrm{J\,kg^{-1}\,K^{-1}}$
C_u	Scaling Parameter for the Isotropic Turbulence Speed	-
c_v	Heat Capacity at Constant Volume	$\mathrm{J\,kg^{-1}\,K^{-1}}$
D	Cylinder Diameter / Bore	m
F	Empirical Function of Auto-Ignition Model	-
$f_{m,n}$	Radial Resonance Frequency	Hz
f	Empirical Function of Auto-Ignition Model	-
f_k	Knock Frequency	%
w	Number of Knock Events	-
H_u	Net Caloric Value	$\mathrm{J\,kg^{-1}}$
i	Number of Engine Cycles	-
I_k	Livengood-Wu Integral	-
j	Temperature Regime	-

k	Turbulent Specific Kinetic Energy	$\mathrm{J\,kg^{-1}}$
K_{adv}	Control Gain for Spark Advance	-
K_{ret}	Control Gain for Spark Retardation	-
l	Global Length Scale	m
l_T	Taylor Length	m
m_b	Burnt Mass	kg
m_E	Entrainment Mass	kg
m_F	Mass Flame Zone	kg
m_{ub}	Unburnt Mass	kg
n	Engine Speed	$\mathrm{min^{-1}}$
P	Knock Frequency	%
p	Pressure	bar
P_{calc}	Predicted Knock Frequency	-
$\hat{p}$	High-Pass Filtered Pressure	bar
P_{target}	Target Knock Frequency	-
$P_{tolerance}$	Tolerance Knock Frequency	-
Q_b	Cumulative Burn Rate	J
R	Individual Gas Constant	$\mathrm{J\,kg^{-1}\,K^{-1}}$
r	Radius	m
r_0	Hotspot Radius	m
S	Stroke	m
s_l	Laminar Burning Velocity	$\mathrm{m\,s^{-1}}$
ST	Spark Timing	°CA
T_0	Initial Temperature	K
T	Temperature	K

t	Time	s
ΔT	Relative Temperature	K
ΔT_{sp}	Relative Temperature around Spark Plug Gap	K
t_e	Time at Integration End / Time Until Auto-Ignition Occurs	s
T_{factor}	Pressure-Dependent Temperature Factor of the Auto-Ignition Model	-
T_{grad}	Temperature Gradient	$\mathrm{K\,s^{-1}}$
T_{incr}	Temperature Increase Following Low-Temperature Ignition	K
$T_{incr,fit}$	Modeled Temperature Increase Resulting from Low-Temperature Ignition	K
T_{low}	Temperature at Time of Low-Temperature Ignition	K
T_{ub}	Temperature Unburnt Zone	K
u_a	Imposed Gas Velocity	$\mathrm{m\,s^{-1}}$
u_E	Flame Propagation Speed into the Unburnt Zone (Entrainment Speed)	$\mathrm{m\,s^{-1}}$
u_{Turb}	Isotropic Turbulence Speed	$\mathrm{m\,s^{-1}}$
Δv_{sp}	Relative Vectorial Charge Velocity around Spark Plug Gap	$\mathrm{m\,s^{-1}}$
V_h	Displaced Volume	$\mathrm{m^3}$
v_{ub}	Vectorial Charge Velocity Unburnt Zone	$\mathrm{m\,s^{-1}}$
$x_{R,st}$	Residual Gas Fraction, Burnt Stoichiometrically	-
$x_{ub,bl}$	Unburnt Mass Fraction in the Thermal Boundary Layer	-

Subscripts

adv	Advance
AI	Auto-Ignition
b	Burnt
c	Critical
KB	Knock Boundary
ret	Retard
ub	Unburnt

1 Introduction

One major focus within the development of today's and new generation spark-ignition combustion engines is the continuous reduction of CO_2 emissions. Many different measures are required to comply with the increasingly stringent restrictions. Downspeeding and downsizing by increasing boost pressures and compression ratios are common approaches. However, such efficiency-increasing measures are mostly limited by the occurrence of knock. Operation of the engine as close as possible to the knocking boundary is therefore required to ensure the best possible efficiency. Related to this requirement, conventional knock control has some drawbacks. Due to the large spark timing retardation after knock detection and only slow subsequent advance in smaller increments, if no knock is detected, many cycles are operated at unnecessarily late center of combustions. Predictive instead of conventional reactive knock control enables an optimal center of combustion for operation at the knock limit, increases the efficiency and consequently reduces the fuel consumption and the CO_2 emissions. Hence, the goal is to increase the knowledge on knocking and develop a knock controller that is able to adjust the spark timing predictively. The work is based on the research project [1].

The high complexity and stochastic nature of knock make controller development challenging. Investigations of local auto-ignitions preceding knock are difficult to capture at the test bench and cannot be investigated in two-zone combustion models due to averaging over the entire burnt and unburnt zone. For that reason, in order to identify knock-relevant conditions, 3D CFD simulations are employed to identify temperature and mixture inhomogeneities. Further, the applicability of the detonation diagram in 0D simulations regarding the evaluation of auto-ignitions is investigated. Lastly, the role of combustion cycle-to-cycle variations regarding knocking is evaluated.

Based on the gained insights from these investigations, a predictive knock control system is developed. Two 0D simulation models for conventional and

the new predictive knock control system are employed to identify the emission reduction and efficiency increase potential of the new control approach. Finally, robustness of the new control approach and requirements regarding an engine application are discussed.

2 Fundamentals & State of the Art

2.1 Abnormal Combustion - Engine Knock

A propagating flame that is ignited by an external source describes normal combustion. Engine knock is besides surface ignition one form of abnormal combustion that can occur in gasoline engines [2]. Although surface ignition can also lead to knock, the occurrence is not controllable by alteration of the spark timing, whereas engine knock can be controlled by spark timing variation [2]. Therefore, in [2] engine knock is also referred to as spark knock. Since in this research project only the controllable spark knock is of relevance, in the following, engine knock will refer to the phenomenon of spark knock.

Although there have been multiple theories on the origin of knocking, such as the not further explained theory of an accelerated flame front [3, 4], the most established theory is that knock is caused by an auto-ignition in the unburnt mixture [2, 5, 6, 7]. This spontaneous ignition ahead of the spark ignited flame front causes a rapid release of chemical energy that triggers the propagation of pressure waves through the combustion chamber. Through reflection at the combustion chamber walls, these waves can be amplified and lead to resonance waves in the combustion chamber with substantial amplitudes (Figure 2.1 right side). The radial resonances with the frequency modes according to

$$f_{m,n} = a_0 \sqrt{\frac{T}{273\,\mathrm{K}}} \frac{\beta_{m,n}}{D} \tag{2.1}$$

With:

a_0	Acoustic velocity at 273 K
T	Temperature in the combustion chamber
D	Cylinder diameter
$\beta_{m,n}$	Bessel function, e.g:
	$\beta_{10} = 0.5861$
	$\beta_{20} = 0.9722$
	$\beta_{30} = 1.2197$

contain the majority of energy from the high-frequency pressure oscillations [8, 9]. Without intervention, the pressure waves can result in substantial engine damage, like a mechanical failure (e.g. of the piston rings) due to the high pressure gradients or melting of components due to the increased heat transfer [9]. Therefore, knock controllers (discussed in the following chapter) are applied to avoid knocking during engine operation.

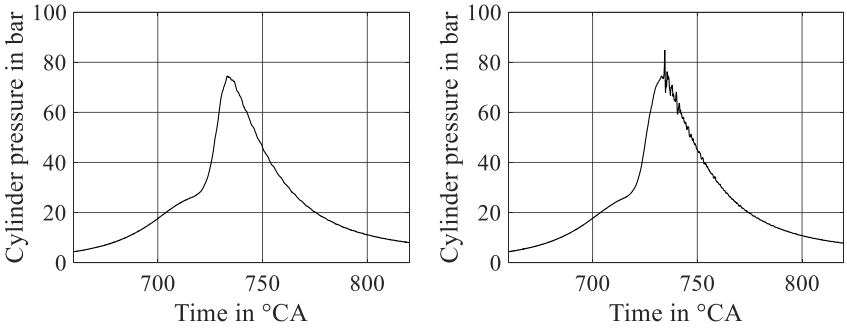

Figure 2.1: Measured cylinder pressure traces of a non-knocking (left) and knocking cycle (right).

For the detection of knock, several different sensors are available. Kiencke and Nielsen give an overview of the different sensors with their advantages and disadvantages in [9]:

Combustion presure sensor (piezoelectric pressure transducer)
Direct measurement of local pressure in the combustion chamber. Knock-induced high-frequency oscillations can be filtered out from the regular combustion pressure with a bandpass. Due to the high accuracy of this sensor type, it is mainly used during engine development and research. High production costs makes this sensor type less attractive for serial application, because the sensors need to be hardened for application in the combustion chamber and integration might be difficult depending on engine head design to enable direct access to the combustion chamber.

Structure borne noise sensor
Measurement of the mechanical vibrations caused by the pressure oscillations. External installation of these sensors allows for a straightforward integration and allows knock detection of up to four cylinders by a single sensor [10]. In combination with low costs and high durability, they are therefore the primary choice for serial production systems [11]. On the downside, the sensor signal contains strong disturbances from the valve train, piston tilting and the crank train, which have to be filtered out to ensure reliable knock detection.

Ion current measurement
Measurement of the intensity of ionization via ion current, which represents the combustion intensity. This type of measurement is integrated into the spark plug and provides in-cylinder measurements without mechanical disturbance from any other components. The integrated design facilitates integration but makes the measurement dependent on the spark plug position. Additionally, only a small volume around the spark plug contributes to the measurement.

Light intensity measurement
The modulation of the intensity of the combustion process caused by the pressure oscillations is associated with a modulation of light intensity and color intensity, which can be optically measured. Accessibility to the combustion chamber is realized by a quartz glass window at the end of the central electrode of the spark plug. The signal is fed through the electrode to a photo transistor via a fiberglass cable. Thereby, as for the ion current measurement, the detection system is integrated into the spark plug and the measurement is independent of mechanical disturbances. However, varying soot coating thickness on the quartz window leads to significant variations of sensitivity.

Depending on the applied detection method, various parameters for knock can be evaluated [11]. Since only measurement data and simulation data from the cylinder pressure were used within this project to detect and measure knock, the presented knock characteristic parameters are confined to the high-frequency analysis of the cylinder pressure signal. From the high-pass filtered pressure signal $\hat{p}$, the knock intensity can be calculated as MAPO, the KPP or the Integral of Modulus of Pressure Oscillations (IMPO):

$$\text{MAPO} = max(|\hat{p}|) \tag{2.2}$$

$$\text{KPP} = max(\hat{p}) - min(\hat{p}) \tag{2.3}$$

$$\text{IMPO} = \frac{1}{\alpha_1 - \alpha_0} \int_{\alpha_0}^{\alpha_1} |\hat{p}| d\alpha \tag{2.4}$$

All three parameters are a measure for the knock intensity. MAPO and KPP (visualized in Figure 2.2) are evaluating the maximum pressure amplitudes that occur and IMPO calculates the energy contained in the high-frequency pressure oscillations. In this project, solely KPP was used to evaluate the knock intensity. In order to calculate not only the knock intensity but also categorize engine cycles in knocking and non-knocking cycles the following, engine speed n dependent threshold definition is utilized:

$$\text{KPP}_{max} = \frac{n}{1000}\,[\text{bar}] \tag{2.5}$$

The general occurrence of knock preceding auto-ignition is mainly dependent on the history of the unburnt mixture (also named endgas) before and during the combustion process. A multitude of parameters influences the ignition delay time and thereby the speed of the chemical reactions that eventually lead to the auto-ignition of the unburnt mixture. Such parameters are e.g. the temperature, pressure, fuel-dependent values like the octane number as a measure for the knock resistance of a fuel blend, air-fuel ratio and the inert gas fraction (e.g. from EGR) [2, 6, 12, 13, 14]. The current trend of downsizing engines and implementing higher compression ratios, which both result in higher cylinder pressures and temperatures shows that limitation by knock is a very present topic for today's engine development.

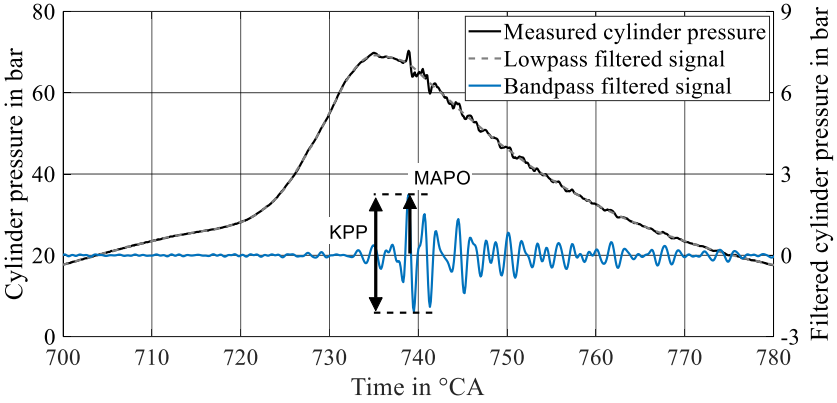

Figure 2.2: Filtered cylinder pressure signal and knock characteristic parameters KPP and MAPO, in accordance with [15, 16].

Besides the various influencing parameters, not every auto-ignition necessarily results in knock [17, 18, 19, 20, 21]. The investigation of test bench data and application of a reaction-kinetics-based auto-ignition model in [15] revealed that auto-ignition occurred in many non-knocking engine cycles. Additional effects such as the cyclic variability of the combustion due to fluctuating turbulence and accompanied inhomogeneities of the mixture further influence the occurrence of knock. This highlights the complexity of the phenomenon due to the involvement and interaction of many global and local variables. In Chapter 2.3 the different results of an auto-ignition are discussed in more detail. Since not all auto-ignitions inevitably lead to knock, many non-knocking engine cycles exist also during stationary engine operation at constant applied operating conditions. For this reason, it is useful to define a further knock characteristic, the knock frequency:

$$f_k = \frac{n_{cycles,knocking}}{n_{cycles,total}} \tag{2.6}$$

The knock frequency represents the relation of knocking to the overall number of cycles and can be determined by measurement of single-working cycles at the test bench and evaluating the KPP value and $\mathrm{KPP_{max}}$ for each cycle. It is further used to define the Knock Limited Spark Advance (KLSA). The KLSA is often also referred to as the knock limit or knock boundary and an important parameter for the operation of the engine, knock control and the development

of new engines. This knock boundary is usually defined as a specific knock frequency or range of knock frequencies, typically between 1% and 10% [22, 23, 24].

2.2 Engine Knock Control

During engine operation, a knock controller constantly adjusts the spark timing to maximize efficiency whilst preventing any mechanical or thermal damage to the engine [10]. To enable the spark timing adjustment, conventional knock controllers require the detection of knock occurrence. Therefore, as mentioned in the previous chapter, in series production primarily structure-borne noise sensors are applied.

The ignition system, which includes the knock control system, calculates the spark timing cylinder-individually for each engine cycle with respect to various operating and ambient conditions. This includes an engine map with fix values that contain the KLSA for stationary operating points across the entire engine map. For conventional knock control, it further includes a closed-loop system with an incremental adjustment based on the detection of knocking events [9]. A comprehensive list of all involved parameters and influences on the ignition angle can be found in [9].

For every non-knocking cycle, the spark timing is advanced by a small increment K_{adv} to shift the operating point closer to the knock limit but also higher thermal combustion efficiencies. If a knocking cycle occurs, the spark timing is retarded by a larger increment K_{ret} to prevent knocking in the next cycle. For a targeted knock frequency P, the controller increments relate to each other according to Equation 2.7 [25].

$$K_{ret} \cdot P = K_{adv} \ (1 - P) \tag{2.7}$$

With this incremental approach, the controller does not settle at the KLSA but cycles in and out of knock resulting in sawtooth-shaped progress of the spark timing over time as illustrated in Figure 2.3. Additionally, due to the larger increments for the spark retardation compared to an advance, the mean spark timing is retarded relative to the desired KLSA because the engine is operated for a longer duration at later spark timings [25].

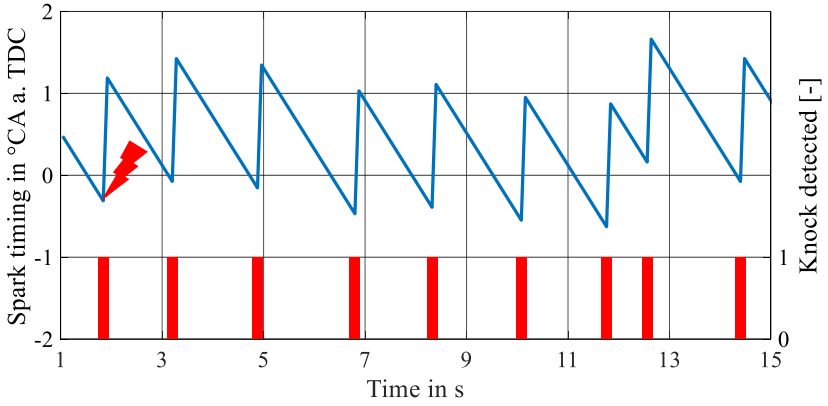

Figure 2.3: Spark timing progress over time for conventional knock control.

Besides the incremental adjustment and the fixed values for the KLSA, a learned ignition angle is part of the spark timing calculation to reduce the response time of knock control at dynamic engine transients [9]. The learned spark timing is stored as an adaptive engine map on the Electronic Control Unit (ECU) and involves a teaching process that is based on the average knock control spark timing from the incremental adjustment. Besides the reduced transient response time, this adaptive map enables the consideration of different fuel blends (e.g. different octane numbers) and aging of an engine within the knock controller. Further details about adaptive knock control are included in [9].

2.3 Resonance Theory and Detonation Diagram

Since not every auto-ignition leads to high-frequency pressure oscillations, various researchers have investigated the possible modes of auto-ignitions. Here, a brief overview of the different investigations will be given and the approach of Bradley et al. [18, 26] will be described in further detail, as it is part of the investigations within this work.

Zeldovich et al. investigated the influence of a temperature gradient in the mixture on the reaction front propagation and the resulting pressure trace for a

one-dimensional case [27, 28]. They found that several transient combustion modes can occur, depending on the induced temperature gradient and that detonation and deflagration are only two of these possible modes. In the context of their work, they also introduced the term "rate of spontaneous propagation" for the velocity of the reaction front of igniting mixture that was found to be dependent on the temperature gradient. Although the results are based on numerical analysis of a simplified one-dimensional model, the different combustion modes were confirmed and extended to cover two dimensions by Koenig and co-workers in [21] who performed schlieren and natural light photography on an optically accessible single-cylinder engine.

Warnatz performed simulations and experiments of hydrogen-oxygen mixture in a hot vessel at various temperatures and pressures to investigate their influence on the ignition behavior of the mixture [6]. He created the so-called p-T explosion diagram for hydrogen-oxygen [6] and hydrocarbon-air mixture at the example of methane-oxygen [29] that contains the ignition limits where certain temperature and pressure combinations either result in no ignition, slow reaction or explosion. He explained the different ignition and combustion modes based on the temperature and pressure-dependent equilibrium of the involved starting, branching and termination reactions.

Kleinschmidt picked up on the combustion modes from Zeldovich to investigate further parameters that are decisive for the occurrence of pressure oscillations. Due to the generally late occurrence of auto-ignition for engine operation at the knock boundary and thus small remaining unburnt volume, he formulated the theory of so-called endgas pockets [19]. For such late phases of the combustion, the turbulent flame already starts to reach the cylinder wall and divides the remaining, thermally inhomogeneous, endgas into separated pockets with different mean temperatures and temperature gradients. Based on his assumption that auto-ignition occurs in such an endgas pocket and with the help of a dimensional analysis, Kleinschmidt found two dimensionless parameters that are beside the pressure decisive for the occurring pressure oscillations.

Similar to Kleinschmidt, Bradley and co-workers [18, 26] developed two dimensionless parameters: the resonance parameter ξ and the reactivity parameter ε that are used to define conditions and boundaries for developing detonations and other possible modes of auto-ignition in the "detonation diagram". The resonance parameter ξ describes a normalized temperature gradient [26] and

follows Zeldovich's combustion mode classification [28] to determine the flame propagation mode after an auto-ignition. The reactivity parameter ε is, as the denotation implies, a measure for the hotspot reactivity and includes the initial hotspot radius r_0.

In an ideal homogeneous mixture, the chemical reaction rates are similar throughout the entire mixture. After the ignition delay time τ has passed, the heat release increases rapidly and the whole mixture ignites at the same time. The resulting pressure rise is rapid and uniform and there are no pressure pulses. This type of auto-ignition, characterized by no spatial gradients is called thermal explosion [26].

However, in Spark Ignitition (SI) engines, no perfect homogeneous conditions exist. Due to varying turbulence, wall temperatures and incomplete mixing with inert gas, local hotspots are developing. These hotspots are regions in the unburnt mixture with increased temperature and increased concentration of active species. If the reaction rates are high enough, the increased chemical reactivity can lead to auto-ignition of a hotspot with a flame propagating out of the hotspot of radius r into the surrounding mixture [26]. The flame, thereby, propagates through the mixture, in which the ignition time τ increases with increasing distance from the hotspot [26]. The propagating flame velocity relative to the unburnt gas imposes a gas velocity u_a that is inversely proportional to the gradient of the ignition delay time τ [18, 26]:

$$u_a = \left(\frac{\partial \tau}{\partial r} \right)^{-1} \tag{2.8}$$

Since the flame propagates into the mixture with lower temperature, Equation 2.8 is related to the temperature gradient $(\partial T_0 / \partial r)$ by [26]:

$$u_a = \left(\frac{\partial \tau}{\partial T_0} \frac{\partial T_0}{\partial r} \right)^{-1} \tag{2.9}$$

According to Zeldovich [28] and Makhviladze and Rogatykh [30], the temperature gradient can reach a critical value $(\partial T_0 / \partial r)_c$, where the imposed velocity u_a matches the acoustic speed a. In this case, the pressure wave caused by the heat release can couple with the auto-ignition front, with reinforcement of both,

releasing pressure spikes and resulting in a developing detonation [18, 26, 28, 30]. This phenomenon is called resonance and from Equation 2.9 [18] given by:

$$u_a = \left(\frac{\partial \tau}{\partial T_0}\right)^{-1} \left[\left(\frac{\partial T_0}{\partial r}\right)_c\right]^{-1} = a \tag{2.10}$$

Yielding the critical temperature gradient [18]:

$$\left(\frac{\partial T_0}{\partial r}\right)_c = \frac{1}{a}\left(\frac{\partial r}{\partial T_0}\right)^{-1} \tag{2.11}$$

The resonance parameter ξ is defined by normalizing the actual initial temperature gradient by this critical gradient [18, 26]:

$$\xi = \left(\frac{\partial T_0}{\partial r}\right)\left(\frac{\partial T_0}{\partial r}\right)_c^{-1} = \frac{a}{u_a} \tag{2.12}$$

With $(\partial T_0/\partial r)$ as the initial boundary condition, chemical resonance of the two waves is reached at $\xi = 1$ [18]. However, the chemical state of the mixture changes due to thermal conduction and diffusion, changing the temperature gradient and ignition delay time gradient. This becomes more pronounced for longer ignition delay times. Therefore, Gu et al. concluded that the development of a detonation is not strictly limited to $\xi = 1$ but is rather an approximate indicator and a certain range of values can be anticipated for a developing detonation [18]. As boundaries for the developing detonation regime, Gu and co-workers introduced a lower ξ_l and upper ξ_u limiting value for the resonance parameter ξ [18]. For $\xi = 0$, the mixture is homogeneous which, as already described, corresponds to a thermal explosion. For $0 < \xi < \xi_l$, the auto-ignition wave is running ahead of the sound wave and there is no causal link between consecutive auto-ignitions. Thus, the gas velocity u_a is unrestricted and can reach large values, which can theoretically exceed the speed of light [18]. When ξ exceeds the upper limit $\xi > \xi_u$, the gas velocity u_a decreases below the acoustic velocity. If the u_a further decreases below the laminar burning velocity s_l flame propagation is driven by molecular transport and subsonic deflagration prevails. The five different propagation modes of the auto-ignition front according to Bradley and co-workers [18, 26] are summarized in Table 2.1:

Table 2.1: Auto-ignition reaction front propagation modes following Bradley et al. [18, 26].

Boundaries of ξ	Propagation mode
$\xi = 0$	Thermal explosion
$0 < \xi < \xi_l$	Supersonic auto-ignitive deflagration (recation front ahead of sonic wave)
$\xi_l \leq \xi < \xi_u$	Developing and developed detonation
$\xi_u \leq \xi < \frac{a}{s_l}$	Subsonic auto-ignitive deflagration
$\xi \geq \frac{a}{s_l}$	Laminar burning deflagration at s_l

In [18, 26] Bradley, Gu and co-workers performed zero- and one-dimensional simulations to investigate the different propagation modes. The zero-dimensional simulations with homogeneous mixture were performed to compute the ignition delay times τ and the excitation times τ_e. Following Lutz et al. [31], the excitation time marks the beginning of rapid energy release to the point of maximum power and was therefore defined as the time duration between 5% and maximum heat release. From the results, they calculated the critical temperature gradient, $(\partial T_0/\partial r)_c$, and found a temperature dependence that suggests that at lower temperatures a smaller temperature gradient can initiate developing detonation, whereas for higher temperatures higher temperature elevations are required.

Auto-ignition of a hotspot was simulated by directly solving the conservation equations in one-dimensional spherical symmetric form in [32, 33] to investigate temperature, pressure, gas velocity and the reaction front wave speed [26]. Three different hotspot sizes (1 mm, 2 mm, 3 mm) and different initial temperature gradients were analyzed. In the center of the hotspot a temperature elevation ΔT_0 is initialized that decreases linearly to the temperature T_0 of the surrounding mixture at the edge of the hotspot, to create a temperature gradient. Detailed reaction chemistry was applied to predict the auto-ignition and combustion of stoichiometric hydrogen-air and syngas-air (H_2-CO-air) mixtures.

From their studies [18, 26], Bradley and co-workers found that developing detonation can occur from small temperature elevations starting with $T_0 = 0.5$ K.

They further observed that thermal conduction and diffusion during the induction time significantly reduce the effective ξ. One simulation e.g., with an initial resonance parameter at $\xi = 1$, resulted in a thermal explosion after a supersonic auto-ignitive deflagration. Therefore, the initial resonance parameter was increased and developing detonation could be observed for simulations with initial values of $\xi = 3$ and $\xi = 10$. Another important finding was that the resonance parameter alone is insufficient to characterize the limits of developing detonation and a second parameter, containing how fast chemical energy can be loaded into the acoustic wave, is required. Only if the heat release following an auto-ignition can feed into the pressure wave, they can reinforce and form resonance. The time for the heat release is thereby characterized by the excitation time τ_e and the duration of the acoustic wave traveling through the hotspot is given by r_0/a, resulting in the definition of the reactivity parameter ε:

$$\varepsilon = \frac{r_0}{a\tau_e} \tag{2.13}$$

Bradley et al. [26] merged and generalized their simulation results into the detonation diagram (Figure 2.4a) which defines the region for developing detonation, limited by the lower and upper boundaries ξ_l and ξ_u as functions of ε. Since the introduction of the detonation diagram, several researchers have investigated its applicability for different fuels and specific phenomena such as super knock [34]. Many of these results were summarized by Netzer in [35] and are shown in Figure 2.4.

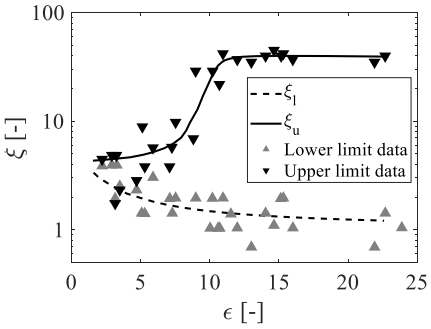

(a) Data from Bradley et al. [26].

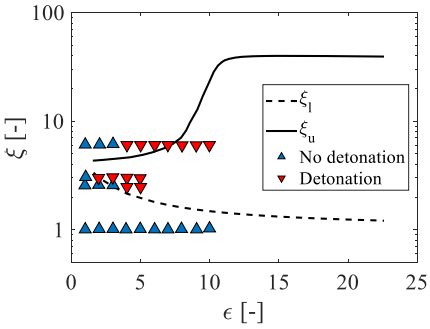

(b) Data from Peters et al. [36].

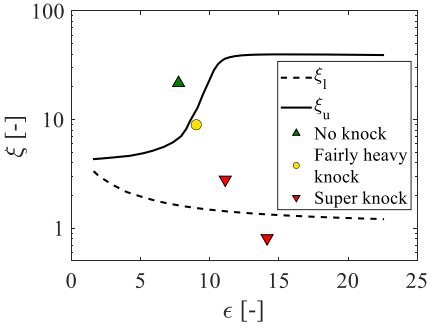

(c) Data from Kalghatgi [34].

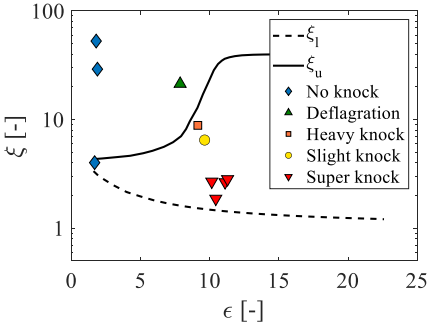

(d) Data from Bates et al. [17].

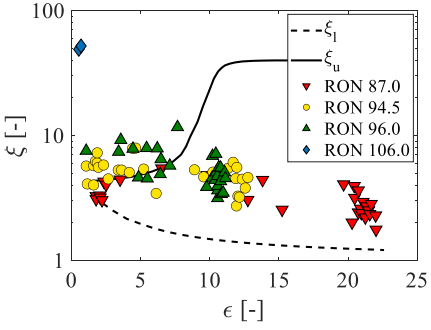

(e) RON variation QD model, data from Nether et al. [37].

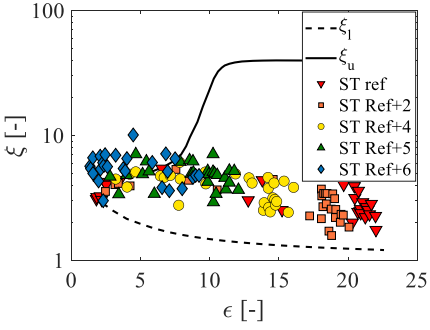

(f) Spark timing *ST* variation QD model, data from Netzer et al. [37].

Figure 2.4: Overview of investigations of the developing detonation regime by various researchers, in accordance with [35].

Peters et al. [36] confirmed the limits of the detonation peninsula as well as the minimum reactivity parameter $\varepsilon = 1.6$ for n-heptane and iso-octane fuel (Figure 2.4b). With a more pronounced low-temperature chemistry and negative temperature coefficient[1], these fuels differ from the fuels investigated by Bradley [26] and are more likely to develop an auto-ignition [35]. Therefore, Peters et al. [36] concluded that the ignition of a hotspot that possibly results in a developing detonation is driven by the high-temperature regime and the low-temperature regime has already been passed before the auto-ignition with significant heat release occurs. The similar high-temperature chemistry found for all fuels is consequently the reason for the fuel independence of the transition boundaries in the detonation diagram [36].

Kalghatgi and Bradley [34] experimentally investigated super knock (Figure 2.4c). To enable the calculation of ξ and ε a hotspot size of $r_0 = 5\,\mathrm{mm}$ and a temperature gradient of $(\partial T_0/\partial r) = -2\,\mathrm{K\,mm^{-1}}$ have been assumed. Ignition delay times and excitation times were calculated for the surrogate fuel at the thermodynamic conditions prevailing at auto-ignition onset. This way, they could trace the transition from a normal non-knocking cycle to super-knock in the detonation diagram. Bates et al. [17] contributed further LES results covering different regimes in the detonation diagram and further gasoline fuels (Figure 2.4d).

Besides all efforts to apply the detonation diagram to simulation data from Direct Numerical Simulation (DNS), LES and measurement data, Netzer and co-workers [35, 37] shall be mentioned, who applied the calculation of the detonation parameters ξ and ε to a quasi-dimensional engine model [38, 39]. In this model, the combustion chamber is discretized into a finite number of non-dimensional particles between which stochastic mixture processes are applied. By collecting the particles that contribute to the high-temperature heat release during an auto-ignition and treating them as one kernel, Netzer et al. enabled the calculation of relevant parameters such as the hotspot radius r_0, assuming a spherical kernel as well as the temperature elevation ΔT_0 and resulting

[1] The Negative Temperature Coefficient (NTC) range is a temperature range in which the ignition delay time increases for increasing temperatures, whereas it usually decreases for increasing temperatures. A negative temperature coefficient in the mid temperature range is characteristic for gasoline fuels.

temperature gradient ($\partial T_0/\partial r$), based on the maximum particle temperature. With this approach, a sensitivity study with a large number of engine cycles at different spark timings and with different RON could be performed (see Figures 2.4e and 2.4f). The results confirmed an increasing knock strength and pressure gradients for advanced spark timings and reduced surrogate RON. Evaluation of the distribution of ξ and ε further showed a strong correlation between the variance of ε and the knock tendency (ref. to Figure 2.5).

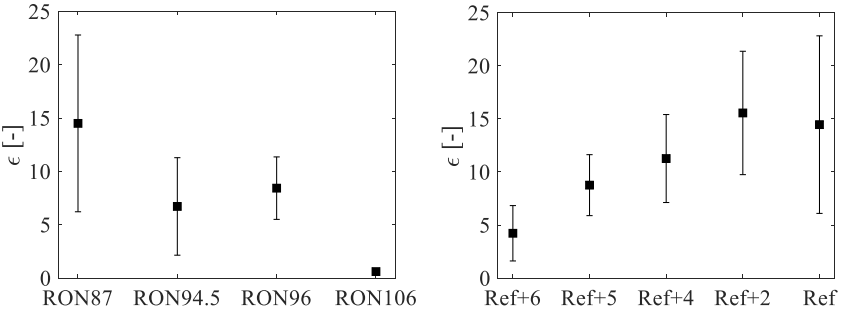

Figure 2.5: Mean and variance of ε for RON (left) and spark timing variation (right), data from [37].

2.4 0D Simulation of SI Engines

2.4.1 Two-Zone Combustion Modeling

For 0D combustion modeling, in this work, the Entrainment model is utilized [40, 41]. Whereas Vibe combustion provides an empirical modeling approach, the Entrainment model provides a phenomenological approach for quasi-dimensional combustion modeling. The general structure of this combustion model will be provided (ref. to Figure 2.6), as it is not only used for the 0D simulations but is also the basis of the utilized cycle-to-cycle variation model and the knock model.

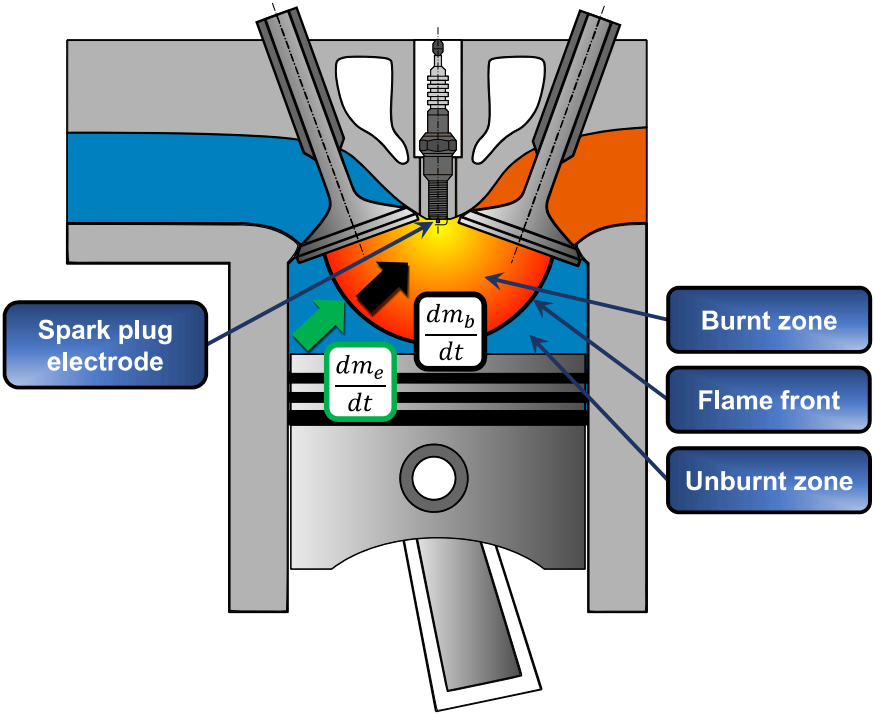

Figure 2.6: Schematic structure of the Entrainment model [42, 43].

The flame propagates with a speed normal to its surface and in a hemispherical shape. With a central spark plug position, this would lead to unrealistic heat release rates since in reality the flame propagation deviates from the perfect sphere. For this reason, in the Entrainment model, the spark plug position should be slightly offset from the center of the combustion chamber, even if in reality a central spark plug is applied. The slight offset leads to an unsymmetrical flame propagation with more realistic heat release rates.

The entire thermodynamic system of the combustion chamber is divided into three systems: the unburnt zone, the burnt zone, and the flame front. The specific properties of the flame front are not calculated but the flame is added to the unburnt zone, hence making it a two-zone computation.

Propagation of the flame is calculated as the sum of the laminar flame speed s_l and the isotropic turbulence speed u_{Turb}:

$$u_E = u_{Turb} + s_l \tag{2.14}$$

Consequently, considering the flame surface A_{fl}, and the density of the unburnt zone ρ_{ub}, the mass brought into the flame zone is:

$$\frac{dm_E}{dt} = \rho_{ub} \cdot A_{fl} \cdot u_E \tag{2.15}$$

This mass is also referred to as the entrainment mass and together with the mass flow into the burnt zone, decisive for the flame zone mass. With the additional characteristic burn-up time, the burn rate is yielded by Equation 2.16. The burn-up time τ_l (Equation 2.17) describes the duration for laminar combustion of a turbulent eddy with the size of the Taylor length l_T (Equation 2.18), which in turn is dependent on the global length scale l, the turbulence speed u_{Turb}, and the turbulent kinetic viscosity ν_T. The factor χ_T is set to 15, following [2].

$$\frac{dm_b}{dt} = -\frac{dm_{ub}}{dt} = \frac{dQ_b}{d\varphi} \cdot \frac{1}{H_u} \cdot \frac{d\varphi}{dt} = \frac{m_F}{\tau_l} \tag{2.16}$$

$$\tau_l = \frac{l_T}{s_l} \tag{2.17}$$

$$l_T = \sqrt{\chi_T \cdot \frac{\nu_T \cdot l}{u_{Turb}}} \tag{2.18}$$

The integral length scale is a measure of the largest eddies in the combustion chamber. It is determined as the diameter of a sphere with a volume corresponding to the combustion chamber's volume. Under the assumption of isotropy at the end of compression [40], the turbulence speed u_{Turb} is calculated by:

$$u_{Turb} = \sqrt{\frac{2}{3}k} \tag{2.19}$$

The turbulent kinetic energy k is determined by a separate turbulence model. Therefore, originally, a k-ε_{tke} model [44, 45] was used. In this model, the start value of the turbulent kinetic energy can be adjusted by the parameter C_k, to calibrate the turbulence model to a specific engine. By now, another turbulence [46, 47] is implemented in the Entrainment model. This model differs slightly in terms of calibration, as the start value of the turbulent kinetic

energy is determined phenomenologically and the calibration parameter C_u allows adjustment of the turbulence speed u_{Turb}.

The remaining unknown, the laminar flame speed, is implemented according to Heywood [2] in slightly modified form [40]:

$$s_l = s_{l,0} \cdot \left(\frac{T_{ub}}{298\,\mathrm{K}}\right)^{\alpha} \cdot \left(\frac{p}{1\,\mathrm{bar}}\right)^{\beta} \cdot \left(1 - 2.06 \cdot x_{R,st}{}^{\xi_R}\right) \tag{2.20}$$

$$\alpha = 2.18 - 0.8 \cdot (\phi - 1) \tag{2.21}$$

$$\beta = -0.16 + 0.22 \cdot (\phi - 1) \tag{2.22}$$

$$s_{l,0} = 0.305 - 0.549 \cdot (\phi - 1.21)^2 \tag{2.23}$$

It has to be noted, that similarly to the turbulence model, a new flame speed model has been developed [48, 49]. The new model was developed based on reaction kinetics calculations and yields more accurate results for the laminar flame speed over a wider range of boundary conditions.

2.4.2 Modeling of Cycle-to-Cycle Variations

Stochastic variations of the combustion are a typical effect for combustion engines. The CCV model, developed by Wenig in [50, 42], provides a phenomenological simulation model to predict these cyclic variations over the entire engine map. The model contains three calibration parameters and is based on the assumption that the cycle-to-cycle variations can be modeled by alteration of parameters available in the previously introduced combustion model (e.g. the turbulence level). The general structure of the model is shown in Figure 2.7.

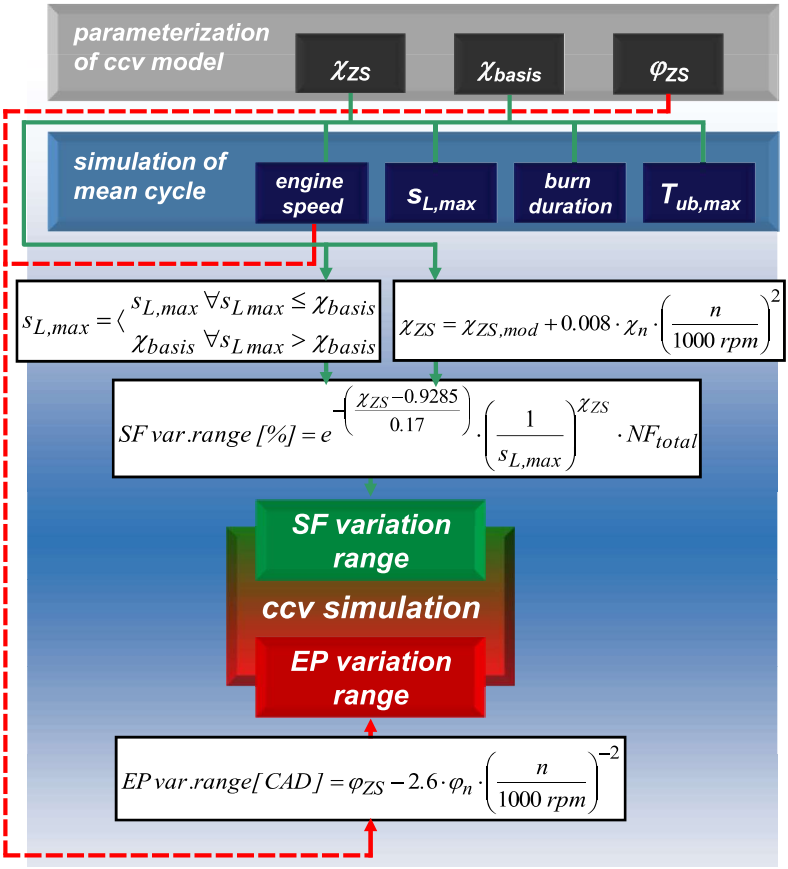

Figure 2.7: Structure of the CCV model [42, 50].

Since charge dilution and the combustion position were identified as the main influences on the cyclic variations, they are modeled by an individual variation of a fluctuating factor SF and the inflammation phase duration EP. The fluctuating factor is applied to the laminar flame velocity altering the flame propagation speed and the inflammation phase duration alters the initial 0-10% burn duration by variation of the spark timing. Two main calibration parameters (χ_{ZS} and φ_{ZS}) are contained, which are used to calculate the respective variation ranges. Differentiated influence of both parameters allows individual and separate

calibration of χ_{ZS} and φ_{ZS}, making the model very user-friendly. As shown in Figure 2.8, the results (e.g. the Indicated Mean Effective Pressure (IMEP)) of each variation are individually weighted to determine the overall cycle-to-cycle variations from a limited number of variation simulations. Commonly, 15 different variations are performed, with the number being adjustable by the user.

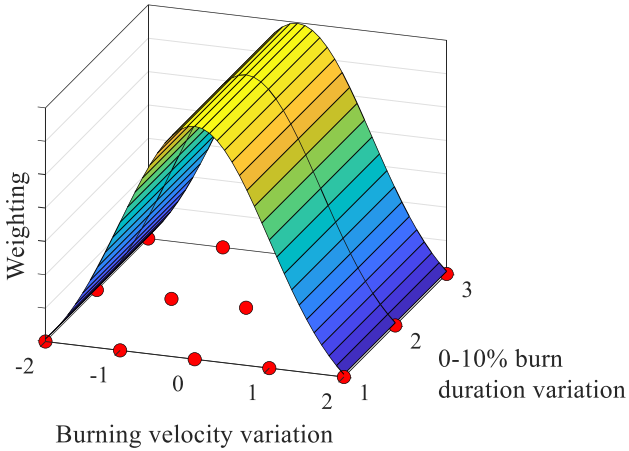

Figure 2.8: Weighting of results from variations of both parameters of the CCV model to calculate the true variation, schematic view according to [42, 50].

The third parameter χ_{basis} affects modeling at intermediate loads, where variation of the charge dilution and combustion position are at minimum degree. Consequently, due to usually negligible EGR-rates and optimal center of combustion, the cyclic variations are small at these operating conditions compared to full load or lower part load with high EGR-rates. Therefore, the third parameters is less important and generally does not have to be calibrated.

2.4.3 Knock Modeling

Knocking is a result of an auto-ignition. Therefore, although not every engine cycle with auto-ignition leads to pressure oscillations, it is crucial for

knock models to predict the occurrence of auto-ignition accurately. Different approaches exist in order to calculate or model the chemical reactions in the unburnt zone that lead to auto-ignition:

- Detailed reaction kinetic mechanisms
- Reduced reaction kinetic mechanisms
- Phenomenological modeling

Detailed reaction kinetics provide the most comprehensive set of chemical species and elementary reactions. Thus, their application to zero- or quasi-dimensional simulations or 3D CFD simulation yields the most accurate results of the real chemical properties. However, the large number of species and reactions in detailed mechanisms and the associated high computational effort make them mostly ineligible for application in 3D CFD simulations. Within zero- or quasi-dimensional simulations like in [14, 22, 51, 52, 53, 54], detailed mechanisms can be used to investigate chemical species, thermodynamic states and physicochemical interactions. In reduced form, the mechanisms still achieve high accuracy while reducing the computational effort, which makes them more suited for the application in 3D CFD simulations. Yet, the typical simulation durations are still magnitudes higher compared to 0D engine simulations and phenomenological models. Such phenomenological models are not based directly on chemical species and elementary reactions but use empirical correlations to calculate the real physical or chemical behavior as realistic and accurate as possible. This approach allows for the lowest computational effort and is therefore well suited for application in 0D engine simulations.

Phenomenological 0D Auto-Ignition Modeling

The auto-ignition model used within the 0D simulations of this project is the state-of-the-art phenomenological model developed by Fandakov [14, 22, 52] and refined by Hess [15, 16]. A comprehensive list of previous knock models is given in [14], but shall not be discussed further in this project. Like many of the other available knock models, the introduced model is based on the evaluation of the chemical state of pre-reactions in the unburnt zone by calculating an integral

developed by Livengood and Wu [55], which is also known as Livengood-Wu integral:

$$1 = \int_0^{t_e} \frac{1}{\tau} dt \tag{2.24}$$

With:

t_e Time at integration end / Time until auto-ignition occurs

τ Ignition delay time of the unburnt mixture at current boundary conditions

As Equation 2.24 implies, integrating the inverse of instantaneous ignition delay time values provides a dimensionless value, representing the state of the chemical pre-reactions. Therefore, the ignition delay time has to be known at every integration step. Integration usually starts at Inlet Valve Close (IVC) or 90 °CA before Firing Top Dead Center (FTDC) [14, 56]. At the time step t_e, when the integral value reaches one, auto-ignition occurs.

Since the ignition delay time for gasoline fuel-air mixtures has a pronounced NTC range, under specific operating conditions, they ignite in two stages [14, 22, 54, 56, 57]. That means a small heat release occurs before the actual high-temperature ignition accompanied by the large heat release takes place. The first ignition stage is therefore also referred to as low-temperature ignition or "cool-flame". Although Livengood and Wu proposed a separate integration for each stage in case of a two-stage ignition already in 1955 [55], Fandakov was the first to implement it in a knock model [14, 22]:

$$I_{k1} = \int_0^{\tau_{low}} \frac{1}{\tau_{low}} dt \tag{2.25}$$

$$I_{k2} = \int_{\tau_{low}}^{\tau_{high}} \frac{1}{\tau_{high}} dt \tag{2.26}$$

The first integral I_{k1} models the low-temperature ignition. If its value reaches one, the low-temperature heat release occurs and the second integral starts. The time of the low-temperature ignition τ_{low} is, therefore, the upper limit of the first integral and the lower limit of the second integral. The second integral

I_{k2} models the high-temperature ignition and the integration end time, when its value reaches one, marks the auto-ignition onset of the mixture, which may induce the pressure oscillations. The integration of the second stage starts at a value of 0.3, whereas the first stage starts at zero, to consider the progress of the pre-reactions during the first ignition stage [14, 22]. Besides the increased starting value, the temperature increase due to the low-temperature ignition T_{incr} is considered within the calculation of the ignition delay time τ_{high} of the second integral. This is especially important, due to the exponential temperature dependence of the ignition delay time [14].

In order to develop a reduced calculation approach for τ_{low}, τ_{high}, and T_{incr}, Fandakov performed zero-dimensional simulations in an adiabatic reactor with a detailed reaction mechanism applied. This allowed accurate prediction of these parameters and their sensitivity/dependence on the variation of temperature, pressure, EGR rate, lambda and composition of the surrogate fuel. As shown in detail in [14, 52], the three parameters are evaluated based on the temperature gradient. The low-temperature ignition delay time τ_{low} is defined as the time when the temperature gradient reaches its maximum before the auto-ignition. Following [14, 52], The high-temperature ignition delay time τ_{high} is defined as the time when the temperature gradient reaches a threshold of $25\,\mathrm{K\,\mu s^{-1}}$. The temperature increase T_{incr} resulting from the low-temperature ignition is defined as the difference between the temperature at minimum temperature gradient $\min(T_{grad})$ between the two ignition stages and the temperature at simulation start.

For the phenomenological calculation of the ignition delay times of the low- and high-temperature ignition τ_{low} and τ_{high} Fandakov used the 3-domain approach, proposed by Weisser [58]. Here, the overall temperature range of the ignition delay times is divided into a low-, medium- and high-temperature regime, each modeled by an Arrhenius-type equation. With the low-temperature ignition characterized solely by the low- and medium-temperature regime and the high-temperature ignition characterized by all three regimes, the ignition

delays are calculated as follows:

$$\frac{1}{\tau_{low}} = \frac{1}{\tau_{1,low} + \tau_{2,low}} \tag{2.27}$$

$$\tau_{j,low} = A_{j,low} \cdot e^{\left(\frac{B_{j,low}}{T}\right)} \tag{2.28}$$

$$A_{j,low}, B_{j,low} = f_{1,2}(p, \lambda, \mathrm{EGR}, surr.comp.fracs.)$$

$$\frac{1}{\tau_{high}} = \frac{1}{\tau_{1,high} + \tau_{2,high}} + \frac{1}{\tau_{3,high}} \tag{2.29}$$

$$\tau_{j,high} = A_{j,high} \cdot e^{\left(\frac{B_{j,high}}{T}\right)} \tag{2.30}$$

$$A_{j,high}, B_{j,high} = F_{1,2}(p, \lambda, \mathrm{EGR}, surr.comp.fracs.)$$

with:

j	Temperature regime
A	Pre-exponential factor
B	Activation energy parameter
f,F	Empirical functions

In comparison to simple Arrhenius-type equations, Equations 2.28 and 2.30 show that the activation energy B within the exponential function is not a constant but similar to the pre-exponential factor A dependend on the boundary conditions. This allows fitting to very complex shapes and therefore contributes to the high accuracy of this calculation method. Fandakov showed in [14, 22, 54] that with the 3-domain approach, the ignition delay times can be calculated with significantly higher accuracy compared to models based on a single Arrhenius-type equation for the entire temperature range. This applies particularly to fuels with a pronounced negative temperature coefficient behavior, such as gasoline.

The temperature increase T_{incr} is modeled as a multiple of 100 of the sum of itself and the temperature at the time of the low-temperature ignition T_{low} according to:

$$T_{incr} = T_{incr,fit} \cdot 100 - T_{low} \tag{2.31}$$

T_{incr} is not directly modeled to reduce the sensitivity of the calculation results to model errors and to achieve better numerical stability [14, 22, 54]. Moreover, to achieve a high modeling accuracy for $T_{incr,fit}$, a quartic polynomial is used:

$$T_{incr,fit} = C_1 \left(\frac{T_{low}}{100}\right)^4 + C_2 \left(\frac{T_{low}}{100}\right)^3 + C_3 \left(\frac{T_{low}}{100}\right)^2 + C_4 \left(\frac{T_{low}}{100}\right) + C_5 \quad (2.32)$$

Details about the parameters and constants of the Equations 2.25 to 2.32 can be found in [14, 52]. Fandakov showed in [14, 22, 52, 54] that this two-stage auto-ignition model significantly improves the prediction quality compared to previous models.

Hess [15, 16] utilized the two-stage auto-ignition model and even further increased the prediction accuracy by implementing a pressure-dependent temperature factor T_{factor}. This temperature factor is an empirical parameter to adjust the input temperature of the auto-ignition model for temperatures above 700 K according to Equation 2.33 and has to be calibrated for each engine.

$$T_{ub} = T_{ub} \cdot (1 + T_{factor}) \quad (2.33)$$

Although empirically based, this parameter is useful from a physical point of view. Since the input temperature in the auto-ignition model is the mean unburnt temperature, local inhomogeneities are not accounted for. With the temperature factor, effects such as inhomogeneities but also inaccuracies of measured ignition delay times or model inaccuracies of the zero-dimensional reactor simulations with detailed reaction kinetics can be accounted for. Hess demonstrated that a small adjustment of max. 20 K is sufficient to increase the prediction quality for a large variation of boundary conditions [15, 16].

Evaluation of Auto-Ignition – 0D Knock Criteria

Knock criteria are employed to evaluate if knock occurs, following an auto-ignition. This is required, since as described in Chapter 2.1 and 2.3, not every auto-ignition necessarily results in knock. However, for the engine operation, an evaluation if the KLSA has been reached is more relevant than the evaluation of every single working cycle. Therefore, knock criteria such as [22, 23, 59, 60,

61] aim at a binary classification if the knock boundary, typically defined as a range of knock frequencies (as in [15, 52]), is exceeded by evaluating the mean working cycle of an engine operating point. Such mean working cycles are an average of many single working cycles at similar boundary conditions, thus containing information of knocking and non-knocking single working cycles. It is important to note that this also means that the prevailing cycle-to-cycle variations of an operating point are not directly accounted for in the knock criterion, due to the averaging.

A large number of knock criteria (summarized in [14]) are based on the assumption that no knock can occur after a specific amount of the mixture is burnt, due to the small remaining unburnt mass. This translates to a limit of MFB, constant for all operating conditions. If auto-ignition occurs after this specified MFB threshold, it does not result in knock.

Investigations of Fandkov [14, 52] and Hess [15] have revealed that the assumption of a constant mass fraction burnt threshold is wrong and the maximum mass fraction burnt at which knock can still occur is depending on the operating conditions. For that reason, following Steuers [62], Fandakov developed a new knock criterion that evaluates the amount of unburnt mass inside the thermal boundary layer of the cylinder wall at the time of the auto-ignition [14, 22]. Since auto-ignition usually occurs at late timings measured by the amount of mass that is already burnt, a substantial amount of unburnt mixture is within the thermal boundary layer close to the cylinder wall [14, 22, 52]. The lower temperature and thus higher ignition delay times close to the cylinder wall has a cooling effect on the still unburnt mixture that suppresses knock. Therefore, no knock occurs or more specifically the knock boundary is not yet reached when the amount of unburnt mixture at the time of the auto-ignition exceeds a critical amount $x_{ub,bl}$ [14, 22]. This threshold parameter has to be calibrated once for an engine and was expected to be constant for all operating conditions [14, 22]. However, Hess found in his investigations that under the assumption of a constant $x_{ub,bl}$, the prediction accuracy of this knock criterion is dependent on the center of combustion [15, 23]. Hess also noted that there are operating points below the knock boundary with an extremely early auto-ignition onset, where less than 5% of the unburnt mass was located in the thermal boundary layer. In these cases, with such a low amount of mass in the thermal boundary, it seems physically not plausible that knocking is suppressed by the cooling effect of the wall [15, 23].

With the purpose to develop a new knock criterion, Hess compared operating points with extremely early and late auto-ignition onset. This revealed that their pre-reaction states I_k at start of combustion, calculated from the two-stage auto-ignition model, differs significantly. Thus, he followed that the pre-reaction state of the unburnt mixture has an important influence on the time when auto-ignition occurs and the mass fraction that is burnt at this time [15, 23]. Investigating only operating points at the knock boundary (operating points with 4-10% knock frequency), Hess found two parameters with a distinct relation to the pre-reaction state at the start of the combustion:

- The time when auto-ignition occurs (CA) – derived from °CA as unit for the time.
- One of the two dimensionless parameters developed by Kleinschmidt [19], that in combination with pressure describes the pressure oscillations resulting from an auto-ignition (Pi).

Based on his findings, Hess developed two new knock criteria (CA-Criterion and Pi-Criterion), which calculate the knock boundary for an engine as the time of auto-ignition or Pi as a function of the pre-reaction state at the time of combustion start [15, 23, 61]. Both knock criteria have to be calibrated at a minimum of two operating points and have shown very high prediction accuracy for a large variety of operating conditions.

3 Influence of Temperature and Mixture Inhomogeneities

3.1 Model Sensitivity to Inhomogeneities

Usually, 0D knock models such as the ones presented in Chapter 2.4.3 are based on mean values as input parameters. This originates from the underlying combustion models that are typically used. The Entrainment model [40, 41], which is also used in this work, models the combustion as a two-zone thermodynamic system. This way, for each, the burnt and unburnt zone, mean values e.g. of the temperature are calculated. These values are subsequently used as input for the knock model and therefore, no inhomogeneities are accounted for. Still, different approaches exist which include the inhomogeneities. Fandakov applied a constant temperature offset to account for locally elevated mixture temperatures [14, 22]. The variable temperature adjustment by Hess [15, 16], introduced in Chapter 2.4.3, provides a temperature correction depending on the cylinder pressure. Yet, both approaches are empirically based and have to be calibrated for each specific engine. Therefore, the aim of evaluating inhomogeneities is to specifically investigate their influence on the occurrence of knock to get a better understanding of the fundamental phenomenon and to provide useful information for the improvement of the knock model.

3D CFD simulations are a convenient tool to investigate local phenomena that are difficult to capture on an engine test bench or that are not contained in typical 0D/1D models. To model the complex turbulent structures and mixing effects in the combustion chamber realistically, a high resolution of the numerical grid and small time steps are required. LES provide a good compromise between accuracy and the required computational effort. Within LES large-scale turbulence such as tumble are modeled directly and therefore more realistically than in Reynolds-

Averaged Navier-Stokes (RANS) simulations. Simultaneously, LES maintain significantly lower computational effort compared to DNS, where all small-scale turbulences are directly solved, which requires very high grid resolution and extremely small time steps. For this reason, results from large-eddy simulations are analyzed.

Prior to investigating the large-eddy simulations regarding the inhomogeneity, a sensitivity analysis of the auto-ignition model shall give more insight into the influence of different input parameters on the auto-ignition prediction. Compared are the temperature of the unburnt zone T_{ub}, the air-fuel equivalence ratio λ and the EGR rate. Further parameters such as surrogate components are not included and therefore the fuel blend itself is assumed fully homogeneous. From the Arrhenius-based approach of calculating the ignition delay times for the Livengood-Wu integrals, it is obvious that temperature has the most pronounced effect due to the exponential influence on the ignition delay time. Figure 3.1 shows that a 5% variation of the air-fuel equivalence ratio has a larger effect on the ignition delay time compared to a similar variation of the EGR Rate. Due to the NTC behavior of the fuel, the temperature influence depends on the current temperature. However, during an engine cycle, the temperature increases over a wide range including not only the NTC range but also temperatures with a steep ignition delay time gradient, where a small temperature variation has a large effect on the ignition delay time.

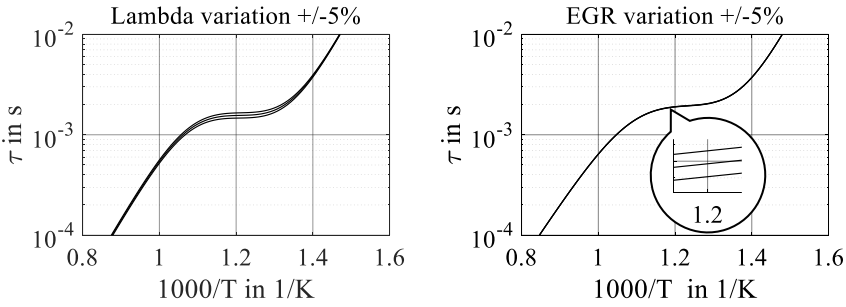

Figure 3.1: Effect of a 5% λ and EGR variation on the ignition delay time.

To compare the influence of all three parameters, a variation of 5%, relative to the initial value, was investigated for otherwise similar initial values, see Figure 3.2a.

The temperature of 770 K refers to the onset of the NTC area (x-value = 1.3 in Figure 3.1), where the temperature gradient is already significantly lower compared to temperatures below 770 K or high temperatures above 900 K. The results show that even at a medium temperature gradient the influence of the temperature is significantly higher compared to the other two parameters. The variation of the EGR rate shows only a very small effect on the ignition delay time.

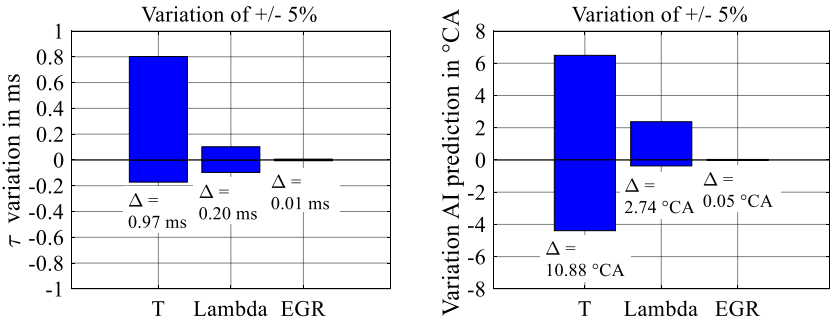

(a) Influence at single operating point – Initial condition: 770 K, 3% EGR, 70 bar, $\lambda = 1$.

(b) Influence averaged over multiple operating conditions, summarized in Table 3.1.

Figure 3.2: Sensitivity of τ (a) and auto-ignition prediction (b) to a variation of the temperature, λ and the EGR rate.

In order to not only evaluate the influence on the ignition delay time but also the resulting prediction of the auto-ignition onset, all three parameters are again varied by 5% but now under various operating conditions. The resulting shift of the auto-ignition onset is then averaged over all operating conditions for each parameter. The results are visualized in Figure 3.2b and the contained operating conditions are summarized in Table 3.1.

Table 3.1: Covered parameters for investigation of auto-ignition model sensitivity to temperature, air-to-fuel equivalence ration and EGR variation.

Parameter	Covered values
Engine speed	1500, 2500, 4000 min^{-1}
IMEP	12, 16, 20 bar
Compression ratio ε_{geom}	10.76, 11.8
Air-fuel equivalence ratio λ	1
EGR rate (internal)	3.3%

The results confirm the large influence of the temperature, whereas the effect of the EGR rate variation is negligible. At this point, it has to be mentioned that the EGR rate in general does have a significant effect on the auto-ignition, especially for higher absolute EGR rates [14]. In case of the investigated simulations with a low EGR rate of 3.3%, the small variation has a negligible effect since the 5% variation refers to EGR rates between 3.1% and 3.5%. Therefore, the inhomogeneity evaluation will focus on temperature and lambda distribution.

3.2 Separation of the Unburnt Zone

Basis of the evaluation are large-eddy simulations of combustion in a single-cylinder engine. Information about the engine as well as the two investigated operating points are summarized in Table 3.2. The large-eddy simulations were performed and the results provided by the Chair of Thermodynamics of Mobile Energy Conversion Systems (tme) of RWTH Aachen University. The two operating points at part-load and a medium engine speed cover two different spark timings with different knock intensities and knock frequencies while all other operating conditions are constant. At each operating point, data of 20 combustion cycles are available. Simulation of each cycle is based on an individual preceding simulation of injection. Thus, the resulting simulated engine cycles are non-consecutive.

Table 3.2: Basic engine data and investigated operating conditions.

Single-cylinder research engine			OP 1	OP 2
V_h	= 400 cm^3	Engine speed:	2500 min^{-1}	2500 min^{-1}
D	= 75 mm	IMEP:	16 bar	16 bar
S	= 90.5 mm	Fuel:	RON95E10	RON95E10
S / D	= 1.2	Ext. EGR Rate:	0%	0%
ε_{geom}	= 11.8	Spark timing:	710 °CA	712 °CA

As a first step before the inhomogeneity can be analyzed the unburnt zone has to be separated from the burnt zone because in 3D CFD simulations the entire combustion chamber is discretized, which includes not only burnt and unburnt zones but also areas close to or in the flame front. This is contrary to 0D simulations with the Entrainment model, where the flame has no thickness and burnt and unburnt zone are already separated as they are treated as individual zones.

If the flame propagation in 3D CFD simulations was to be investigated, a simple separation by temperature is sufficient since the flame thickness is very thin and contains a steep temperature rise (see Figure 3.3). Thus, categorizing cells close to or in the flame front to either the burnt or the unburnt zone yields only a small inaccuracy regarding the position of the flame front. However, to investigate inhomogeneities, separation is more complex.

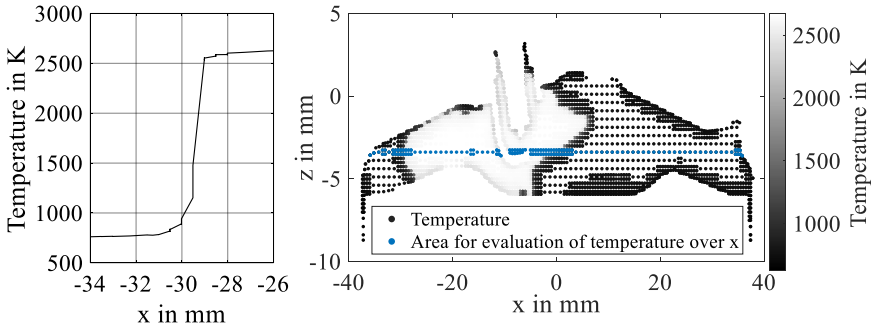

Figure 3.3: Temperature rise from unburnt into the burnt zone.

As can be seen from Figure 3.3, if a separation temperature is set too high, the temperature distribution in the unburnt zone will be dominated by cells with high temperatures near or in the flame front. The high temperatures are caused by heat conduction from the flame front into the unburnt mixture and not the inhomogeneities that shall be evaluated. These cells are expected to be not knock-relevant, since the propagating flame would consume any occurring auto-ignition shortly after, due to the proximity to the flame front. Moreover, a high separation temperature yields another problem for evaluations over time. As the flame propagates through the combustion chamber already burnt areas start to cool down with increasing distance from the flame. Especially towards the end of the combustion, the temperature can drop below the separation limit, leading to a categorization of burnt cells as unburnt. If a low separation temperature is set, the unburnt cells will have a sufficient distance from the flame front and the elevated temperatures close to the flame are excluded. However, due to the much smaller remaining temperature variation, there is a risk of classifying knock-relevant cells or areas with higher temperature as the burnt zone. It is therefore desired to have a separation criterion without direct influence on the temperature.

Taking the previous considerations into account, a separation based on the concentration of chemical species is developed. On the one hand, ignition of the mixture is accompanied by an instantaneous rise of the OH concentration, which is therefore well suited as an indicator of the flame front. On the other hand, the hydroxyl radicals are only a temporary product of the combustion

and the concentration decreases again behind the flame front. For that reason, another species is required to avoid the same problem already encountered with the temperature, by which burnt cells with decreasing hydroxyl radical concentration could be categorized as unburnt.

As the second species, therefore, the concentration of iso-octane is utilized. In comparison to the steep rise of the OH concentration, the reduction of the iso-octane concentration across the flame is more gradual. It is still very well suited as additional criterion because burnt cells close to the flame still contain a significant OH concentration. Burnt cells that are further behind the flame, where the OH concentration has further decreased, have only a very small or no amount of the initial iso-octane left. Thus, the additional criterion prevents burnt cells from being shifted back into the unburnt zone. In Figure 3.4, the basic functionality of the new separation compared to the separation by temperature is shown.

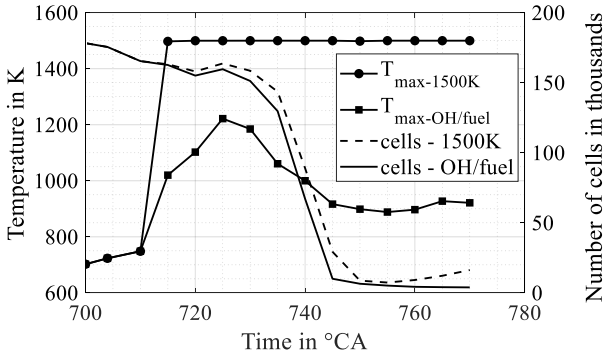

Figure 3.4: Comparison of maximum temperature and number of cells contained in the unburnt zone for separation by temperature (1500 K threshold) and by chemical species concentration (OH and iso-octane).

For the beginning and most of the duration of the combustion, the unburnt zone of both criteria consists of similar numbers of cells. This indicates an accurate separation at the flame front using the new criterion based on chemical species. Towards the end of combustion after 750 °CA, the advantage of the new criterion can be seen, as the number of cells in the unburnt zone remains low until the end of the simulation, whereas it increases for the separation

by temperature. Besides the number of cells, Figure 3.4 shows that with the new criteria the maximum temperature contained in the unburnt zone is more realistic and varies over time. In contrary, for the separation by temperature the hottest cell in the unburnt zone after ignition is always at the separation temperature.

In Figure 3.5a and 3.5b both zones separated by the new criterion are compared to the temperature distribution across the entire combustion chamber. The sectional view confirms the accurate capturing of the flame front. Yet, a visualization of the hottest temperatures within the unburnt zone (Figure 3.5c) reveals that the respective cells are still located close to the flame front. This means the temperature distribution of the unburnt zone is still governed by the high temperatures close to the flame that are not knock-relevant.

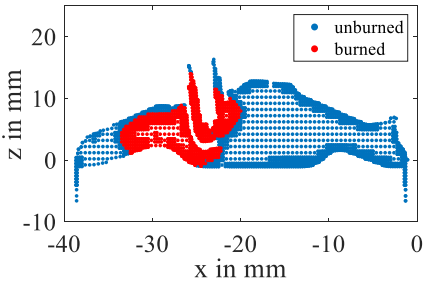

(a) Separation criteria: OH & iso-octane.

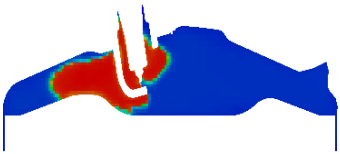

(b) Temperature distribution.

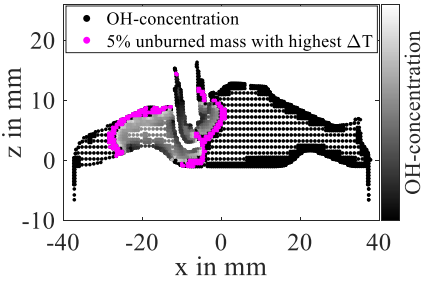

(c) 5% mass with highest temperatures in the unburnt zone.

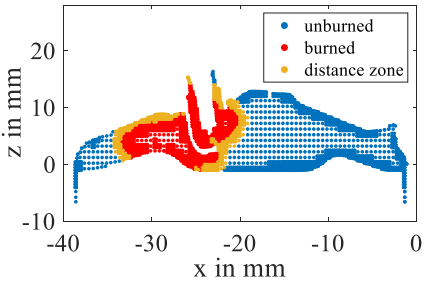

(d) Distance zone of 2 mm.

Figure 3.5: Zone separation based solely on chemical species (a) with flame position (b), location of hottest cells following the separation (c) and introdcution of a distance zone (d) – visualized at time step: 725 °CA.

To eliminate these high-temperature cells close to the flame front from the unburnt zone, an artificial distance zone is applied (see Figure 3.5d). Cells with a minimum distance of < 2 mm to the flame front are excluded from the unburnt zone. This criterion is based on the previously described consideration, that auto-ignition too close to the flame is not knock-relevant, because these cells are consumed after a short period by the propagating flame. The limit of 2 mm was set based on the maximum temperatures contained in the unburnt zone. For a distance smaller than 2 mm, the contained maximum temperatures increase significantly with cells close to the flame front. For distances larger than 2 mm, the maximum temperature remains almost constant. Following these observations, 2 mm appears to be the best compromise to include as many cells as possible without the biasing effect of high-temperature cells close to the flame front.

Verifying again the location of the cells with 5% mass of the unburnt zone and highest temperatures shows that the hottest cells are now distributed across the entire unburnt zone and therefore show the relevant inhomogeneity. Due to the larger spread of these hot cells, a sectional view would only contain very few of the hot cells, thus a projection of the hottest cells is provided, see Figure 3.6. As the verification shows, the new criterion is capable of separating the knock-relevant unburnt zone and thus provides a suitable tool for zone separation before investigating inhomogeneities and their relation to the occurrence of knock.

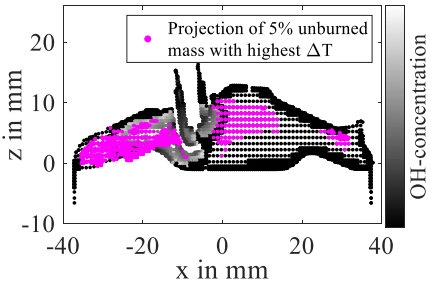

Figure 3.6: Final zone separation based on chemical species and a distance zone of 2 mm – visualized time step: 725 °CA.

3.3 Evaluation of Inhomogeneities

With the previously established separation criterion, inhomogeneities in the unburnt zone, as well as their cycle-to-cycle variation shall be quantified to identify knock-relevant conditions. For this reason, the inhomogeneities will be evaluated over the duration of the combustion. In order to keep the amount of evaluated raw data at an acceptable level, inhomogeneities will be evaluated in steps of 5 °CA, beginning at 700 °CA.

Figure 3.7 shows the unburnt temperatures separated with the new criterion over time. For simplicity, only the results of four time steps are included in the figure. Each time step contains the temperature of all cells of the unburnt zone at the respective time. The results show a large range of temperatures for the unburnt zone already at the first time step. With a spread of over 150 K, the temperature variation at a first glance is significantly higher than expected, based on inhomogeneities observed by Schießl et al. [63, 64].

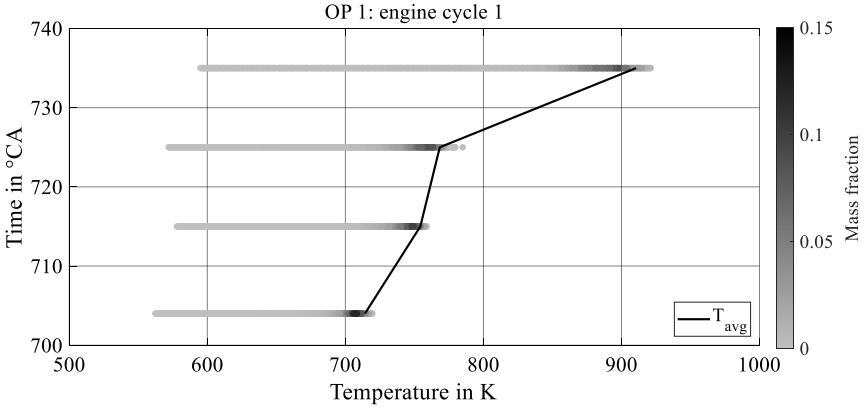

Figure 3.7: Temperature distribution and average temperature over time – absolute temperatures.

An additional greyscale to visualize the mass distribution for the temperature reveals that the majority of cells of the unburnt zone are contained in a much smaller temperature range. Only a few cells with a small total amount of mass represent the wide variation towards lower temperatures. These cells are most

likely located in the top land volume, where their temperature is affected by wall heat losses into the surrounding cylinder wall, piston ring and piston. Generally, the mixture located in the top land volume is the last to be reached by the propagating flame. Thus, there are still unburnt cells remaining in this area until the late phases of the combustion. This explains the small variation of the lowest absolute temperatures over the entire combustion duration. More detailed figures of the temperature distributions at each time step are provided in Appendix A.1.

In opposition to the lowest included temperatures, the average temperature and the maximum temperatures increase significantly throughout the combustion. This results in increasing temperature ranges at each time step. It has to be noted that the average temperature and the maximum temperature are not only rising during the combustion but also during the late compression phase before ignition of the mixture at 710 °CA. Therefore, the cause for increasing average and maximum temperatures of the unburnt zone can not be solely accounted to compression caused by the pressure rise of the combustion or heat conduction from the flame, but also the adiabatic compression before Top Dead Center (TDC) and ignition of the mixture.

With both maximum and average temperature increasing over time, the inhomogeneity of the temperature over time is not directly apparent from the evaluation of absolute temperatures as in Figure 3.7. It, therefore, seems more suitable to evaluate a relative temperature ΔT, defined as the difference between the cell temperature and the average temperature of the unburnt zone at the respective time step:

$$\Delta T = T_{ub,cell} - T_{ub,mean} \tag{3.1}$$

It is obvious that $\Delta T = 0$ as a constant value now represents the average temperature at each time step.

For the visualization and evaluation of the inhomogeneity, quantification is required and multiple options are conceivable. Evaluating the single hottest cell and its temperature elevation over the average temperature is not suitable, since auto-ignition does not originate from such a small volume and the included chemical energy. Thus, a specific mass or volume with highest ΔT, which also refers to the highest absolute temperatures, will be evaluated.

Both mass and volume could be defined as a constant or relative amount. Using a constant volume seems obvious under deliberation that inhomogeneous areas appear as a specific volume with elevated temperature compared to the mean temperature. However, the definition as a constant volume yields some difficulty for the evaluation over the duration of combustion. For advancing combustion, the unburnt volume decreases, thus the relative amount of a constant investigated volume increases. Especially towards the end of combustion, when the unburnt volume gets very small, the investigated constant volume could represent the entire or close to the entire unburnt volume. In such a case, no inhomogeneity would be analyzed but rather mean values of the entire unburnt zone. For this reason, a relative volume or mass is better suitable.

Since no information about the position of the relevant cells with high temperature-elevations to each other is included in the evaluation, it cannot be ensured that the evaluated volume also is a connected volume within the unburnt zone. They could also be single distributed cells. Identifying connected volumes with locally higher temperatures that auto-ignite before the rest of the unburnt mixture yields further challenges and is discussed in Chapter 4. Thus, evaluating a volume instead of a mass does not provide any advantage. However, mass has the advantage that it can be directly compared to the mass fraction burnt at each stage of the combustion, providing a rough estimation about the absolute amount that is included in the relative mass at a specific time step. Due to the non-linear relation between burnt volume fraction and the burnt mass fraction (for assumed spherical flame propagation), this would not be possible if a volume fraction was evaluated. Taking these considerations into account, inhomogeneity is defined as the relative temperature ΔT threshold where all cells with higher ΔT values combined have 5% of the unburnt mass at the respective time step.

In Figure 3.8 the results are presented for one engine cycle. It shows the same engine cycle and therefore same temperature data as in Figure 3.7, but now includes all time steps and the progress of the inhomogeneity over time. The individual temperature distributions for time steps 704 °CA to 740 °CA are provided in Appendix A.1. During the compression phase, the available simulation raw data was exported in steps of 2 °CA before ignition. This is the reason for the unequal spacing of the evaluated time steps before the ignition at 710 °CA.

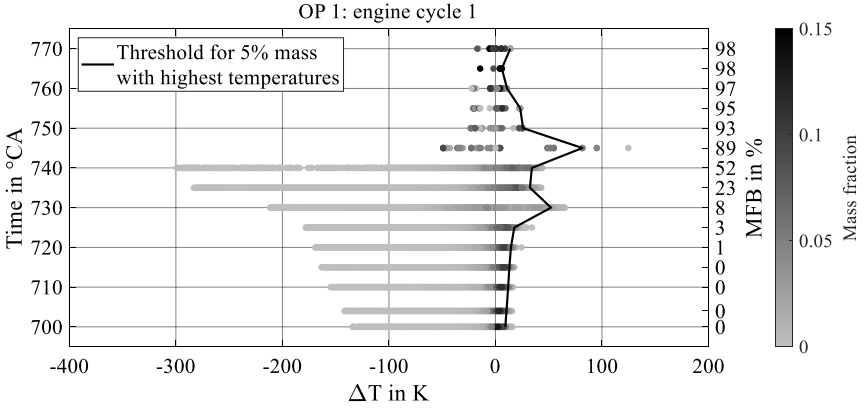

Figure 3.8: Temperature distribution and progress of 5% mass limit with highest temperatures over time – relative temperatures.

An important observation is that the progress of inhomogeneity can be divided into two different phases. During the first phase from the beginning of the evaluation until 725 °CA, the inhomogeneity increases almost linearly. This indicates uneven heating of the unburnt mixture. Equal heating of all cells would lead to increasing average but similarly increasing maximum temperatures. Thus, the resulting ΔT would remain constant. Considering higher specific heat capacities at higher temperatures and assuming equal energy input into the system, ΔT would decrease. However, with temperature differences significantly below 100 K to the average value, differences in the heat capacity are small. Hence, their influence on the progress of ΔT is negligible.

Since this linear increase already occurred during compression, it is likely caused by varying wall temperatures, such as different valve temperatures or temperature differences between cylinder wall, piston, piston ring and spark plug. The inhomogeneity further linearly continues into the first phase of the combustion, in this example until 15 °CA after ignition and an MFB of 3%. Although the burnt mass fraction at the end of this first phase is relatively low, a significant amount of volume has already been burnt (see Figure 3.5).

After 725 °CA, the temperature distribution transitions into a phase where the unburnt zone contains an inhomogeneity with unstable progress over time until combustion is finished. A closer investigation of the temperature profile of a

monitor point in the outer area of the cylinder (see Figure 3.9) reveals occurrence of the first ignition stage shortly after 725 °CA, which is accompanied by a significant heat release. At this time, the previously unburnt mixture is already in the process of igniting. Therefore, it is concluded that the temperature increase following the first ignition stage causes this significant disturbance of the initial temperature stratification and the evaluated inhomogeneity.

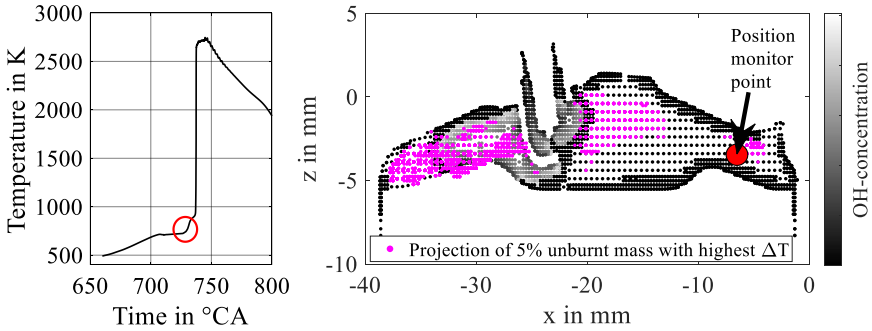

Figure 3.9: Temperature progress over time of a monitor point and it's location in the combustion chamber.

This two-phase behavior with an initially linear increase of the inhomogeneity until the first ignition stage, followed by an unstable progress until the end of combustion, is observed for all 20 engine cycles of each operating point. In order to avoid these disturbances and evaluate the inhomogeneities before the beginning ignition of the mixture, the comparison of all cycles of each operating point is performed at TDC, the last time step where none of the cycles has yet entered the first ignition stage.

The results of all engine cycles at TDC are shown in Figure 3.10a and 3.10b. Both ignition timings contain a general inhomogeneity between 13 K and 18 K. The cyclic variation is small with a variation range below 5 K, which is approximately a third of the general inhomogeneity. Also, not specifically shown in Figure 3.10a and 3.10b, the variation of 5 K is almost constant for the duration of 700 °CA up to 720 °CA. The comparison of temperature inhomogeneities including all engine cylces over the entire combustion duration, can be found in Appendix A.1, exemplarily for OP 1 and OP 2 for the 5% mass definition.

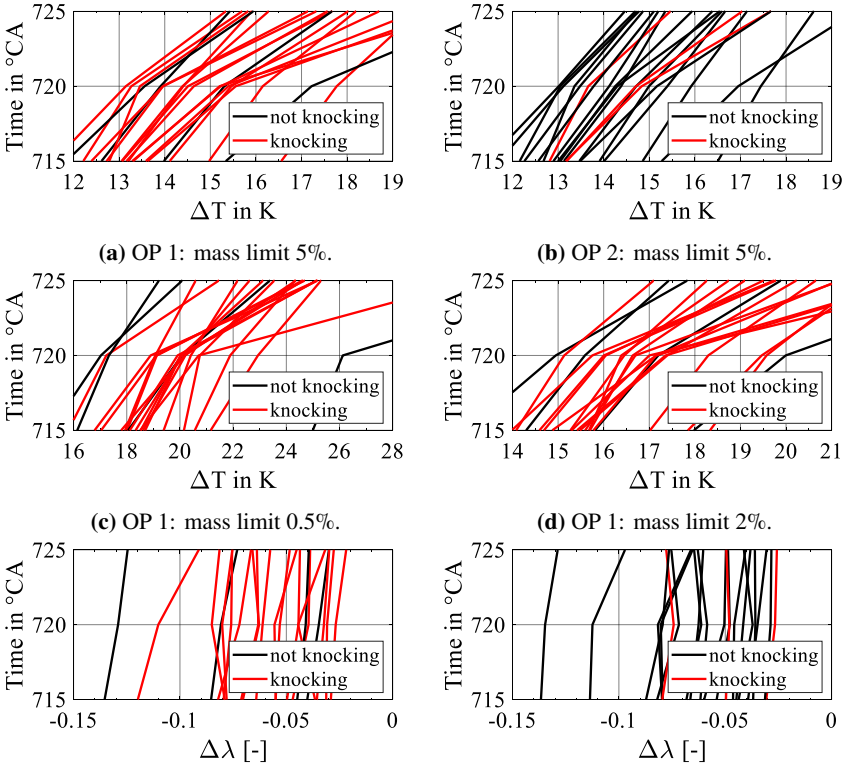

(a) OP 1: mass limit 5%.

(b) OP 2: mass limit 5%.

(c) OP 1: mass limit 0.5%.

(d) OP 1: mass limit 2%.

(e) OP 1: mass limit 5%.

(f) OP 2: mass limit 5%.

Figure 3.10: Temperature and λ inhomogeneity for highest temperatures and lowest λ values: Temperature inhomogeneity for both OPs with 5% mass limit (a) & (b), OP 1 with 0.5% and 2% mass limit (c) & (d) and λ inhomogeneity for both OPs with 5% mass limit.

A comparison to the initial sensitivity study allows an estimation of the influence of this cyclic variation. A temperature variation of 5% across multiple operating conditions led to a variation of the predicted knock onset of 10.88 °CA. At a low unburnt temperature of 600 K, a variation of 5% relates to a temperature variation of 30 K. The observed cyclic variation of 5 K, therefore corresponds to only approx. 17% of this 30 K variation or 0.8% of the absolute temperature of 600 K. Assuming directly proportional behavior, a 5 K variation instead

of 30 K would result in a change of 1.8 °CA for the predicted auto-ignition onset. However, the true variation range will be much smaller and is expected to be below 1 °CA, considering that the temperature increases significantly over the combustion duration. With increasing absolute temperatures the relative variation decreases over time resulting in less change of the predicted auto-ignition onset. For this reason, the cycle-to-cycle variations of the temperature inhomogeneity before occurrence of the first ignition stage in the unburnt mixture are expected to be negligible for the calculation of the auto-ignition onset.

Besides the small cyclic variation, no obvious relation between the inhomogeneity of an engine cycle and the occurrence of knock can be observed. One possible reason might be that the 5% mass fraction limit as the definition of the inhomogeneity includes too many cells, which could lead to a loss of knock-relevant information due to averaging. To eliminate this risk of potential information loss, the results of the first operating point with more knocking cycles are additionally evaluated with two different mass fraction limits: 0.5% and 2% (see Figure 3.10c and 3.10d). As the results show, for the 2% definition, the cyclic variation remains at 5 K, whereas it increases to 10 K for the 0.5% definition. This is a good indicator that for the 0.5% limit the amount of cells included in the definition of the inhomogeneity has significantly decreased, consequently increasing the impact of single cells with high temperatures that are potentially knock-relevant. However, for none of the two definitions, the inhomogeneity shows a clear correlation between the temperature elevation ΔT and the occurrence of knock.

At this point, it has to be mentioned that from a physical point of view, the reduction of the limit to define inhomogeneity is not infinitely reasonable. If the resulting mass fraction gets too small, the remaining mixture and included chemical energy will be too small to explain the occurrence of an auto-ignition. Since no clear connection to the occurrence of knock was observed even for the very small mass limit of 0.5%, no further effort was made to specifically identify the mass fraction relating to a physically reasonable limit.

Besides the limit of the mass fraction, a second possible reason for not observing a dependence between inhomogeneity and knock occurrence is that the single hottest cells are evaluated and not a connected volume of cells with elevated temperatures. Thereby, for example, mixing effects and all other cell interacting

effects that could be knock-relevant are not considered.

With no improvement from different mass fraction definitions, the evaluation of the air-fuel equivalence ratio distribution contains the initial definition with a 5% mass fraction to identify rich cells with the lowest λ values. Similar to the temperature evaluation, the results in Figure 3.10e and 3.10f show no dependence between cells with the lowest lambda values and the occurrence of knock. It can therefore be concluded that solely temperature or air-fuel equivalence ratio inhomogeneities under the current definition cannot identify knock-relevant conditions.

As an additional approach, inhomogeneity is investigated by comparison of local parameters confined to a specific area around the spark plug to the entire unburnt zone before ignition of the mixture. This local area is defined as a sphere with various radii and the center point in the spark plug gap. This approach follows Zhao et al. [65], who investigated consecutive engine cycles with LES and found that the velocity field in the spark plug gap before ignition determines cyclic differences of the flame propagation. Here, the radius of the sphere is varied between 1 mm and 15 mm and the difference of the mean temperature and mean charge velocity within the sphere to the mean temperature and mean charge velocity of the entire unburnt zone are analyzed:

$$\Delta T_{sp} = T_{ub,sphere} - T_{ub,mean} \tag{3.2}$$

$$\Delta v_{sp} = v_{ub,sphere} - v_{ub,mean} \tag{3.3}$$

As for the first approach, the aim is to determine if the local parameters inside the sphere and their deviation to the mean value of the unburnt mixture can be related to the occurrence of knock. In Figure 3.11 the results are presented exemplarily for the smallest radius of 1 mm. Results including both operating points of further investigated radii are summarized in Appendix A.1.

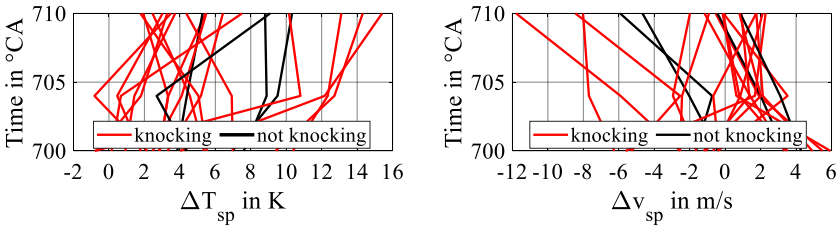

Figure 3.11: Temperature and mixture velocity inhomogeneity for OP 1 for a spherical volume with 1 mm radius around the spark plug gap.

Neither the temperature nor the charge velocity shows a clear correlation between their inhomogeneity and the occurrence of knock. This was the case for all investigated radii of the sphere, which is why only the results of one radius are presented.

In total, all the performed investigations provided data with no clear relation to the occurrence of knock that could be considered within the knock model. Nevertheless, many further effects might be of interest, for example, the direction of charge motion instead of the vectorial velocity, the charge velocity confined to a specific direction or the turbulent kinetic energy within a specific area. Additional insights might be gained by investigating connected volumes without limitation to the area around the spark plug and instead of evaluating global inhomogeneities. Concerning this, the detonation diagram introduced by Bradley et al. [26] contains the evaluation of connected volumes with elevated temperatures that auto-ignite (called hotspots) to identify developing detonations. In the following chapter the evaluation of auto-ignition based on the detonation diagram and its application to 0D simulations is investigated.

4 Evaluation of Auto-Ignition using the Detonation Diagram

4.1 Application of the Detonation Diagram in 0D Simulations

The detonation diagram by Bradley et al. [26] and the contained limits that were confirmed by other researchers [17, 34, 36] was developed to identify developing detonations and categorize auto-ignitions in different regimes, starting from harmless deflagration over developing detonations with significant pressure waves up to thermal explosions. For the classification into the different regimes, two dimensionless parameters ξ and ε that contain local conditions and their stratification in a limited volume with elevated temperature, so-called hotspots, and boundary conditions of the surrounding unburnt mixture are used. Based on these two parameters, it can be evaluated if the propagating auto-ignition front can couple with the pressure wave leading to resonance with large pressure amplitudes in a developing detonation. This work aims to apply the detonation diagram to 0D simulations to identify knock-relevant boundary conditions.

While the initial investigations leading up to the development of the detonation diagram were carried out as 1D simulations [18, 26], many other researchers investigated the detonation theory and its applicability to various fuels in 3D CFD simulations [17, 34, 36, 66]. Netzer et al. applied the detonation diagram to a QD simulation, which allowed a more extensive investigation of multiple engine cycles at a single operating point, as well as various spark timings and various fuel blends [35, 37]. One important finding was an apparent correlation between the variance of ε and the knock tendency (ref. to Figure 2.5 in Chapter 2.3). For advanced spark timings but also for fuels with smaller research octane numbers RON, increased variance of ε was observed.

Following this observation, the 0D application focuses on the determination of the reactivity parameter ε for single working cycles, with the aim to derive a knock-relevant parameter, such as the knock tendency or knock frequency. Since the hotspot size contained in ε, acc. to Equation 2.13, represents a local condition that exceeds the mean values calculated by a two-zone combustion model, the determination of the hotspot radius will be the main challenge for a successful application.

The same operating conditions already summarized in Table 3.1 are used for this investigation. For each engine speed and engine load combination, measurement data of 500 single working cycles at five different spark timings is available. The data originates from the same single-cylinder research engine with details displayed in Table 3.2 that was the basis for the large-eddy simulations used for the inhomogeneity investigation in Chapter 3. The five spark timings include a low knock frequency of close to 0% up to the knock boundary (defined as 4-10% knock frequency) for each engine speed and load combination. Thus, the data cover 70 operating points and 35 000 engine cycles in total. Additionally to the measurement data, Pressure Trace Analysis (PTA) results for each engine cycle are available.

To calculate ε, the acoustic velocity, the excitation time and the hotspot radius are required. Both acoustic velocity and excitation time are determined for the entire unburnt zone at the time of auto-ignition. The two-stage auto-ignition model, presented in Chapter 2.4.3, is thereby utilized to determine the auto-ignition onset also named Knock Onset (KO). The acoustic velocity calculates to:

$$a_{ub,KO} = \sqrt{\frac{c_p}{c_v} \cdot R \cdot T_{ub,KO}} \tag{4.1}$$

The included values to determine the acoustic velocity at time of knock onset are directly available from the PTA results of each cycle. The excitation time is determined from a lookup table based on pressure and temperature of the unburnt zone, fuel-air equivalence ratio of the unburnt zone and the global internal EGR rate. The lookup table was provided by the Chair of Thermodynamics of Mobile Energy Conversion Systems (tme) of the RWTH Aachen University and was created based on 3D simulations of an adiabatic reactor with detailed reaction kinetics applied. A reduced form of the utilized lookup table is provided in Appendix A.2. The required input parameters, similar to determination of the acoustic velocity, are directly available from the PTA results. The hotspot

radius r_0 is set to a constant value of 10 mm, following Robert [66]. This allows calculation of the reactivity parameter ε in the unburnt zone at the time of auto-ignition for each engine cycle as follows:

$$\varepsilon = \frac{r_0}{a_{ub,KO} \cdot \tau_{e,ub,KO}} \tag{4.2}$$

The mean values and the variance of ε are determined from the 500 single values at each operating point and are presented exemplarily for two engine speed and load combinations in Figure 4.1. The results including all operating points are summarized in Appendix A.3.

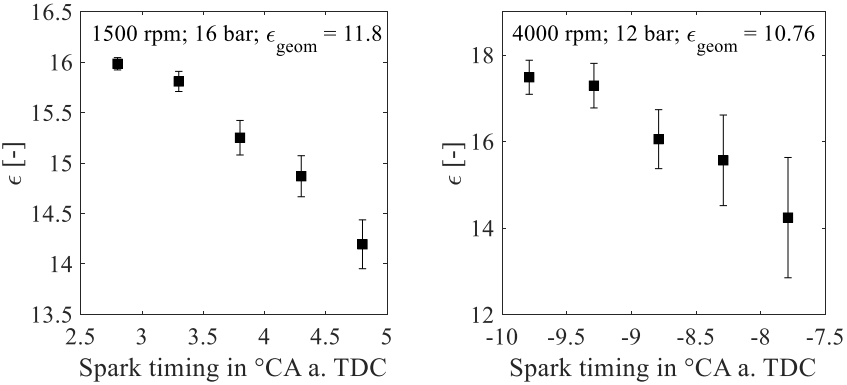

Figure 4.1: Mean and variance of ε determined from 0D data at the time of auto-ignition for various operating conditions – contained hotspot radius r_0 assumed with 10 mm for all engine cycles in accordance with [66].

In comparison to the results by Kalghatgi, Peters and Bates et al. [17, 34, 36], the mean values of ε are unexpectedly high. For non-knocking or slightly knocking operating conditions, they found ε values below 10. For $\varepsilon > 10$ Kalghatgi and Bates et al. solely observed heavy knocking cycles or super knock. Since the utilized data for which the reactivity parameter was calculated is located just at the knock boundary, mean values are expected to be below 10, for which other researchers observed no or only slight knock. Netzer et al. [37] did observe higher values, up to $\varepsilon \geq 20$ even for operating points close to the knock boundary (ref. to Figure 2.4f data set ST Ref+2) within the QD investigation. However, these results also show a much larger variation of ε at a

single spark timing, including values below five. Thus, the mean values are still significantly lower than the ones determined in this work. In addition to the unexpectedly high mean values of ε, the correlation between variance and the knock tendency that was observed by Netzer cannot be confirmed. The results in Figure 4.1 show an inverse trend with decreasing variance for higher knock tendencies and overall smaller variance of ε.

One main reason for the large discrepancy of the determined values and available results from literature is expected to be caused by the hotspot radius initialization with a constant value of 10 mm. Analyzing 3D CFD simulations, Netzer found a maximum hotspot radius of approx. 12 mm [35]. This hotspot occurred for an extreme spark advance of 10 °CA relative to the reference spark timing. For less spark advance, significantly smaller hotspot sizes with values between 1.5 mm and 6.5 mm were observed [35]. This is a first indicator that 10 mm might not be a suitable definition, since it appears to be at the upper limit of observed hotspot sizes.

In order to further assess the constant hotspot radius value of 10 mm, flame propagation in the two-zone combustion model is analyzed, see Figure 4.2. The comparison of the burnt volume fraction and burnt mass fraction shows that they are not proportional to each other. Considering that auto-ignition typically occurs in the late stages of the combustion at approximately 85-95% burnt mass fraction, only 1-5% of unburnt volume are remaining at that time. In Figure 4.2 additionally, a maximum hypothetical hotspot radius r_0 is given. This radius is calculated based on a spherical hotspot with similar volume as the entire remaining unburnt mixture volume. This reveals a maximum hypothetical hotspot radius of 6-9 mm for 1% and 5% unburnt volume respectively. Considering these values refer to a hotspot that contains the entire unburnt volume and not a local fraction of it, clearly shows that 10 mm is not a suitable value.

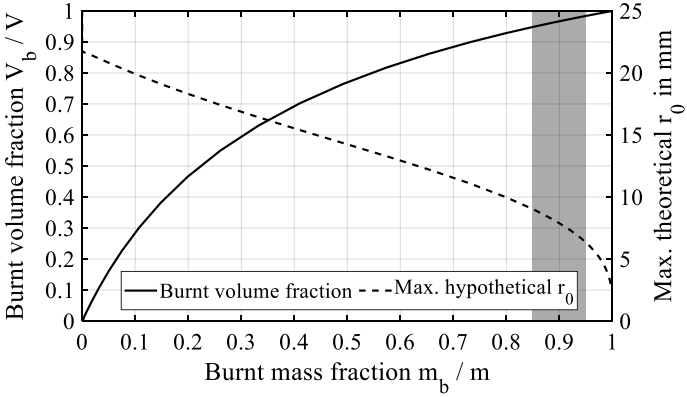

Figure 4.2: Relation of burnt volume and burnt mass fraction within the Entrainment model and maximum hypothetical radius for a spherical hotspot based on the unburnt volume.

It has to be stressed that this does not mean hotspots with a radius of 10 mm or larger cannot exist. Besides the typical auto-ignition onset at late stages of the combustion, there are engine cycles with extremely early auto-ignition at an MFB of 50% or less [15]. Consequently, for such early auto-ignition also a larger unburnt volume is remaining. In addition, the shape of the hotspot might not always be a perfect sphere. Thus, larger radii are possible at smaller included volumes when referring to the maximum extent of such non-spherical hotspots. However, for operating points with a very low knock frequency close to 0%, where the majority of engine cycles have no or only minor pressure oscillations, the 10 mm definition is not realistic.

Moreover, the definition as a constant value for all engine cycles has to be questioned. Since the cycle-to-cycle combustion variations largely influence the chemical reactions leading to auto-ignition, also the formation of hotspots is expected to be affected by the cyclic variations. Thus, modeling a distribution of different hotspot sizes for a single operating point seems more suitable than assuming a constant size.

To realize such modeling, different considerations have to be taken into account. The hotspot size cannot be infinitely small because a minimum amount of energy is required for the auto-ignition. Further, small-sized hotspots are expected to

occur more frequently than larger hotspots due to the generally small remaining unburnt volume at later stages of the combustion in which hotspots can form. Lastly, higher knock frequencies and consequently higher knock intensities are expected to correlate with larger hotspots since more chemical energy is released during their auto-ignition.

Based on these considerations, a halved normal distribution with a minimum radius of 1 mm will be used for modeling the radius distribution. Variation of the standard deviation between values of 1 mm and 3 mm allows adjustment of the maximum occurring radius (see Figure 4.3). The limits for the standard deviation are defined following the observations from Netzer in [35].

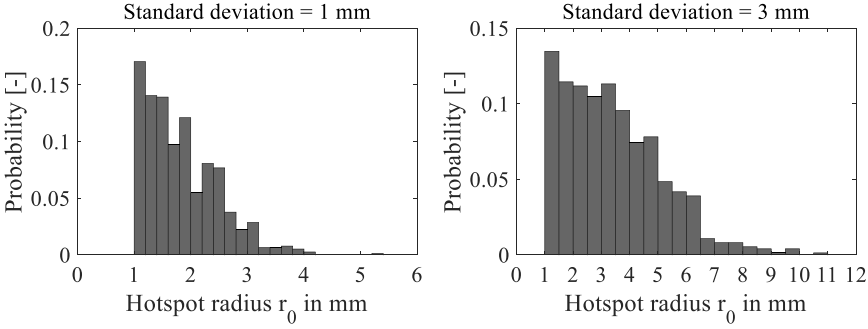

Figure 4.3: Halved normal distributions to model a hotspot radius distribution – minimum (left) and maximum (right) defined standard deviation to control the maximum ocurring hotspot size.

Netzer did not observe developing detonation for $r_0 < 3\,\text{mm}$. Applying a standard deviation of 1 mm to a halved normal distribution with minimum values at 1 mm, 91% of all included hotspot sizes are below 3 mm. Thus, this lower standard deviation limit applies to operating points with a very low knock frequency. For the maximum standard deviation of 3 mm, 91% of all hotspot sizes are between 1 mm and 7 mm and the maximum included hotspot radius is approximately 11 mm. This applies to operating points with higher knock frequencies, as Netzer observed a maximum hotspot radius of 11.9 mm and found that developing detonations are possible for hotspot sizes between 3 mm and 6 mm, depending on the local boundary conditions [35].

In order to calculate ε based on a modeled distribution of hotspot sizes, a specific standard deviation has to be assigned to each operating point with respect to the prevailing operating conditions. The initial approach was to scale the standard deviation of the distribution based on the total unburnt volume at the time of the auto-ignition. Considering, that a hotspot refers to a fraction of the unburnt volume, an early auto-ignition onset and therefore larger unburnt volume would increase the probability that a large hotspot forms. For later auto-ignition onsets with less remaining unburnt volume, this probability would be smaller. Since auto-ignition of larger hotspots releases more chemical energy than auto-ignition of smaller hotspots, consequently, a correlation between the unburnt volume at auto-ignition onset and the knock frequency is expected.

However, the evaluation (left plot of Figure 4.4) reveals no obvious dependence between the unburnt volume at the time of auto-ignition and the knock frequency. A likely reason for the missing correlation comes from the restriction to mean values within the 0D two-zone combustion model. Effects like asymmetric flame propagation and separation of the unburnt volume into smaller volumes when the flame already reaches the cylinder wall in some areas are not accounted for. Especially the separation into smaller independent volumes with individual local conditions and their high relevance for the occurrence of knock was already described by Kleinschmidt in [19], who named these separated volumes "endgas-pockets". Since the two-zone combustion model does not account for these effects, a different parameter for assigning an appropriate standard deviation for each modeled radius distribution is required.

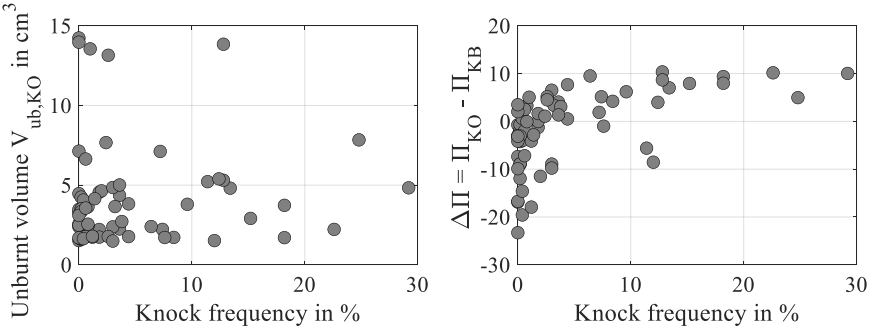

Figure 4.4: Unburnt volume (left) and $\Delta\Pi$ (right) at the time of auto-ignition in relation to the knock frequency.

Knock criteria of 0D knock models, as the ones presented in Chapter 2.4.3, are used to evaluate if an operating point is above or below the knock boundary. As mentioned in the beginning of this chapter, the knock boundary for the data used in this investigation is defined as a knock frequency between 4% and 10%. Within the knock criterion a specific value representing this knock boundary is calculated. The difference of the actual value at an operating point and this knocking threshold could be used as an indicator for possible occurring hotspot sizes. Figure 4.4 (right) shows such a difference over the measured knock frequency. The utilized model is the Pi-criterion by Hess [23] that was introduced in Chapter 2.4.3. The deviation $\Delta\Pi$ is calculated from the knock boundary Π_{KB}, calibrated for this engine, and the value of Π calculated for each operating point at the time of auto-ignition Π_{KO}:

$$\Delta\Pi = \Pi_{KO} - \Pi_{KB} \tag{4.3}$$

In comparison to the unburnt volume, $\Delta\Pi$ shows a much better correlation and is subsequently used to assign a standard deviation for the hotspot size distribution of each individual operating point.

Since no information about the true distribution of hotspot sizes at any of the operating conditions is available, lower and upper limits of the standard distribution (1 mm and 3 mm respectively) are assigned to the operating points with the lowest and highest $\Delta\Pi$ values of all operating points included in the investigation. For all other operating points, the standard deviation for the modeled radius distribution is calculated from a simple linear approach based on the prevailing $\Delta\Pi$ value according to Equation 4.4:

$$\sigma(\Delta\Pi) = \Delta\Pi \cdot 0.06 + 2.38 \tag{4.4}$$

The reactivity parameter is then again calculated for all engine cycles, now including hotspot radii according to the specific modeled distribution for each operating point instead of a constant value for each engine cycle. Acoustic velocity and excitation time are determined similarly for the unburnt volume at the time of auto-ignition from Equation 4.1 and the lookup table respectively. The results presented in Figure 4.5, contain the same operating conditions as Figure 4.1 and confirm a much more reasonable mean value and variation of ε, considering location of the operating points close to the knock boundary. For all operating conditions, ε-values between 1 and 11 are observed. Additionally, the variance of ε now follows the trend observed in the literature and increases

at higher knock tendencies. Results including all operating conditions are summarized in Appendix A.4.

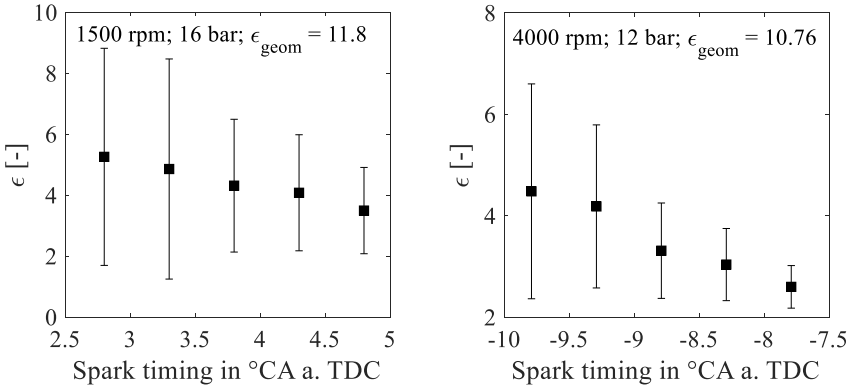

Figure 4.5: Mean and variance of ε determined from 0D data at the time of auto-ignition for various operating conditions – calculation based on modeled hotspot radius r_0 distribution.

With more realistic results, it is now of interest, if there is vice versa a direct relation between the reactivity parameter and the knock tendency of an operating point. Therefore, the 3-Parameter-Approach introduced by Hess in [15, 67] is utilized. This approach was developed based on measurement data of the same single-cylinder engine and allowed a precise calculation of the knock frequency based on the distribution of the auto-ignition onset of single working cycles. To evaluate the relation between ε and the knock tendency, this calculation method is applied to the distribution of ε to determine the knock frequency based on the reactivity parameter. Other than applying the method to the distribution of ε instead of the auto-ignition onset, the method remains similar. Details about the calculation using the 3-Parameter-Approach are given in Chapter 5, where the influence of cycle-to-cycle variations on knock is further investigated or can be found in [15, 67].

The comparison of the knock frequency derived from ε and the measured knock frequency in Figure 4.6 shows that the trend of the increasing knock frequency is correctly replicated by the calculated knock frequency. However, the results also show that for many operating points the knock frequency is overestimated

and for fewer operating points the knock frequency is underestimated. For an ideal correlation between ε and the knock frequency the results would be located closely around the angle bisector.

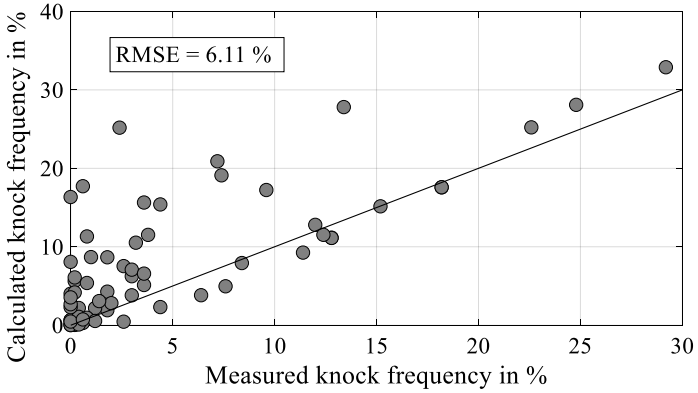

Figure 4.6: Knock frequency calculated from ε distribution vs. measured knock frequency.

The mean deviation reveals that the calculated knock frequencies on average deviate by over 6% from the measured values. Considering that the knock boundary for the engine is defined as a range covering 6%, between 4-10%, this might seem like an acceptable result. However, a deviation of 6% at a high measured knock frequency of 30% still is a relative deviation of 20%. For small measured knock frequencies under 5% at the lower end of the knock boundary, the relative error increases even above 100%.

In comparison to the observed mean deviation of over 6%, in [15, 67] Hess demonstrated an accuracy of 1.81% for the knock frequency calculation based on auto-ignition onset distributions determined from measurement data. In terms of a relative deviation, this relates to 6% and 36% for a 30% and 5% knock frequency respectively. This highlights the significantly smaller accuracy of the approach using the ε-distribution.

Different contributing factors for this significant accuracy loss are plausible. To start with, the in the literature observed correlation between the variance of the reactivity parameter and the knock tendency could be insufficient for an

accurate prediction of the knock tendency. Besides, the comparison between the application approach using a constant radius and the second approach using a modeled hotspot radius distribution demonstrates the significant influence of the hotspot radius on the reactivity parameter. Additionally, the multitude of modeling assumptions and definitions that are required to model the hotspot size distribution as realistically as possible in a 0D environment could deteriorate the prediction accuracy.

However, due to a lack of information, many assumptions in the modeling approach for the hotspot sizes can either not be or not sufficiently be validated. No measured distribution of hotspots is available that could confirm the suitability of a halved normal distribution for modeling. Moreover, missing data of hotspot size distributions at different operating conditions prevent validation of the scaling approach for the standard deviation and assignment of a specific standard deviation to an operating point. This conflict between the high sensitivity of ε to the contained hotspot radius and the lack of validation possibilities for the modeling approach of the hotspot radii inevitably leads to a loss of modeling accuracy.

The acquisition of validation data is exacerbated by the fact that auto-ignition of a hotspot occurs in a locally confined area but not the same for each engine cycle and occurs in a very short time frame. This makes it very difficult to capture the phenomenon with optical measurements. Another difficulty regarding the measurement of local effects is the required optical access to the combustion chamber. It is not always possible to provide access to all relevant areas and engine design might deviate from the original engine to allow optical access at all. Further, 0D simulations, based on a two-zone combustion model, such as the one utilized in this project, do not account for inhomogeneities and can therefore not be used to acquire validation data. Therefore, almost exclusively, 3D CFD simulations with sufficiently high spatial and temporal resolution can provide suitable validation data. This method, however, requires an extremely high computational effort, especially if the cyclic distribution of specific local parameters is of interest since then data of a sufficient amount of cycles is required.

In this project, large-eddy simulation results of 100 engine cycles at a single operating point are available. This enables the evaluation of a distribution of local parameters, such as the hotspot radius, for at least this single operating

point. Therefore, it could give further insights into the suitability of the modeling approach for the hotspot size distribution. An evaluation of auto-ignition hotspots is, however, not trivial, since auto-igniting cells have to be distinguished from the spark-ignited flame front. Therefore, in the following chapter, a method is presented that allows the efficient identification of auto-igniting hotspots within large amount of data from 3D CFD simulations.

4.2 Identification of Hotspots in CFD Simulation Data

Large-eddy simulations provide detailed information about local conditions in the cylinder during the combustion. In comparison to measurements, the simulation allows investigation of any local area within the discretized domain in very small time-frames, without time resolution limitation from measurement equipment. Timely resolution in the simulation is only limited by the time step size initialized within the numerical solver that is applied. This is especially beneficial for fast occurring effects like auto-ignition. Additionally, no modification of the engine design to provide access for measurement is necessary.

However, detecting auto-ignition of an area, entirely separated from the spark-ignited flame front, named hotspot, is challenging. In contrast to pre-ignition, the auto-ignition occurs simultaneously to cells igniting due to propagation of the spark-ignited flame front. Therefore, it has to be distinguished, if the igniting cell is part of the flame front or part of an auto-igniting hotspot. This cannot be done by only evaluating temperature or chemical species concentration.

A visual inspection of a cross-section through the combustion chamber allows identification of hotspots, but regarding only one cross-section for example horizontally through the cylinder is insufficient. An area that appears as a hotspot in such a cross-section might not truly be separated from the flame front, but could be connected to it further above or below, due to folding of the flame. Therefore, it would be required to analyze many cross-sections in various heights through the cylinder to determine a true separation from the flame front. Furthermore, this evaluation would have to be repeated at many time steps, since the exact time of hotspot auto-igniting is unknown. Considering a data volume

of approx. 22 GB per engine cycle for the available simulation which includes 100 single engine cycles, such a manual identification is not reasonable.

In order to reduce the required effort, a method is developed that allows automated and efficient identification of auto-igniting hotspots and can be applied universally to different engine designs and simulation results by simple calibration. An overview of the different steps of the proposed method is given in Figure 4.7.

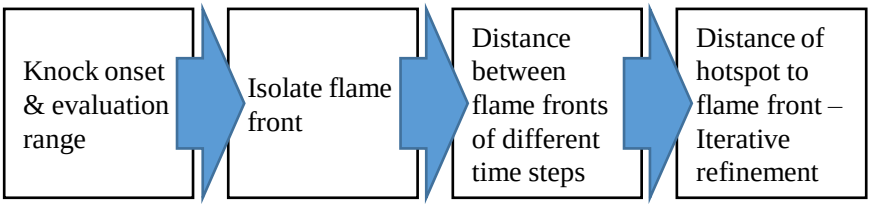

Figure 4.7: Four-step method to identify auto-igniting hotspots in 3D CFD simulations.

The first step is to determine the knock onset to allow the limitation of the time range that will be investigated to identify knock-relevant hotspots. The workflow, shown in Figure 4.8, to determine the knock onset is analogous to the method in [15, 67]]. It calculates the last zero crossing of the pressure oscillations before they reach either half the knocking threshold $KPP_{threshold}$ or half of the maximum amplitude, whatever occurs earlier. Unlike the application of a bandpass filter to isolate the knock-relevant pressure oscillations from a measured global cylinder pressure, in the simulation, global in-cylinder pressure and local pressure at the position of the knock sensor are available. Their difference directly provides the relevant pressure oscillations.

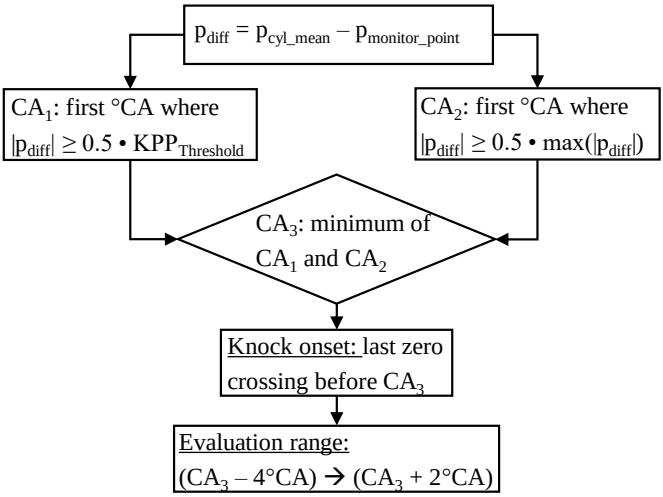

Figure 4.8: Determination of the knock onset and evaluation range for identification of hotspots, calculation analogous to the method described in [15, 67].

The time range to be evaluated is set to 6 °CA: from 4 °CA before to 2 °CA after the determined knock onset. A time range is required to ensure the relevant time step is included since the calculated knock onset might not exactly represent the time of auto-ignition and the local pressure signal at position of the knock sensor can contain a lag between auto-ignition and occurrence of the triggered pressure waves. For the investigated engine geometry and typical in-cylinder conditions at the time of auto-ignition, such lag is estimated to be below 1 °CA. After detection of the pressure oscillations, no knock-relevant hotspots are expected. Thus, the higher relevance of the time before onset of the pressure oscillations, the aim of keeping the evaluation range as small as possible to reduce computational effort and the inaccuracies in the calculated knock onset, explain the asymmetric definition of the evaluation range. This way, the estimated lag is sufficiently covered and the time range even enables capturing of possible earlier hotspots that might trigger further auto-ignitions leading to the detected pressure oscillations.

In the second step, cells within the flame front are isolated. As apparent from Figure 3.3, cells in the temperature range from 1400 K to 1600 K are well within the area of the steep temperature gradient in the flame front. Therefore,

cells within this temperature range are separated. In contrast to the initial investigation of inhomogeneities, here, a separation based on the temperature is possible because cells directly within the flame front are of interest, not the adjacent unburnt zone. A range of separation temperature ensures enough cells are included for reliable application of the method. Still, the range is defined as little as possible, since the performance of the subsequent computations is significantly dependent on the number of cells. For clarification, when referring to the flame front in the following steps, these separated cells with temperatures between 1400 K and 1600 K are meant.

The third step marks the actual beginning of the hotspot identification by comparing the flame front cells of two different time steps, see the top left plot of Figure 4.9. The distance of the flame front of the currently investigated time step to the flame front of an earlier time step is calculated. As visualized in Figure 4.9 in the upper plots, this is realized by determining the distance of each cell at the current time step to all flame front cells at the earlier time step (indicated by the red arrows) and saving solely the smallest distance (indicated by the blue arrows). This provides the minimum distance to the previous flame front for each cell of the current time step. Due to this approach, the number of cells included in the isolated flame front significantly affects the performance.

As long as only the spark-ignited flame propagates and no hotspot auto-ignites, the minimum distances between the compared flame fronts will be distributed around a value referring to the mean flame velocity at relatively small distances. If a hotspot auto-ignites its cells will have a significantly larger distance to the flame front of the preceding time step, due to their separation from the spark ignited flame front. This characteristic can be seen from the lengths of the arrows starting from the hotspot in the top left plot of Figure 4.9.

This distance difference is confirmed by the histogram including the calculated minimum distances, see the bottom left plot of Figure 4.9. The majority of cells have a minimum distance distributed around 1 mm. These can be attributed to the spark ignited flame front. For larger minimum distances up to approximately 2 mm the number of cells drops close to zero. However, from 3 mm to 6 mm the number of cells increases again. These cells with significantly higher minimum distances can be attributed to a hotspot. This characteristic is used to initially separate the hotspot cells from the rest of the flame front.

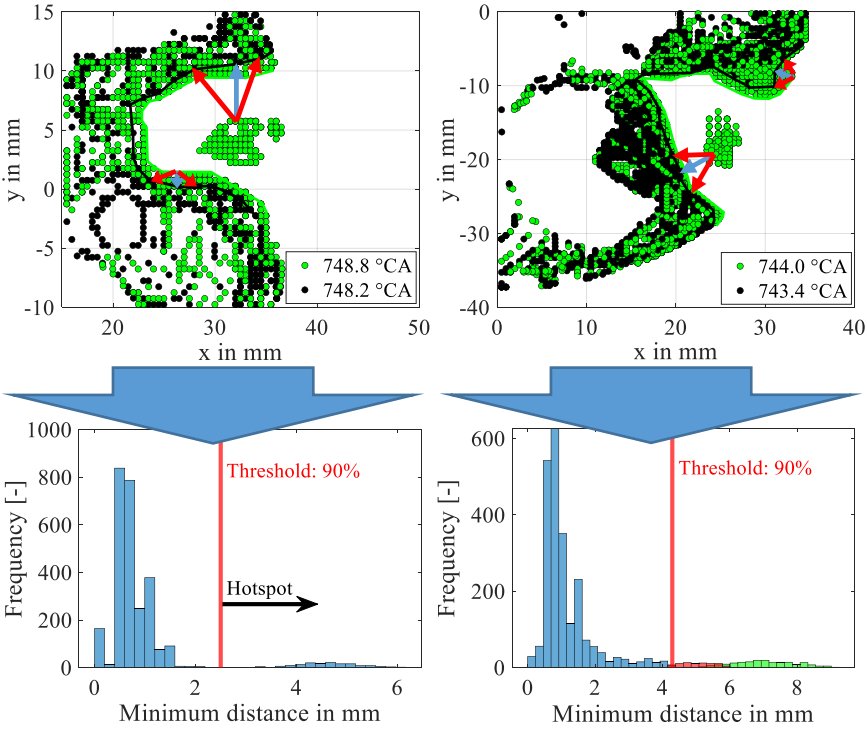

Figure 4.9: Evaluation of the flame propagation distance between two time steps of two different engine cycles – cycle one (left) with clear distinction of hotspot cells and cycle two (right) without clear distinction of hotspot cells.

Therefore, a threshold is defined as the minimum distance where 90% of all cells at the current time step have a smaller minimum distance. This threshold is the first calibration parameter and can be adjusted for different data to match the region of minimum distances with almost no cells between spark-ignited flame front and hotspot.

An important assumption embedded in this definition is that any occurring hotspot contains 10% of the isolated and investigated cells. During development of the method and application to simulation data, this yielded good results. However, if the method was to be applied to data that shows a significant

variation of the number of cells included in the hotspots, the relative definition could be set more conservatively to include more cells, as later described in further detail or an absolute definition of the threshold could be considered.

It has to be mentioned that also the difference between the time steps, defined with 0.6 °CA, influences the results and robustness of the method. A smaller time difference between the compared steps makes the method more robust since the flame front propagates a smaller distance. Even considering locally varying flame velocities, in areas with higher propagation velocity, the traveled distance remains smaller. Consequently, the occurrence of a hotspot always shows a significant difference regarding the minimum distances to the preceding time step. However, if a hotspot develops over multiple time steps and the difference is too small, only the initial phase of the development can be captured. As soon as the flame front is compared to an earlier time step that already contains the hotspot, the minimum distance falls in the same range as for the propagating spark-ignited flame. Thus, no hotspot could be identified. For that reason, a sufficient difference is required to ensure comparison to a time step without a hotspot to be able to capture the formation over multiple time steps.

On the downside, a larger time difference can lead to a less distinct distribution of the minimum distances. Although the distance results on the right side of Figure 4.9 are determined for the same 0.6 °CA time difference definition, they show the effect of a larger time difference very well. The majority of cells still have a minimum distance below 2 mm, but for all larger minimum distances included an almost constant amount of cells exists. For this engine cycle, the definition of a threshold would be difficult because of a missing clear distinction between cells of the flame front and the hotspot. Application of the 90% threshold reveals that not only hotspot cells are separated but also cells of the flame front, as marked in red in the bottom right plot of Figure 4.9 and the bottom left plot of Figure 4.10.

This is the typical effect for larger time differences and conservative definition of the threshold. Due to the longer duration, the spark-ignited flame can propagate significantly larger distances, especially in regions with higher local flame velocities. If the duration is long enough that the regular flame propagation locally reaches similar distances as the occurring hotspot, the distribution of minimum distances becomes ambiguous, similarly as shown in the bottom right histogram of Figure 4.9. Still, in order to be able to capture hotspots developing

over multiple cycles, 0.6 °CA was found to be the smallest possible time step size and a fourth step is added to the method to refine the identified potential hotspot cells to remove falsely categorized ones, if necessary.

For this final step, the distance of the potential hotspot cells to the flame front at the current time step is evaluated. As can be seen in Figure 4.10, hotspot cells have a greater distance to the flame front compared to the cells that are categorized as a hotspot but are part of the flame front. A threshold of 2 mm is applied, to re-define cells with smaller distances back into the flame front.

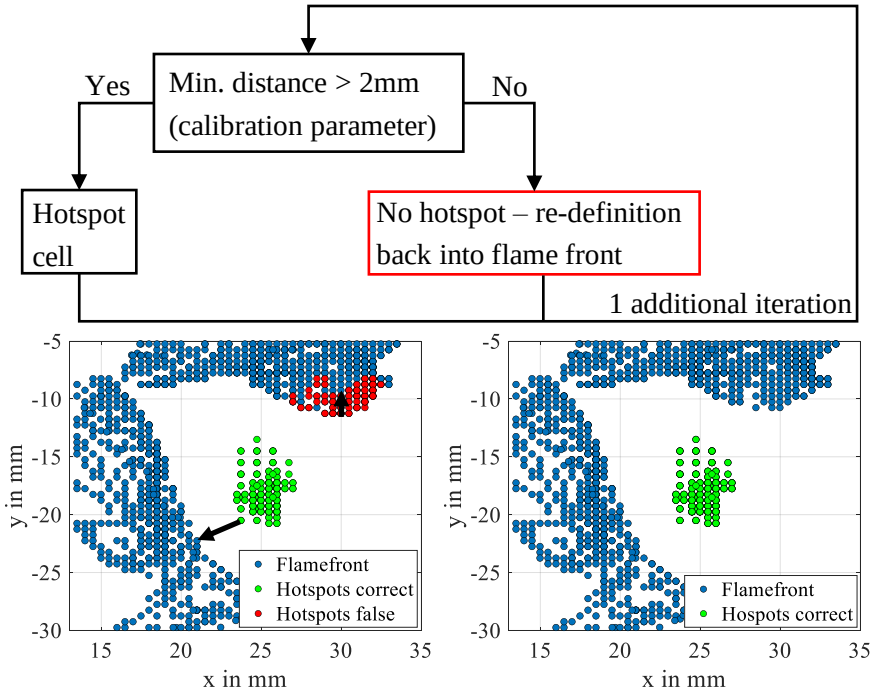

Figure 4.10: Iterative refinement of potential hotspot cells by evaluation of the minimum distance to the flame front. Hotspot cells with a minimum distance of < 2 mm are re-defined as the flame front.

This threshold is the second calibration parameter of the method and influences how close hotspots can appear to the flame front and still be detected. Definition

as 2 mm is based on the same assumption as in Chapter 3.2, that auto-ignition too close to the flame front is not knock-relevant, since the igniting hotspot is directly consumed by the propagating flame. Additionally, for the data investigated in this project, the threshold of 2 mm yielded the best results.

Re-defining potential hotspot cells back into the flame front influences the distance calculation for all remaining hotspot cells. Therefore, the best results in eliminating as many cells as possible that are not part of the igniting hotspot were achieved by one additional iteration. In this second loop, again, the distances for all remaining hotspots are calculated and cells with minimum distances below 2 mm are re-defined as flame front cells. The general method of the iteration loop is summarized in Figure 4.10.

Finally, Figure 4.11 exemplarily shows a time step of occurrence and the separated hotspot after a successful identification, which subsequently allows investigation of local parameters of such hotspot. Due to the simplicity of the method, including only two calibration parameters, it is very easy to apply and the setup of the method allows a forgiving and user-friendly calibration.

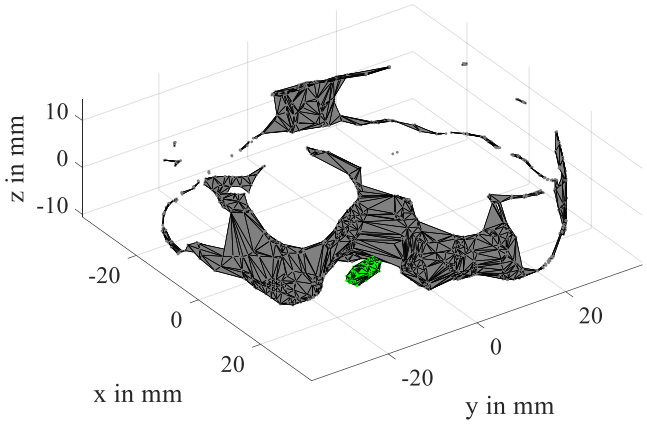

Figure 4.11: Final identified hotspot in comparison to the spark ignited flame front.

The first threshold can be set rather conservatively, to ensure capturing of all hotspot cells. This reduces the number of distance distributions that have to be

investigated to set a suitable threshold for an engine. Even if a larger number of flame front cells initially is identified as a hotspot, the iterative refinement reliably filters out these cells. If the results are still not satisfactory after two refinement loops, further iterations can be easily added to filter out as many flame front cells as possible. Since the refinement is already set up as two loops, increasing the number of iterations is a simple task.

The second threshold parameter directly influences the distance a hotspot can have to the flame front and still be identified. A larger distance threshold filters out more cells in a single loop, compared to a smaller one. This can enable a reduction of required iterations. Yet, for larger or smaller thresholds, the number of iterations has to be chosen carefully, since a single cell between hotspot and flame front categorized as flame front could lead to elimination of all hotspot cells in following iterations. For this reason it is advisable to use as few iterations as possible and rather keep a small number of cells that are not part of the hotspot instead of risking elimination of all initially identified hotspot cells.

In total, the approach provides an efficient and user-friendly method to identify local auto-ignitions within CFD simulation results. Additionally, due to its basis on purely geometrical information, the method is not limited to large-eddy simulations but could also be applied to RANS or DNS. Accuracy of the results and possibilities to investigate local conditions would then only be limited by the general limitations of the chosen simulation approach.

In this project, the method is applied to the available LES results of one operating point including 100 engine cycles that were set up to match a knock frequency of 50%. Thereby, 54 hotspots in knocking and non-knocking cycles for 53 engine cycles could be identified. At one engine cycle, two hotspots occurred simultaneously. No correlation between hotspot occurrence and knocking could be observed. The results are used to investigate the size distribution of the hotspots. The operating conditions for this single operating point are:

- Engine speed: $2500\,\mathrm{min}^{-1}$
- IMEP: 16 bar
- Compression ratio ε_{geom}: 11.8
- Air-fuel equivalence ratio λ: 1
- Ext. EGR Rate: 0%

To evaluate the radius, different approaches are conceivable since the identification method only provides the hotspot cells but no information about the shape of connected cells. Two different ways of calculating the hotspot radius are applied. For the first one, the volumes of all hotspot cells are accumulated and assumed to form a spherical hotspot. From this sphere, the radius of the hotspot can be derived. For the second one, the two cells of the hotspots with the largest distance from each other are determined. The radius is calculated as half the maximum distance. This yields a radius representative for the largest spatial extend of the hotspot. Values similar to the first calculation method would indicate that the identified hotspots have an almost perfect spherical shape.

In Figure 4.12, the hotspot size distributions of both approaches are shown. Comparison of both distributions reveals significant differences in the maximum contained radius. Whereas the maximum radius for evaluation assuming a sphere is 1.9 mm, the maximum radius evaluating the largest distance is by more than factor seven greater with a radius of 14 mm. Regarding the lower distribution limits, the smallest observed values are 0.8 mm for evaluation as sphere and 2.2 mm for evaluation of the maximum extend. This indicates that the hotspots rarely occur in an almost perfect spherical shape and commonly have a more flat and elongated shape. This seems reasonable, considering that hotspots typically auto-ignite in later stages of the combustion where the small unburnt volume is distributed along the cylinder wall.

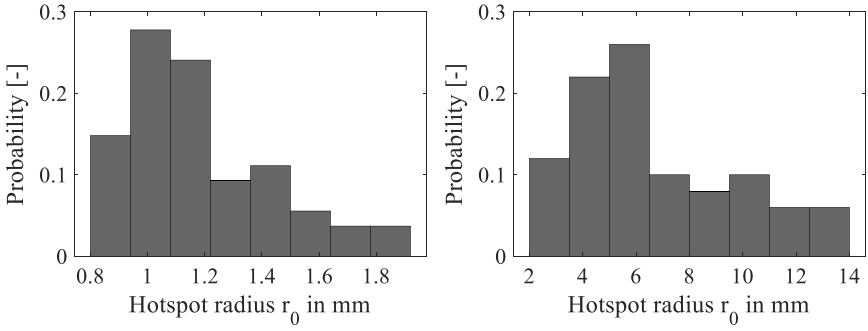

Figure 4.12: Hotspot radius distribution of a single OP, determined from 100 simulated engine cycles. Radius determined for a sphere (left) and from maximum distance between two hotspot cells (right).

The differences in the observed hotspot sizes also highlight the large influence of the radius calculation method. Still, in terms of shape, both distributions are very similar. It appears the most suitable modeling approach would be a skewed normal distribution or a stretched beta distribution. Yet, although slightly less accurate, modeling by a halved normal distribution is a good first approximation, as the majority of values is shifted towards the lower end of each distribution. Mainly the reduction of probability towards the smallest observed values is not accounted for using a halved normal distribution. Consequently, implementing a different distribution function to match the hotspot size distribution more realistically could be a conceivable measure to improve modeling accuracy.

Further, in terms of observed hotspot sizes, the results of both distributions confirm that a constant radius of 10 mm is not suitable as a realistic assumption for the hotspot sizes. However, this evaluation of a single operating point does not provide sufficient data to validate the suitability of the scaling approach for the standard deviation of the modeled distribution and the subsequent assignment to different operating points.

In order to further evaluate the sensitivity of the knock frequency calculation to the hotspot size modeling approach, based on the new results, a streched beta distribution is set up to model the hotspot sizes more realistically compared to a halved normal distribution, see Figure 4.13 left side. As can be seen, modeling is now based on the previously acquired hotspot size distribution where the radius was determined by the maximum distance between two identified hotspot cells (ref. to Figure 4.12 right side).

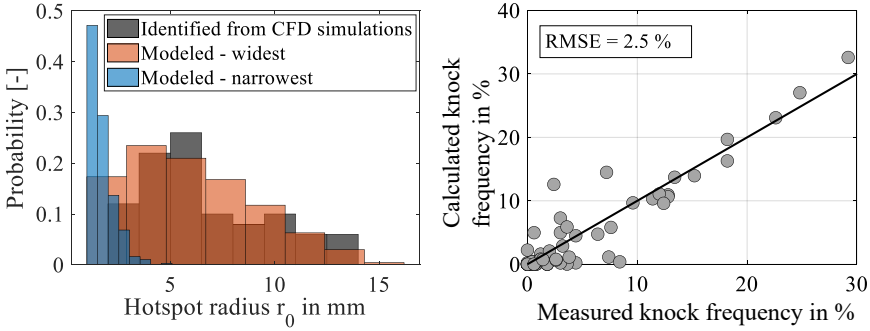

Figure 4.13: Modeled hotspot distributions based on a beta distribution and predicted knock frequencies based on ε distribution.

Since the evaluated simulation represents operating conditions at a high knock frequency of 50%, this distribution is assumed to yield the largest hotspot sizes and thereby represents the upper limit of the modeled hotspot size distributions. Scaling the width of the modeled distribution is realized analogous to the previously introduced method with the only exemption that now the second parameter of the beta distribution instead of the standard deviation is varied. The covered values range from 5 to 35 and relate to the maximum and minimum width of the beta distribution respectively. Also similar to the first modeling approach, the minimum hotspot size is limited to 1 mm. Finally, the first parameter of the beta distribution has a constant value of 2 and each distribution is streched by a factor of 20.

The comparison of the maximum width modeled distribution with the distribution determined from 3D CFD simulation in Figure 4.13 shows the good agreement of the new modeling approach with the real size distribution. Similar to the first modeling approach, the most narrow distribution includes maximum hotspot sizes of around 5 mm (ref. to Figure 4.3).

The knock frequency calculated from ε-distributions with the refined size modeling approach is shown on the right side of Figure 4.13. The results show a significant increase in accuracy with a mean deviation of 2.5%, compared to the 6.11% (ref to. Figure 4.6) reached with the initial modeling approach. This highlights that a high accuracy and realistic hotspot size distribution is crucial to reach better prediction qualities. However, compared to the 1.81% mean deviation demonstrated by Hess in [15, 67], the knock frequency calculation based on the reactivity parameter ε is still less accurate.

To sum up, the results show that the application of the Three-Parameter-Approach to the detonation parameter ε can provide a tendency regarding the knock-relevance of various operating conditions, confirming the correlation between the variation of ε and knock tendency observed by Netzer [35, 37]. In comparison to the prediction accuracy by Hess in [15, 67], the results however show a significant lack of accuracy and high sensitivity of the reactivity parameter ε to the included hotspot size. The low precision can mainly be attributed to the lack of validation possibilities.

Investigation of the hotspot distribution at a single operating point revealed crucial information but is insufficient for a comprehensive validation of the modeling approach. The determined hotspot size distributions showed that the

initially assumed halved normal distribution is a good first approximation, but higher accuracy can be reached using a stretched beta distribution. However, even with the refined distribution modeling method, the mean deviation of the calculated knock frequencies is still higher compared to the mean deviation demonstrated in [15, 67].

The evaluation of the hotspot distributions also reveals the large influence of the radius calculation approach, enhancing the difficulties with the high sensitivity of ε to the hotspot size. This demonstrates that an enormous effort would be required to validate the entire current 0D modeling approach or to be able to perform further in-depth investigations to set up another appropriate modeling approach.

Another contributing factor, regarding a 0D application for the prediction of knock-relevant conditions at the knock boundary, might be the general purpose of the detonation diagram. Previous investigations utilized the detonation diagram mainly to identify super-knock conditions [17, 34] with extreme pressure oscillations that can lead to instant engine failure. The transition from deflagration to developing detonations as super-knock events cover a generally larger range of parameters within the detonation diagram. Thus, the fact that the thresholds between the different auto-ignition regimes are not strict limits but rather represent a range of conditions where the transition occurs (ref. to Figure 2.4a and [26]) have less importance for the identification of super-knock-relevant conditions. However, precise differentiation of operating conditions close to the knock boundary proves to be very challenging, since these conditions are confined to a much smaller area within the detonation diagram. This can already be observed in results from Bates and co-workers in [17]. As can be seen in Figure 2.4d, for the transition from deflagration to developing detonation, they counterintuitively observed heavy knock at higher parameters of ξ and ε, closer to the transition limit and slight knock for smaller ξ and ε values, that would be assumed to cause more severe pressure oscillations.

For these reasons, at this point, it does not seem reasonable to further investigate a possible application of the detonation diagram in a 0D simulation environment for the identification of knock-relevant conditions close to the knock boundary. However, Hess demonstrated a high knock frequency calculation accuracy using the Three-Parameter-Approach in [15, 67], by application on auto-ignition onset distributions determined from measurement data. It therefore seems promising

to keep investigating the Three-Parameter-Approach to evaluate the influence of cycle-to-cycle variations on knocking behavior, but by means of auto-ignition onset distributions instead of ε distributions. Therefore, in the subsequent chapter, it will be investigated if simulations considering the cyclic combustion variations and thus variations of the time of auto-ignition are suitable for a prediction of the knock tendency.

5 Influence of Cycle-to-Cycle Variations on the Knock Frequency

5.1 Three-Parameter-Approach

Large variations of the combustion are typical for spark-ignited engines. They are caused by the variation of multiple parameters such as temperatures, homogenization of the mixture, turbulence and duration of the initial ignition phase. They occur even under stationary operation of an engine and the magnitude of the variation depends on the operating conditions. Due to these unavoidable fluctuations, parameters such as the burn duration, center of combustion, maximum pressure and IMEP also vary from cycle to cycle. Especially due to variations of the resulting temperatures and pressures, the cycle-to-cycle variations have a significant influence on the occurrence of auto-ignition and knock.

The objective of 0D/1D knock models generally is to predict the KLSA for the average working cycle, which represents the knock boundary for specific operating conditions of an engine. This knock boundary, for the data used within this project, is defined as a range of 4-10% knock frequency but can typically range between 1% and 10% [22, 23, 24]. Knock models like [22, 23, 60, 68] are applied to the simulation of varying spark timings and evaluate if the mean cycle of an operating point is below or above the knock boundary.

The Three-Parameter-Approach introduced by Hess [15, 67] allows a precise calculation of the actual value of the knock frequency under consideration of prevailing cycle-to-cycle variations since the calculation is based on measure-

ment data of single working cycles. It, therefore, seems crucial to include cyclic variations in a prediction of knock-relevant conditions.

In comparison to the previous approach where the cyclic variation of the detonation diagram parameter ε was considered, the cycle-to-cycle variations shall now be considered by application of the knock frequency prediction approach in its original form to 0D simulations. The aim is to enable a prediction of the actual value of the knock frequency rather than the binary classification if an operating point is above or below the knock boundary, as provided by the current knock models. This provides further details about the current operating conditions regarding engine knock. At first, prior to the application, the calculation approach will be introduced in more detail.

The Three-Parameter-Approach, introduced by Hess [15, 67], was developed based solely on measurement data. It provides the first step towards a predictive calculation method of the knock frequency that can be applied to simulations, since it is independent of pressure oscillations, which are not modeled in typical 0D simulation tools. Basis of the development was measurement data of single working cycles close to the knock boundary. The different steps of the calculation method are presented in Figure 5.1 at the example of a measurement set that contains five different operating points with various spark timings at otherwise similar operating conditions, see Figure 5.1b.

Each of the operating points contains the pressure traces of 500 consecutive single working cycles. The state-of-the-art two-stage auto-ignition model [16] is used to determine the auto-ignition onset of all single working cycles. Before that, a pressure trace analysis PTA is performed to obtain the required inputs for the auto-ignition model. This allows determination of the auto-ignition onset distributions of each operating point, as shown in Figure 5.1a for one operating point.

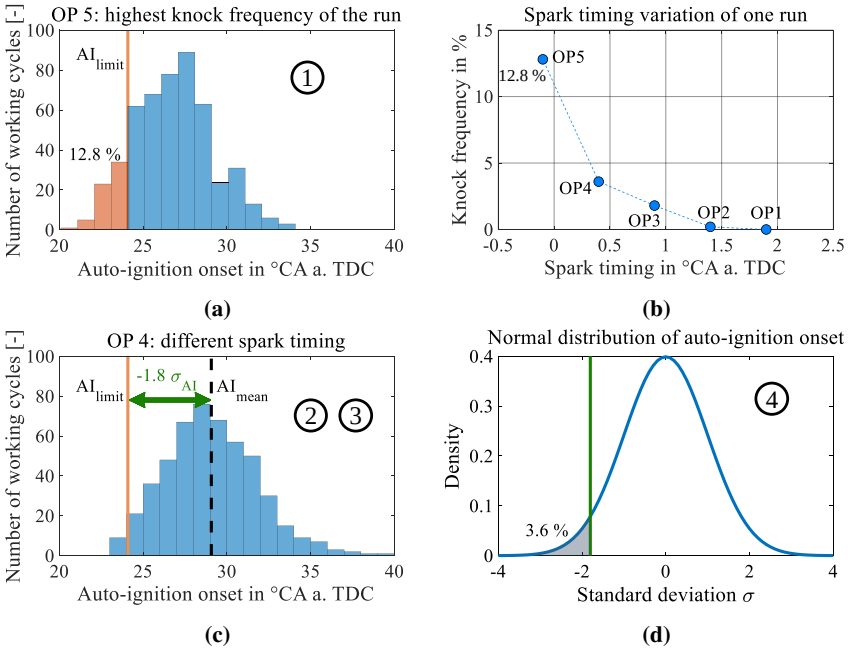

Figure 5.1: Three-Parameter-Approach for calculation of the knock frequency, according to [15, 67].

The first step towards the knock frequency calculation is to determine an auto-ignition limit AI_{Limit} for the operating point with the highest knock frequency. Therefore, the number of knocking single working cycles is calculated based on the measured knock frequency and the total number of measured cycles. In this case, with a measured knock frequency of 12.8% and 500 measured engine cycles, this calculates to 64 knocking engine cycles. The auto-ignition limit AI_{Limit} is set in such a way that 64 cycles or 12.8% cycles (marked orange) have an earlier auto-ignition onset than the calibrated limit. This limit is the first of three parameters required for the knock frequency calculation and is calibrated only at the operating point with the highest knock frequency. It remains constant for the knock frequency calculations of all other spark timings.

In the second step, the AI_{Limit} is applied to all operating points. In Figure 5.1c, this is illustrated for OP 4. However, instead of evaluating the number of single

working cycles with auto-ignition onset before AI_{Limit}, the mean auto-ignition onset AI_{mean} and the standard deviation σ_{AI} as representative parameters for each auto-ignition onset distribution are determined .

As third step, the difference between AI_{Limit} and AI_{mean} is calculated as the multiple of the standard deviation σ_{AI} of the respective operating point. For the fourth and final step, a Gaussian distribution is assumed for the auto-ignition onset distribution of all operating points. This allows calculation of the knock frequency as the probability of values of this Gaussian distribution deviating by more than the multiple of σ_{AI} from AI_{mean}.

Therefore, in summary, three parameters, which are derived from the auto-ignition onset distribution of an operating point, AI_{Limit}, AI_{mean} and σ_{AI} are required for the calculation of the knock frequency. Hess used this method to calculate the knock frequency for 70 operating points in total and found a high accuracy comparing the results to the measured knock frequencies [15, 67].

From the introduction it is apparent that single working cycles are required in order to apply the knock frequency calculation approach from measurement data to the simulation. As mentioned, this is a major difference to the application of current knock models, since the determination of the knock-limited spark advance using knock models like [22, 23, 60, 68] is based on evaluation of the average working cycle. For this reason, two different approaches to predict the knock frequency with the Three-Parameter-Approach are introduced that are based on different methods to simulate single working cycles.

For both simulative approaches, similar operating conditions as for the development of the Three-Parameter-Approach will be investigated. Thus, measurement data of single working cycles of all operating points are available. This enables validation of the simulated single working cycles and the predicted knock frequencies. In total 15 operating points covering two different engine speeds and two different indicated mean effective pressures are investigated, as summarized in Table 5.1. Each combination includes five operating points with different spark timings while the remaining operating conditions are similar. For all single working cycle simulations, the Entrainment model [40, 41] is used.

Table 5.1: Operating conditions covered by the simulations of single working cycles.

Engine speed	IMEP	
2500 min^{-1}	12 bar	16 bar
1500 min^{-1}	-	16 bar

5.2 Simulation of Single Working Cycles

For the first simulation approach, to create the cyclic fluctuations, a turbulence level distribution is modeled. This will alter the flame propagation velocities and subsequently will result in a variation of the engine load, the center of combustion, the pressure gradient, the maximum pressure and the combustion efficiency, replicating the cycle-to-cycle variations.

Before initializing a variation of the turbulence, the simulation model is set up to be able to predict the average working cycles of all five operating points that are included in one measurement set. As the next step, similarly to the calibration of AI_{Limit}, the turbulence level distribution is initialized and calibrated for the operating point with the highest knock frequency.

The Entrainment model provides different modules for the calculation of turbulence. For this investigation the base turbulence model is used which calculates the progress of the turbulent kinetic energy over time based on a simple k-ε_{tke} model and a start value of the turbulent kinetic energy. This start value can be adjusted by the user via a scaling factor. Further details about the utilized turbulence model are given in [44, 45]. Different turbulence levels are realized by a variation of the scaling factor, which in turn varies the start value of the turbulent kinetic energy.

The modeled distribution of this scaling factor contains 500 individual values with a distribution as shown on the left side of Figure 5.2, exemplarily for the engine speed and load combination of 2500 min^{-1} / 16 bar. The number included in the distribution matches the number of measured single working cycles, allowing simulation of the same number of engine cycles.

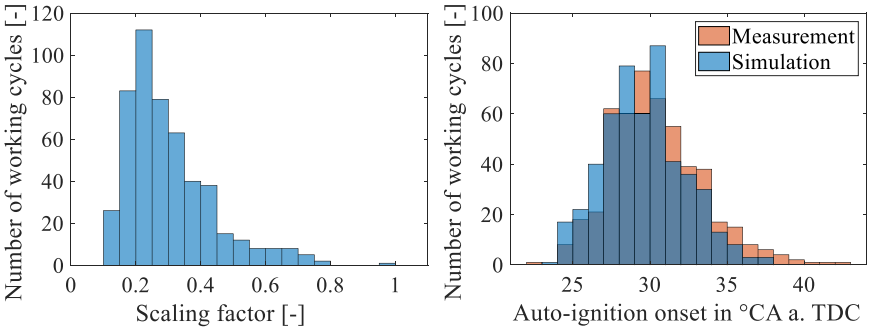

Figure 5.2: Scaling factor distribution to vary the turbulence level and auto-ignition onset distribution of the simulated SWCs, according to [69].

As the comparison on the right side of Figure 5.2 indicates, the scaling factor distribution is set up to yield auto-ignition onsets that match the auto-ignition onset distribution of the measured cycles. However, the presented comparison of auto-ignition onset distributions does not show the results of the operating point with the highest knock frequency, but those of an operating point with lower knock frequency at the same engine speed and load. This demonstrates that the measured cycle-to-cycle variations can be calculated precisely, especially considering calibration of the scaling factor distribution exclusively at the operating point with the highest knock frequency.

In order to determine the auto-ignition onsets, 500 SWCs are simulated for each operating point with the applied scaling factors, while all other calibrated simulation model parameters are kept constant. Subsequently, the simulation results are used as input for the two-stage auto-ignition model to determine the time of auto-ignition of each cycle. The utilized auto-ignition model [67] is the same that was also used for the development of the Three-Parameter-Approach.

In Figure 5.3, the pressure traces of the simulated single working cycles in comparison to the variation range of the measured cycles are presented for the operating point with the highest knock frequency at 2500 min^{-1} / 16 bar, for which the scaling factor distribution was set up. The results indicate that the simulated cycles based on the modeled turbulence level distribution match the measured cycle-to-cycle variation very well.

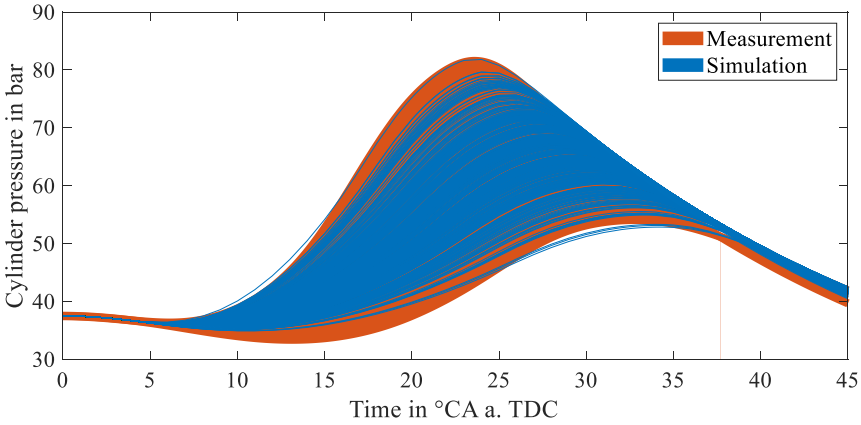

Figure 5.3: Cylinder pressure of simulated SWCs using a turbulence level distribution in comparison to measured SWCs at 2500 min^{-1} / 16 bar, according to [69].

The scaling factor distribution is, without further calibration, applied to the remaining different spark timings at lower knock frequencies (four operating points for each measurement data set). This allows the simulation of 500 SWCs for all operating points at a certain engine speed and load combination with a turbulence level distribution that was calibrated only at a single operating point. Similar to the first operating point, the auto-ignition model is used to determine the auto-ignition onset of each simulated SWC.

Finally, with the auto-ignition onset of every operating point determined for the first simulation approach, the Three-Parameter-Approach can be applied. Since the data from the simulations with 500 single values for the auto-ignition onset of each cycle is similar to the input data used for the development of the Three-Parameter-Approach, determination of the parameters AI_{Limit}, AI_{mean} and σ_{AI} as well as the final calculation of the knock frequency is identical:

1. AI_{Limit} is determined from the auto-ignition onset distribution.
2. AI_{mean} is the arithmetical mean of the auto-ignition onsets of each operating point.
3. σ_{AI} is the standard deviation of the auto-ignition onsets of each operating point.

4. Knock frequency = probability that values of a Gaussian distribution exceed $(AI_{Limit} - AI_{mean})/\sigma_{AI}$.

For the second simulation approach, the CCV-model developed by Wenig [42, 50] and introduced in Chapter 2.4.2 is utilized. The model provides a phenomenological approach to predict cyclic combustion fluctuations. In comparison to the first simulation approach, this model allows a significant reduction of the required calculation time, since the model simulates a smaller amount of single working cycles (15 instead of 500 cycles).

Similar to the first SWC simulation approach, the CCV-model is calibrated at the operating point with the highest knock frequency, to match the measured standard deviation of the IMEP. It is then applied to all further operating points without any additional calibration.

In Figure 5.4, the simulated cycles are compared to the variation range of the 500 measured engine cycles for the operating point with the highest knock frequency at 2500 min^{-1} / 16 bar. The comparison shows that the simulated cycles are well within the scatter of the measured cycles while having a smaller maximum variation. This is expected, as the simulated cycles do not directly represent the true variation and the final cyclic variation is determined by weighting of these simulation results.

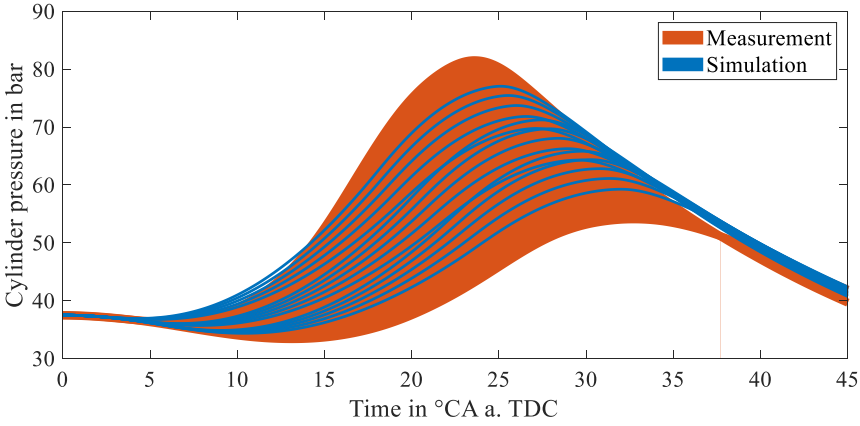

Figure 5.4: Cylinder pressure of simulated SWCs using a CCV-model in comparison to measured SWCs at 2500 min^{-1} / 16 bar, according to [69].

Subsequently, also similar to the first simulation approach, the auto-ignition model is used to determine the auto-ignition onset of each simulated single working cycle. Due to the reduced number of 15 simulated cycles compared to the 500 within the first simulation approach, the simulation performance could be significantly increased by factor 575. This is discussed further in the following section of this chapter.

However, due to this reduced amount of simulated cycles, the strategy to determine the parameters AI_{Limit}, AI_{mean} and σ_{AI} for the knock frequency calculation has to be adapted. Instead of calculating the arithmetical mean for all available auto-ignition onset values, AI_{mean} is calculated as weighted mean based on the 15 available values with the same weights that are used within the CCV-model (ref. to Figure 2.8). Equally, the standard deviation is calculated based on the available values and weights.

Since only a reduced amount of cycles and their auto-ignition onset is available, AI_{Limit} could only be determined with a maximum resolution of 1/15, instead of a resolution of 1/500, using the same calibration method as Hess and as previously used for the first simulative approach. This corresponds to a maximum knock frequency resolution of 6.67% which is not sufficiently accurate considering that the highest measured knock frequencies range between 12% and 30%. To overcome the issue, AI_{Limit} is calibrated iteratively at the operating point with the highest knock frequency. Therefore, a start value for AI_{Limit} is initialized at a very early timing, defined as $AI_{mean} - 8 \cdot \sigma_{AI}$. Application of the Three-Parameter-Approach then allows calculation of the knock frequency, which is ~0% for the initialized AI_{Limit}. Note that the knock frequency calculation based on the proposed method using a normal distribution can never truly become 0% or 100%, but initialization of such an early AI_{Limit} provides a knock frequency very close to 0%. The limit is then increased iteratively in small increments until the calculated knock frequency matches the measured knock frequency. This enables accurate calibration of AI_{Limit} and thereby the calculated knock frequency at this operating point without limitation to the resolution as described above.

5.3 Results and Discussion of Predicted Knock Frequency

The calculated knock frequencies based on the simulated single working cycles in comparison to the measured knock frequencies are presented in Figure 5.5 for both simulation approaches and all three engine speed and load combinations. For reasons of readability, subsequently, the simulation approach modeling a turbulence level distribution will be referred to as the first simulation approach and the simulation method using the CCV-model will be referred to as the second simulation approach.

The results, generally, show a very good agreement with the measured knock frequencies. Both, best agreement and largest deviation are found for the second simulation approach at operating conditions of $2500\,\mathrm{min}^{-1}$ / 16 bar and $2500\,\mathrm{min}^{-1}$ / 12 bar respectively.

In order to quantify the calculation accuracy in more detail, the deviation of the center of combustion of the predicted knock frequency from the center of combustion of the measured knock frequency is evaluated. This deviation is exemplarily visualized by the horizontal arrow in Figure 5.5 for one operating point at $2500\,\mathrm{min}^{-1}$ / 12 bar within the second simulation approach. Linear interpolation between the measured knock frequencies is applied to calculate the center of combustion at similar knock frequencies as the simulated results. However, the predicted knock frequencies of two operating points, marked with $(*)$, are higher than the maximum measured knock frequencies of the respective measurement set. Thus, no interpolation between measurements is possible to determine the center of combustion required for the comparison. For both these operating points, therefore, an exponential fit is applied to the measurement results of all five contained spark timings of the measurement set. This allows extrapolation of a center of combustion for a knock frequency exceeding the highest measured knock frequency.

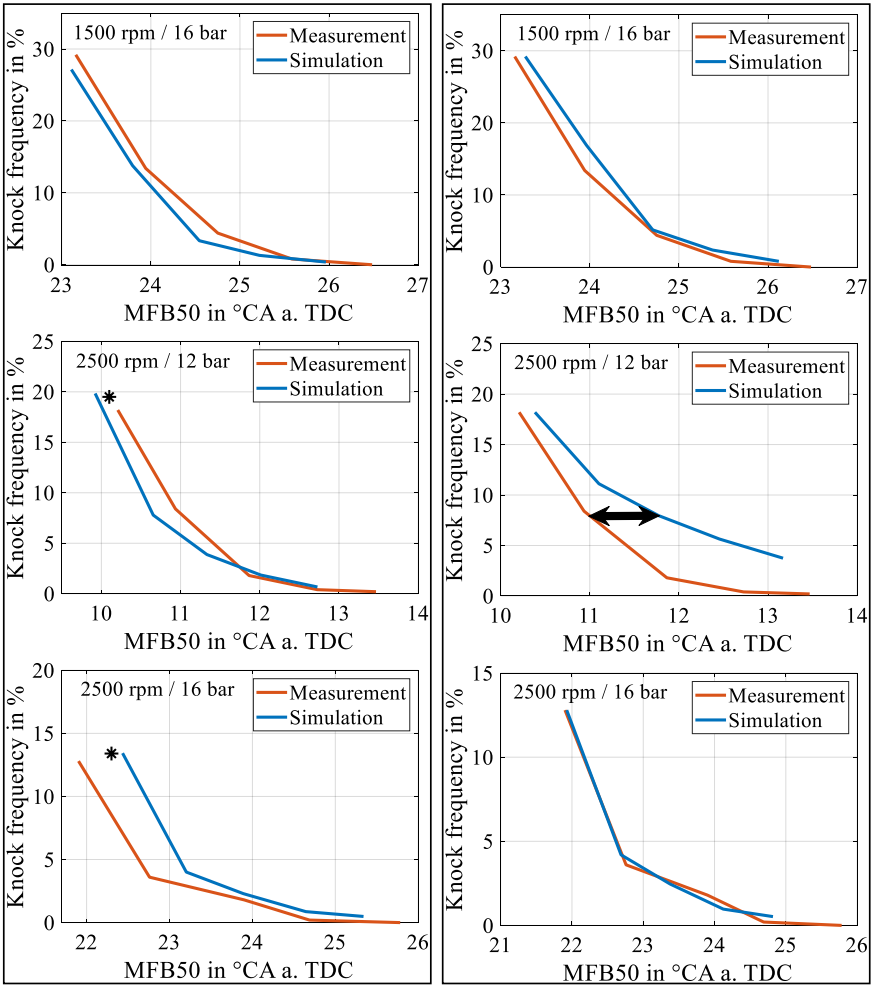

Figure 5.5: Calculated knock frequency in comparison to the measured knock frequency for simulation approach using a turbulence level distribution (a) and using a CCV-model, according to [69].

In Figure 5.6 the prediction accuracy is visualized by comparing the center of combustion of the simulations to the center of combustion of the interpol-

ated/extrapolated points for the measurements. This way, results exactly on the angle bisector indicate a perfect prediction of the specific knock frequency. Results above the angle bisector indicate an overestimation of the knock tendency since the same knock frequency is predicted for a later center of combustion compared to the center of combustion where it occurred within the measurement. Consequently, results under the angle bisector underestimate the knock tendency. For both simulation approaches, all 15 operating points covering the three different engine speeds and engine loads as well as the contained spark timing variations are included in the evaluation.

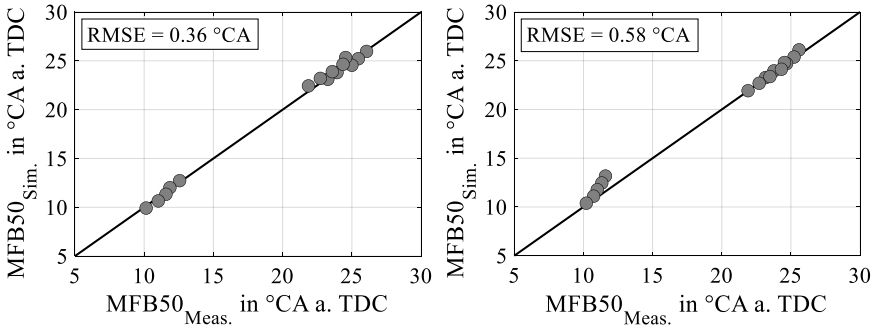

Figure 5.6: Evaluation of the predicted knock frequencies for the simulation approach using a turbulence level distribution (left) and using a CCV-model (right), according to [69].

Their small mean deviations of 0.36 °CA and 0.58 °CA for the first and second simulation method respectively, confirm a high accuracy of the predicted knock frequencies. The largest deviation of 1.6 °CA was found for the second simulation method at 2500 min^{-1} / 12 bar. Comparing this value to a mean accuracy of other knock models of approx. 2 °CA in [14] and 1.25 °CA in [61], 1.6 °CA as the single maximum deviation is still a good result.

Further investigation of the operating conditions where the largest deviation was observed, additionally, revealed a very small CCV at this particular engine speed and engine load. Evaluated by the standard deviation of IMEP, all five operating points at this engine speed and load have less than 40% of the cyclic fluctuations compared to any other of the 10 remaining operating points. Whereas the CCV-model calculates the cyclic variation correctly for the operating point with

the highest knock frequency, at which it was calibrated, the prediction accuracy decreases with increasing shift of the spark timing away from the calibrated spark timing. There are two possible reasons for this behavior.

The first one might be a non-optimal calibration of the CCV-model, considering that it is only calibrated at one operating point. However, the model provides two basic calibration parameters that each can be set independently from each other [42]. This is possible since they separately affect the prediction of the cyclic variations at low or high engine loads. For that reason, and the accurate results at the tuned operating point, a miscalibration can be ruled out. The second possible reason for the deviation might be that the overall CCVs are at such a small level that the limit of the prediction accuracy of the model is reached. This seems to be the most evident cause for the deviation, considering that the effect occurs at 12 bar, which is in the mid-range of the engine map, where CCVs can get very small. This is additionally supported by the observation of the significantly smaller measured variations at 12 bar compared to the variations observed at 16 bar. In total, this indicates that the deviations of the predicted knock frequencies at 2500 min^{-1} / 12 bar for the second simulation approach can rather be attributed to the inaccuracy of the CCV-model than inaccuracy of the simulation method or the Three-Parameter-Approach itself.

Comparing both simulation approaches, another important aspect to consider is the calculation performance. All simulations are performed locally as standalone working process calculations on a quad-core processor with 3.6 GHz each and 16 GB internal memory. This allows direct comparison of the simulation durations. The first simulation method required approximately 11 500 s / 3.2 h for the calculation of 500 cycles, whereas the simulation duration for the 15 cycles of the second simulation method was approx. 20 s, which is 575 times faster or a reduction of over 99.8%. One obvious reason for the significantly faster simulation is the smaller number of cycles. Yet, another difference is found by comparing the time per cycle. The second simulation method requires less time for one cycle with ~1.34 s/cycle, whereas the first method requires ~23 s/cycle. The reason for this are the different degrees of implementation. For the first simulation method, the working process calculation tool is started individually and consecutively for each SWC. This process was externally set up in a simple Matlab routine. The second simulation method requires only one single start for the calculation of all 15 cycles since the CCV-model is implemented in the Entrainment model. To sum up, both comparisons, by

entire simulation duration and time per cycle, show significant performance gain achieved by the second simulation method for an only marginal and negligible loss of accuracy.

Regarding the simulation approaches, the results confirm the general suitability of the Three-Parameter-Approach to predict the knock frequency, if the cycle-to-cycle variations are predicted with good accuracy. It is further important to note that both simulation approaches are calibrated only at the operating point with the highest knock frequency of each engine speed and load combination, similar to the calibration of AI_{Limit} for the knock frequency calculation. This way, all calibration is carried out at a single operating point and no further calibration to measurement data is required for all other operating points of each engine speed and load combination. This makes the knock frequency calculation an actual simulative prediction for these operating points.

For a complete predictability, including the operating points with the highest measured knock frequency, besides calibration of the simulation methods used to simulate single working cycles, AI_{Limit} would have to be determined phenomenologically. This could be a major challenge because as already pointed out by Hess in [15, 67] AI_{Limit} at this point does not have a comprehensible physical meaning. As shown in the introduction of the Three-Parameter-Approach (Figure 5.1), AI_{Limit} generally divides the single working cycles of an operating point into knocking and non-knocking cycles. Therefore, it seems obvious to refer to and define this limit as the knock limit. However, measurement results show that not exclusively cycles with the earliest auto-ignition onsets are necessarily the knocking cycles. This is not explicitly shown again in this work as it was already shown by Hess in [15, 67]. Hence, to avoid any confusion with the knock limit or knock boundary definition of current knock models, the description auto-ignition limit is better suited. With the current definition, especially within the second presented simulation method, AI_{Limit} rather has the character of a calibration parameter for the knock frequency calculation method, than a knock limit. Nevertheless, all current results indicate that the Three-Parameter-Approach including the current definition of AI_{Limit} is well suited for a knock frequency prediction.

From all previous investigations, the precise knock frequency prediction shows a great potential to improve knock control, since it provides a direct measure of the knock tendency instead of a binary evaluation if an operating point is

above or below the knock boundary. This could prove to be useful for knock control, where currently for conventional knock control the input signal is the information if knock has occurred in the preceding cycle or not. For that reason, in the second part of this work, the concept of a knock frequency based knock controller will be discussed. This includes an introduction to the basic control concept, the elaboration of the requirements for an engine application, a simulative investigation of the potential efficiency gain and an assessment of the robustness of the approach.

6 Knock Frequency Based Knock Control

6.1 Concept for Predictive Knock Control based on Knock Frequency

Knock control commonly used within serial applications, also referred to as conventional knock control, is characterized by immediate retardation of the spark timing if knocking is detected. If no knock has occurred, the spark timing is incrementally advanced after each non-knocking cycle, in much smaller increments compared to the retardation. This results in the typical sawtooth-shaped spark timing trace over time (ref. to Figure 6.1). Although this ensures the safe operation of spark-ignited engines and effectively prevents engine damage, it also includes some drawbacks. The much larger adjustment to later, less efficient spark timings and the slow gradual advance over more cycles results in the engine being operated for longer periods at spark timings later than the desired knock boundary. Besides the undesired shift of the mean spark timing, the large adjustment after knock detection leads to a wide variation of the spark timing in general. A tighter control can be realized by reducing the gains, especially for the spark retardation, but smaller gains also reduce the transient response capabilities of the controller [24]. Therefore, tuning of the conventional knock controller is always a trade-off between an acceptable variation of the spark timing and sufficient transient response capability.

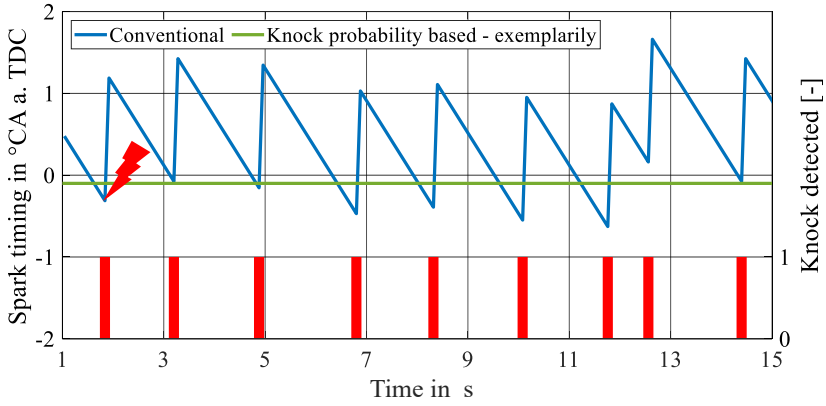

Figure 6.1: Exemplary spark timing adjustment with new knock frequency based knock control concept in comparison to conventional control during stationary operation.

Knock control based on the knock frequency/probability would avoid this deterministic behavior and overcome the trade-off difficulty. The knock frequency directly contains information about the probability that knock occurs in the next cycle under similar operating conditions. This way, the knock controller can allow knocking events without immediate retardation of the spark timing. This concept is exemplarily visualized in Figure 6.1 for stationary operation of an engine at the desired knock boundary. Whereas the conventional controller adjusts the spark timing after each knock event and thus cycles in and out of the knock limit, the new concept would allow operation without adjustment, since the engine is operated at the desired knock frequency.

Various knock control approaches have been published, aiming at an improvement of efficiency in comparison to conventional knock control. Pla [70] provides a good overview over many of these approaches. In [71], the binary classification into knock or no knock is extended by indeterminate cycles to reduce the chance of misclassification of knocking cycles. According to [72], this allows increasing of the control gains for a better transient response. A control scheme, combining an extremum seeking loop with a likelihood-based knock limit control loop, to maximize thermal efficiency is introduced in [73].

Further approaches with control algorithms that allow the occurrence of knock are the cumulative summation based stochastic knock controller [24] and the statistical likelihood based knock controller [74]. The cumulative summation based stochastic knock controller compares the number of measured knock events to an expectancy-value for the desired knock frequency over time. If the difference reaches a threshold, the spark timing is adjusted. It, therefore, requires the completion of multiple cycles. Within the statistical likelihood controller, spark timing adjustment is initialized based on a comparison of the knock occurrence probability under the measured knock frequency to the knock occurrence probability under the desired knock frequency. This controller is able to react instantly, but only if knocking occurs within a specific number of cycles. If no knock is detected although the knock frequency might be above the desired limit, a minimum amount of cycles is required before the controller adjusts the spark timing. Despite the generally good performance of these approaches, they rely on the detection of knock events and are rather reactive than predictive.

Knowledge about and direct control of the knock frequency allows instantaneous and predictive adjustment of the spark timing, independent from the occurrence of knock. This further also allows fast transient response for spark advance and spark retardation. There have been previous approaches to control knock based on the mean knock frequency or the knock intensity [75, 76], but as Peyton [24] pointed out, these concepts lack in their transient response behavior, due to the need for sizeable buffer and low pass filter to determine the required values with an acceptable degree of accuracy. Pla and co-workers shared the same observation in [70], that many stochastic methods for knock control show a good performance, especially during steady-state operation, but have a delayed response time in transient operations. This highlights the necessity for not only an accurate prediction of required control parameters but also an efficient and fast calculation of them.

With the results presented in this work, that demonstrated an accurate prediction of the knock frequency using the Three-Parameter-Approach, a control concept based on the knock frequency is introduced. The schematic structure of the new knock frequency based knock control concept is presented in Figure 6.2. The knock frequency is calculated with the Three-Parameter-Approach based on the parameters AI_{Limit}, AI_{mean} and σ_{AI}. The latter two are characteristic values describing the auto-ignition onset distribution of an operating point, thereby

including the cycle-to-cycle variations. AI_{Limit} is the calibrated auto-ignition limit, applied to the distribution to enable the knock frequency calculation. Within the control algorithm, the predicted knock frequency is directly compared to the target knock frequency in order to determine the appropriate spark timing adjustment.

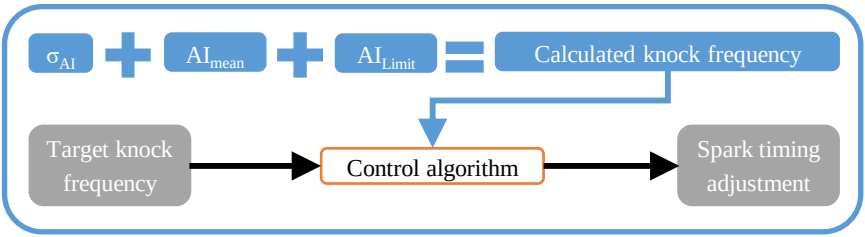

Figure 6.2: Schematic structure of the new knock frequency based knock controller.

The structure of the control algorithm is provided in Figure 6.3. The input parameters are the calculated knock frequency and the target knock frequency. The difference of the predicted knock frequency to the target knock frequency is compared to a tolerance value in the first step. Spark timing adjustment is only initialized if the difference of both input values exceeds the tolerance value. This allows accounting for small modeling inaccuracies and prevents unnecessary adjustments close to the target knock rate. Thus, the tolerance value is a calibration parameter that allows for tuning of the controller, to achieve the best response behavior for a specific prediction quality while preventing instability of the controller. If the deviation from the target knock rate exceeds the tolerance, the spark timing is either advanced or retarded, depending on whether the predicted knock frequency is above or below the target knock frequency. The final spark timing adjustment is determined by multiplication of the knock frequency deviation to the target frequency with the respective constant gain for spark advance K_{adv} or retardation K_{ret}. Including the difference of the input values in the adjustment allows precise control close to the desired limit and improves the fast transient response capabilities.

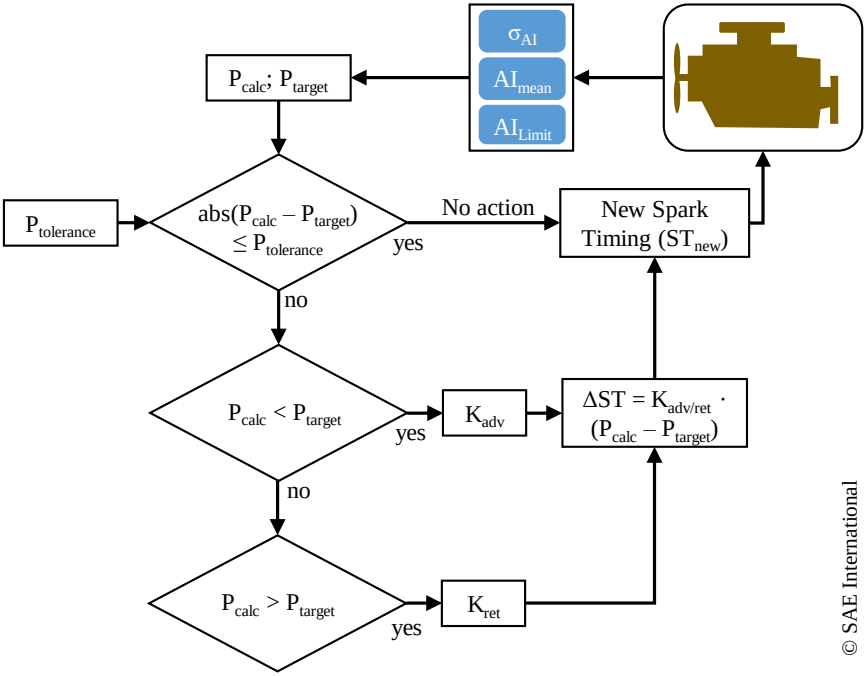

Figure 6.3: Schematic structure of the new knock frequency based knock controller, according to [77].

Since this work so far mainly focused on knock models and prediction of knock-relevant conditions, it is important to differentiate between the development of a knock model and the development of a knock controller because their requirements, available data and application differ significantly. Knock models are mainly used for engine concept development to reliably determine the KLSA of a large number of operating points across the engine map. During this early engine development stage usually, only few measurement data are available. For that reason, the predictive capabilities of these models are crucial. Although calculation performance of knock models is important, especially within 0D simulations, opposed to knock controllers, no real-time capability is required. For knock controllers however, real-time capability is crucial for efficient and fast transient operation. Further, knock controllers are usually developed in later stages of the engine development process or for existing engines. Thus,

comprehensive engine-specific measurement data usually is available or can be acquired from measurements.

In a first step, to identify the potential efficiency gain with the new control approach, the concept will be investigated via 0D simulations. The advantage of using simulations for the first estimation of the potential is that there is no risk of engine damage and although high calculation performance is desirable, in comparison to an engine application, real-time capability is not mandatory to allow an investigation. Therefore, in the following chapter, simulation models for conventional knock control and the new knock control concept are presented. The models enable comparison of the spark timing and thus the center of combustion over time under various operating conditions to evaluate the potential of the new control approach.

6.2 Simulative Investigation of Predictive Knock Control

6.2.1 Simulation of Conventional / Deterministic Knock Control

The simulative investigation is set up for the same single-cylinder research engine, which was part of the previous investigations, with a compression ratio of 10.76. The reason for the simulation of the single-cylinder engine instead of a multi-cylinder engine is the availability of the measured knock frequencies at various spark timings close to the knock boundary. This is required for the setup of the new control concept. An engine model of the single-cylinder engine is set up in GT-Suite [78] to simulate the air path. Gas exchange and combustion within the cylinder are simulated using the Entrainment model [40, 41], which can be implemented in the GT-Suite model via the FKFS UserCylinder® [79]. Input data for the Entrainment model are the boundary conditions, calculated from the air-path model at the time when the valves are open.

In order to be able to simulate conventional knock control, the identification of knocking cycles is crucial, since conventional knock control is based on the detection of knock. However, in 0D simulations, no pressure oscillations

and vibrations are modeled that would allow similar knock detection as on the test bench by pressure transducers or structure-borne sensors. To remedy the situation, a simple method, introduced by Peyton et al. in [24] is used to simulate knock events. This method is based on the assumption that knock events are binomially distributed, regardless of the underlying probability density function or the knock intensity [25].

Peyton and co-workers validated the assumption by evaluating the number of knock events contained in sets of 30 measured engine cycles at a knock frequency of 33% over 56 100 cycles, totaling 1870 sets. The resulting distribution is shown in the left histogram of Figure 6.4 marked as measurement. The same evaluation was performed for the simulated engine cycles from the proposed knock event simulation approach, marked as simulation in Figure 6.4 (left histogram). Both data sets are compared to the number of knock events predicted for a binomial distribution. The probability P_i of observing w knock events in i cycles at a given knock frequency f_k, for a binomial distribution, can be calculated according to Equation 6.1. The close agreement of all results confirmed the validity of the simulation method for the engine investigated by Peyton et al. [25].

$$P_i(w) = \binom{i}{w} {f_k}^w (1 - f_k)^{(i-w)} \tag{6.1}$$

The same validation was performed with measurement data of the single-cylinder engine to ensure the suitability of the knock event method for the data used in this project. Since the number of measured cycles at a single operating point is significantly smaller than the 56 100 cycles that were available to Peyton and co-workers, the set size is reduced from 30 to 10 and solely the operating point with the highest measured knock frequency of 24.8% is evaluated. An evaluation of operating points with even lower knock frequencies is not suitable because in combination with the reduced set size number the majority of sets would not contain any knocking cycle. Binomial distribution for such operating points could only be validated with a significantly larger number of cycles per set and a consequentially higher number of total measured cycles. The validation results for the operating point with 24.8% knock frequency at an engine speed and IMEP of 1500 min^{-1} and 20 bar respectively are shown on the right side of Figure 6.4. Considering the small number of measured cycles and the reduced set size, the results show a good agreement, confirming the validity of the simulation approach for the utilized data.

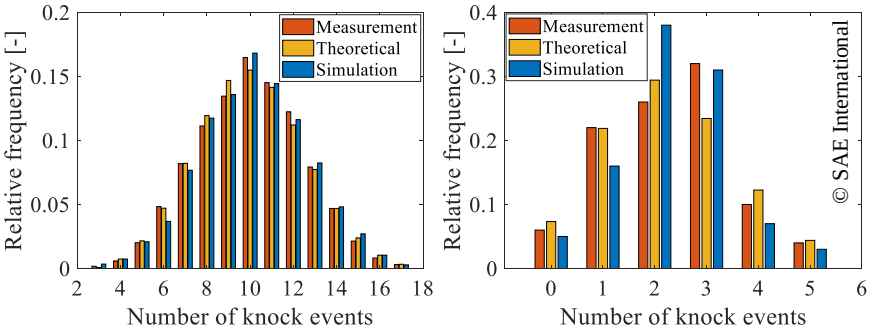

Figure 6.4: Validation of binomial distribution of knock events by Peyton et al. [25] (left) and measurement data of the single-cylinder engine investigated in this work (right), according to [77].

With the confirmed validation of the underlying assumption, knock events are simulated according to the structure presented in Figure 6.5. The current knock frequency is subtracted from one to yield the knocking threshold, which is applied to a random number between zero and one, provided by a uniform random number generator. The current knock frequency in this work is determined by interpolation of the measured knock frequency based on the engine speed, IMEP and the current spark timing. The random number determines if the cycle is knocking or not, depending on whether it is above or below the threshold.

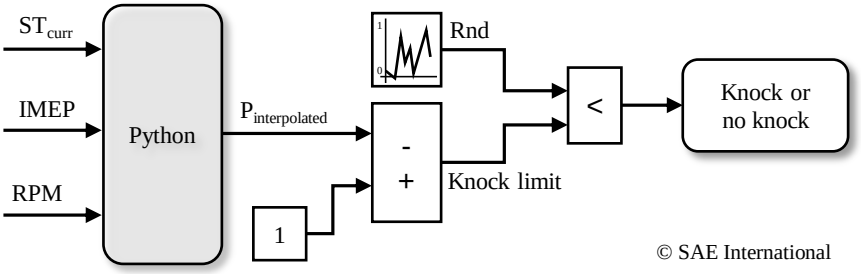

Figure 6.5: Knock event simulation structure, method analogous to [24], according to [77].

Interpolation of the current knock frequency is realized by a simple script written in Python, which is implemented in the GT-Suite model. The GT-Suite model provides the three input parameters and the interpolated knock frequency is returned. However, the available measurement data, exemplarily visualized for two engine loads in Figure 6.6a, are not sufficient for the simulation of knock control. As can be seen, the maximum knock frequency is 15% at 16 bar, which is not sufficient even under stationary operating conditions. If no knock occurs according to the knock event simulation at the maximum measured knock frequency, spark timing would be adjusted to an even earlier spark timing at which no measurement data is available. Thus, the controller either would fail to determine an appropriate adjustment or could only provide the maximum measured knock frequency although the spark timing has been further advanced. In any way, no realistic control is possible. For that reason, an exponential fit is applied to the five measured spark timings to extend the available data to knock frequencies between 0% and 100%, to account for the exponential increase of the knock frequency, see Figure 6.6b.

Further, the determination of the knock frequency is limited to the approximate engine loads and speeds available from the measurement data (ref. to Figure 6.6a). It has to be mentioned, that in theory, an interpolation to acquire a knock frequency for an engine load between the measured values is possible. However, triangulation-based linear interpolation of the 3D scattered data did not yield satisfactory results. Therefore, the data set is manually extended to cover engine speeds and loads in between the measured engine loads and speeds.

The result of the manual extension can be seen in Figure 6.6d with the knock frequency curves between the measurement data. For the manual extension, the exponential curve is shifted with respect to the spark timing where it reaches 100% knock frequency, as shown in Figure 6.6c. For example, creating new data for an IMEP of 14 bar, the spark timing where the knock frequency reaches 100% for the available 12 bar and 16 bar measurements and their exponential fits is evaluated first. The exponential fit is subsequently shifted in such a way, that the resulting 100% knock frequency spark timing is located exactly between the spark timing where the knock frequency reached 100% at 12 bar and 16 bar. Additionally, the fitting parameters describing the exponential fits are linearly interpolated to modify the shape of the exponential function, thus accounting for varying shapes of the exponential fits on the measurement data.

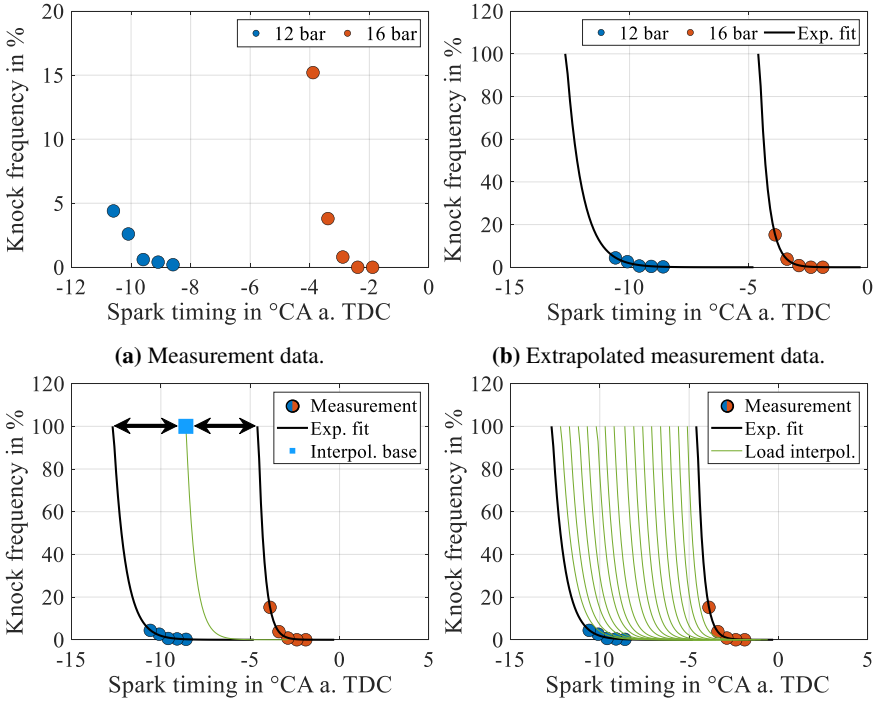

(a) Measurement data.

(b) Extrapolated measurement data.

(c) Basis of load interpolation.

(d) Fully extended data.

Figure 6.6: Extrapolation and interpolation method to extend measurement data to higher knock frequencies and higher load resolution – required for the knock frequency interpolation within the knock event simulation.

Using this approach, 15 datasets between the available engine loads and 7/11 datasets between the available engine speeds are created to increase the resolution of data to 0.25 bar and 125 min^{-1}. The different sized datasets for engine speed are required, since the available data cover 1500, 2500 and 4000 min^{-1}, thus two different ranges of 1000 min^{-1} and 1500 min^{-1}.

With the extended dataset and the high resolution, the triangulation approach is not required anymore and good interpolation results are acquired by applying the nearest point method. Moreover, the nearest point method interpolation is significantly faster compared to the linear approach. Due to the extrapolation and

interpolation of the available measurement data, determination of the current knock frequency is not limited to the spark timings, engine loads and engine speeds contained in the measurement data. Thus, knock events and therefore conventional knock control can be realistically simulated without restrictions to the measurement data as described above.

Besides the knock event simulation, two gains for spark retardation K_{ret} and advance K_{adv} are defined. They are related to each other by the target knock frequency, according to Equation 2.7. The target knock frequency for the simulative investigation of the two knock controllers is set to 5%, which also refers to the lower limit of the knock boundary definition with 4-10% knock frequency.

The gains could be directly applied to the current spark timing, depending on the knock event signal to either advance the spark by a small increment or retard it by a larger one. This would result in the typical sawtooth trace of the spark timing over time and would be sufficient for evaluation of solely stationary engine operation. However, this basic implementation is not suitable for the evaluation of transient behavior, since the spark timing could only be adjusted by the fixed increments. For a transient change, for example to a lower knock frequency, this means, the knock controller has a very slow response because the spark timing can only be advanced by the small increment K_{adv} if no knock occurred. Regarding a transient change to a higher knock frequency, the controller response would be faster due to the larger increment K_{ret} but almost every cycle during the transient change would be knocking.

As introduced in Chapter 2.2 and described in further detail in [9], therefore, an adaptive map is contained within the knock controller that enables faster transient response and the possibility to account for further knock-relevant effects such as the fuel quality and aging of the engine. For this reason, to realistically simulate conventional knock control, the spark timing for the next cycle ST_{new} in this work is calculated as follows:

$$ST_{new} = ST_{base} + (ST_{incr})_{continuous} \tag{6.2}$$

An engine map that contains the spark timings at the lower end of the knock boundary referring to 1% knock frequency provides the base spark timing ST_{base} based on the engine speed and IMEP. This engine map represents a simplified non-adaptive version of the previously mentioned adaptive engine

map. Within this investigation, the simplified non-adaptive setup is justified, as only one fuel is investigated and no further effects such as aging of the engine have to be accounted for.

The base spark timing is determined for the subsequent engine cycle, thus providing an appropriate base spark timing, which prevents the above-described effect of continuously knocking cycles or the slow advance of the spark timing during transient conditions. In the simulation, the IMEP of the upcoming cycle is estimated based on the intake pressure. The respective intake pressure is determined based on its initial and its target value, representative of the initial and commanded/target engine load. To the base spark timing, a spark timing increment ST_{incr} is added. This parameter contains the continuous summation of the increments K_{adv} and K_{ret} depending on whether knock occurred or not.

This setup enables more realistic spark timing control during transient conditions while maintaining similar control abilities during stationary operation compared to the control approach without a base spark. Thus, not only stationary operation but also transient conditions can be investigated. This includes load steps and initial transient controller response, by activating the controller at a spark timing different to the target spark timing. Simulations using this model will act as the comparison basis for the new knock frequency based control concept. In the following section, the simulation model for this new knock control concept will be introduced.

6.2.2 Simulation of Predictive Knock Control

The new predictive knock control approach is based on the knock frequency calculation using the Three-Parameter-Approach as shown in Figure 6.2. Thus, the three parameters AI_{Limit}, AI_{mean} and σ_{AI} have to be available at each engine cycle to allow calculation of the knock frequency.

In Chapter 5.2 it was shown that σ_{AI} can be determined phenomenologically, however, the calculation is too slow not only for an engine application but also for the simulation of many cycles, since multiple cycles have to be calculated for a single operating point. For this reason σ_{AI} is stored in an engine map and is determined based on the engine speed, IMEP and the current spark timing. This map contains engine-specific σ_{AI} values and allows fast determination,

since the CCV information is directly stored within the engine map and does not have to be acquired by simulation of multiple cycles.

It has to be mentioned, that the parameter is still phenomenologically based on the cycle-to-cycle variations and could be determined from simulation of those. Storing the data directly in an engine map is a measure to provide the required parameter fast enough for the control application. Moreover, utilizing the measured cycle-to-cycle results is convenient, since both simulation and engine application require measurement of the knock frequency at the test bench to be able to calibrate the knock frequency calculation. Therefore, an automated determination of the knock boundary for various engine speeds and loads with higher resolution than the available data in this project would directly provide the required data for the setup of the σ_{AI} lookup table.

The second parameter, AI_{mean}, for the control application, is defined as the auto-ignition onset of the average working cycle of an operating point. This definition slightly differs from the original definition, where AI_{mean} was defined as the arithmetical mean of the auto-ignition onsets of all single working cycles of an operating point. Although both definitions include a mean value of the included single working cycles, it is important to note that the application of the two-stage auto-ignition model on the averaged pressure trace does not yield the same auto-ignition onset as averaging the auto-ignition onsets determined for each single working cycle. The resulting small difference is not concerning, as it can be compensated by the third parameter AI_{Limit}. Similarly to the method described in Chapter 5.2, AI_{Limit} is calibrated iteratively by applying the Three-Parameter-Approach and adjusting AI_{Limit} until the calculated knock frequency based on AI_{mean}, AI_{Limit} and σ_{AI} matches the measured knock frequency. Thus, calibration of AI_{Limit} accounts for the small difference of AI_{mean}.

Further, analogous to σ_{AI}, this new definition allows the determination of AI_{mean} without the simulation of multiple cycles. Consequentially, the mean engine cycle for the respective operating conditions is required in the simulation but also within an engine application of the controller. While the determination of the mean cycle is straightforward in the simulation, as the Entrainment model directly provides the average working cycle of specific operating conditions, it is challenging for a real engine application. The requirements for a successful engine application shall not be further explained here, as they are discussed

in further detail in Chapter 6.4. In the simulation, the two-stage auto-ignition model is used to determine the auto-ignition onset of the simulated engine cycle and thus directly provides AI_{mean} of the respective cycle.

The third parameter AI_{Limit} is, as mentioned, crucial as it allows calibration of the knock frequency calculation to the measured knock frequencies. It is therefore convenient to store the values of this parameter as engine-specific lookup table. Similar, to σ_{AI}, AI_{Limit} is determined based on the engine speed, IMEP and the current spark timing. The contained values of AI_{Limit} are calibrated as described above, to allow precise calculation of the measured knock frequencies using σ_{AI} from the lookup table based on the measured cycle-to-cycle variations and the auto-ignition onset of the mean cycle as AI_{mean}. In oppose to the simulative investigation of the calculation approach in Chapter 5.2 where the overall predictive abilities of the Three-Parameter-Approach were of interest, here, AI_{Limit} is not solely calibrated at the spark timings with the highest knock frequencies but each included spark timing. This allows a precise calculation of the knock frequency at each operating point and consequently an accurate investigation of the potential of the new control approach. Additionally, as mentioned before, the general predictive abilities requiring calibration at only a few operating points are important during the early stages of the engine development but are not the main focus for a knock control application.

With all three parameters available, similar to the conventional controller, the new control approach aims to determine the knock frequency of the subsequent engine cycle in order to be able to make an appropriate predictive adjustment of the spark timing. AI_{Limit} and σ_{AI} are lookup tables based on the same input parameters as the knock frequency interpolation for the knock event simulation within the simulation model of the conventional controller. This enables prediction of both parameters for the upcoming cycle by estimation of the engine load for the next engine cycle, based on the intake pressure, similarly as described in the previous chapter for the conventional controller. By estimating the engine load, the two values of AI_{Limit} and σ_{AI} are representative for the operating conditions of the upcoming engine cycle, assuming the spark timing would not be adjusted. The third parameter AI_{mean}, however, is only available for the completed engine cycle, as the auto-ignition model, implemented in the Entrainment model, determines the auto-ignition onset during the combustion calculation. For that reason, no estimation of the auto-ignition onset due to the changing engine load for an upcoming cycle is possible without actual

calculation of the respective cycle. That means, in total, within the new control approach, the calculated knock frequency can be interpreted as the potential knock frequency of the upcoming cycle with different engine load as well as unchanged spark timing and auto-ignition onset.

The calculation of the knock frequency is embedded in the controller structure, as shown in Figure 6.7. Analogous to the conventional controller, the required interpolations and the knock frequency calculation are implemented by a simple script written in Python. Engine speed, estimated engine load, spark timing and now additionally AI_{mean} are the input parameters to this python module. Within this module, σ_{AI} and AI_{Limit} are determined from the stored lookup tables and from all three parameters including AI_{mean}, using the Three-Parameter-Approach, the final knock frequency is calculated and returned to the GT-Suite model.

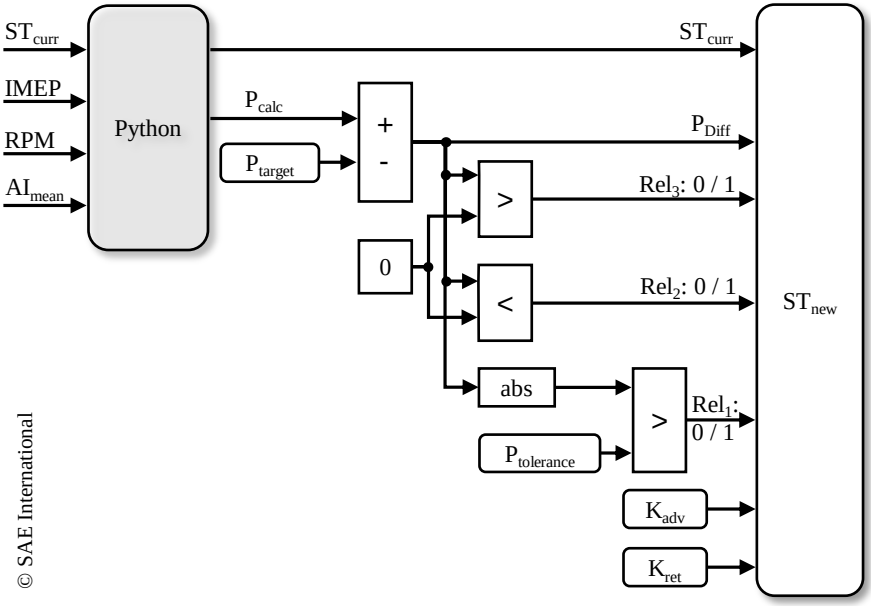

Figure 6.7: Calculation of the spark timing for knock frequency based knock control, according to [77].

The subsequent modules evaluate the difference between the calculated and the target knock frequency and determine three relational operators that are either one or zero. Rel_1 indicates if the tolerance threshold is exceeded and Rel_2 and Rel_3 indicate which gain has to be applied. Within the final module, the new spark timing for the next engine cycle is calculated based on the current spark timing, the difference of the calculated and the target knock frequency P_{Diff}, the gains and the relational operators according to Equation 6.3.

$$ST_{new} = ST_{curr} + (P_{Diff} \cdot Rel_1)(K_{adv} \cdot Rel_2 + K_{ret} \cdot Rel_3) \tag{6.3}$$

Similarly to the interpolation of the knock frequency within the knock event simulation, the available measurement data for the σ_{AI} and thus also the AI_{Limit} lookup table is not sufficient to ensure proper operation of the controller due to the limited maximum contained knock frequencies. For this reason, the available data has to be extrapolated as well, to cover a larger range of knock frequencies for a certain engine speed and load.

The basis for this extrapolation are the exponential fits of the measured knock frequencies over the respective spark timings (ref. to Figure 6.6b). Based on these fits, spark timing ranges with a resolution of 0.1 °CA are defined that cover knock frequencies of > 0.001% up to the last spark timing with a knock frequency below 100%. In Figure 6.6b for example at 12 bar IMEP, this spark timing range covers values between −12.6 °CA and −5.2 °CA. Subsequently, simulations at all spark timings contained in these ranges are performed and their auto-ignition onsets are determined by the auto-ignition model. As shown by the simulation data in Figure 6.8a, this increases the resolution of available AI_{mean} data in the measured range and extends it to the 0.001-100% knock frequency range. Good agreement of the measurement data to the simulation results at the five discrete spark timings indicates a precise representation of the real engine. The linear fit to the simulation data indicated by the dashed line and the red marker are incidental for now. They will be relevant for the later explanation of the spark timing regions with constant auto-ignition onsets.

In order to extend the data of the second parameter, σ_{AI}, a linear fit to the available values of σ_{AI} from the measurement data is applied, as shown in Figure 6.8b. This allows determination of σ_{AI} in the extended knock frequency and respective spark timing range. Lastly, presented in Figure 6.8c, AI_{Limit} is determined for the new spark timing range by iterative calibration, as described above, whereas now calibration is performed based on the knock frequencies

determined by the exponential fits instead of the measured knock frequencies. This way, the knock frequency calculation is calibrated for the extended knock frequency range.

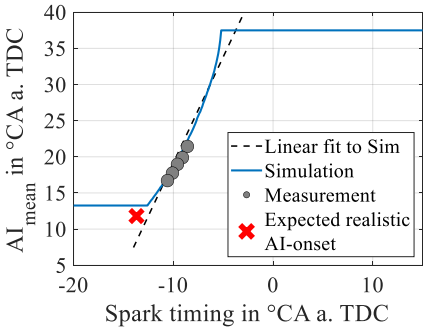

(a) AI_{mean} from simulation.

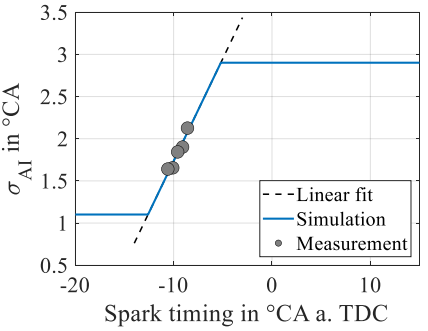

(b) σ_{AI} from measurement data.

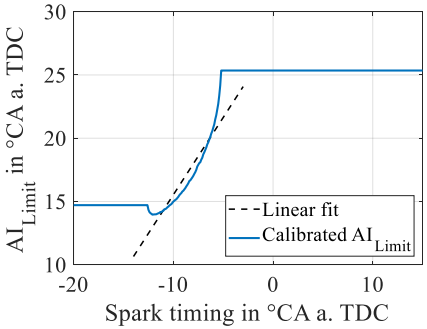

(c) Calibrated AI_{Limit}.

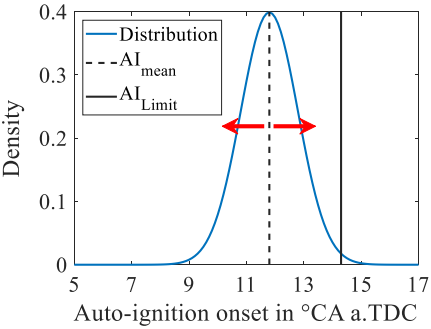

(d) Exemplary distribution.

Figure 6.8: Extension of AI_{mean}, σ_{AI} and AI_{Limit} (a)-(c) to consider a *ST* range that refers to 0.001-100% knock frequency, and exemplary distribution (d) of auto-ignition onsets to explain const. values of the three parameters for *ST*s exceeding the 0.001-100% knock frequency.

As can be seen in Figure 6.8, the spark timing range of σ_{AI} and AI_{Limit} is even further increased, exceeding the 0.001-100% knock frequency. This enables the use of similar spark timing ranges for all operating conditions included in the lookup tables. Moreover, it is obvious that both σ_{AI} and AI_{Limit} are kept

constant for this exceeding spark timing range. This has physical and modeling reasons.

Applying a linear fit of σ_{AI} over the entire range is not reasonable, because the cycle-to-cycle variation will not drop below a minimum value and will never reach zero or negative values. Even extremely small but positive values would relate to a very narrow distribution function, thus making the knock frequency calculation extremely sensitive to inaccuarcies of AI_{mean}. Additionally, the maximum cycle-to-cycle variation is a finite value and will not infinitely increase. Regarding AI_{mean}, the auto-ignition onset will not shift to later times infinitely, as at some point for a late ignition timing no auto-ignition will occur anymore. Shifting the spark timing to earlier ignition, as can be seen from Figure 6.8a, the auto-ignition onset will rather approach a constant value than shift to earlier timings linearly.

From a modeling point of view, if AI_{mean} and σ_{AI} were extrapolated linearly over the entire range, also the calibrated limit would further progress to earlier and later values, as indicated by the dashed lines in Figure 6.8c, to keep the calculated values of the knock frequency at 0.001% and 100%. However, due to the apparent non-linearity of AI_{mean} over the spark timing, calibration of AI_{Limit} to linearly extrapolated σ_{AI} and AI_{mean} could yield significant modeling errors if the auto-ignition of an operating point would deviate from the extrapolated value.

For example, if an extremely early spark timing occurred and the respective auto-ignition would occur later than the linear interpolation (indicated by the red marker in Figure 6.8a), the resulting knock frequency would decrease to a lower value than the calibrated maximum knock frequency close to 100%. This can easily be seen by the schematic visualization of the knock frequency calculation in Figure 6.8d. All parameters, σ_{AI}, AI_{mean}, and AI_{Limit} are calibrated to yield a knock frequency close to 100% at this spark timing. If AI_{mean} would occur later, that would refer to a shift of the distribution function to the right, while AI_{Limit} and σ_{AI} would remain similar. Thus, AI_{Limit} would shift relative to the position of the distribution in such way, that the resulting knock frequency would decrease compared to the initial conditions. That means the calculated knock frequency could decrease when the spark timing is further advanced than the spark timing referring to the maximum knock frequency determined by the exponential fit. This is physically not reasonable. For that reason, a constant

value of σ_{AI}, AI_{mean} and consequentially also AI_{Limit} is better suited for spark timings that exceed the initial 0.001-100% knock frequency range.

As obvious from the progress of AI_{mean}, advancing the spark timing would in reality result in earlier auto-ignition onsets. As a consequence and in oppose to the linear extrapolation, the constant AI_{mean} value for early spark timings (exceeding the spark timing that relates to 100% knock frequency) is now always later than the real auto-ignition onset. In Figure 6.8d, the effect on the calculated knock frequency for the same scenario as previously is then indicated by a shift of the distribution to the left. Hence, AI_{Limit} shifts to the right, relative to the distribution function, and increases the calculated knock frequency. However, since the initial conditions were already close to 100% knock frequency, the resulting increase is small and even smaller for further relative shifts. This way, the calculated knock frequency remains at a knock frequency close to 100%.

For completion, it has to be noted, that the assumption of a constant AI_{mean} for various spark timings is not physically correct and a linear fit would yield better results from a physical point of view. Nevertheless, the assumption, in this case, is justified because it ensures the physically correct modeling of the knock frequency for significantly varying spark timings. To sum up in simple words, the constant values of σ_{AI} and AI_{Limit} outside the 0.001-100% knock frequency range ensure that outside of this range the calculated knock frequency cannot drop below 100%, even if the spark timing is further advanced. Similarly, the calculated knock frequency cannot increase above 0.001% even if the spark timing is further retarded.

Besides the extrapolation to cover a larger knock frequency range, also analogous to the conventional controller, the data has to be extended to increase the resolution regarding engine speed and load. To keep the simulative effort low, simple linear interpolation was used to extend the data. Whereas σ_{AI} was already interpolated linearily, AI_{mean} and AI_{Limit} are now also interpolated linearly. This approach is shown for AI_{mean} in Figure 6.9 (top left). The linear fits created from the simulation data are the basis to determine a new representative linear progress of AI_{mean} for the respective new engine load (indicated by the green curve). The process is similar for σ_{AI} and AI_{Limit}, resulting in a linear curve of both these parameters for the extended data covering additional engine loads, as indicated in the upper plots of Figure 6.9.

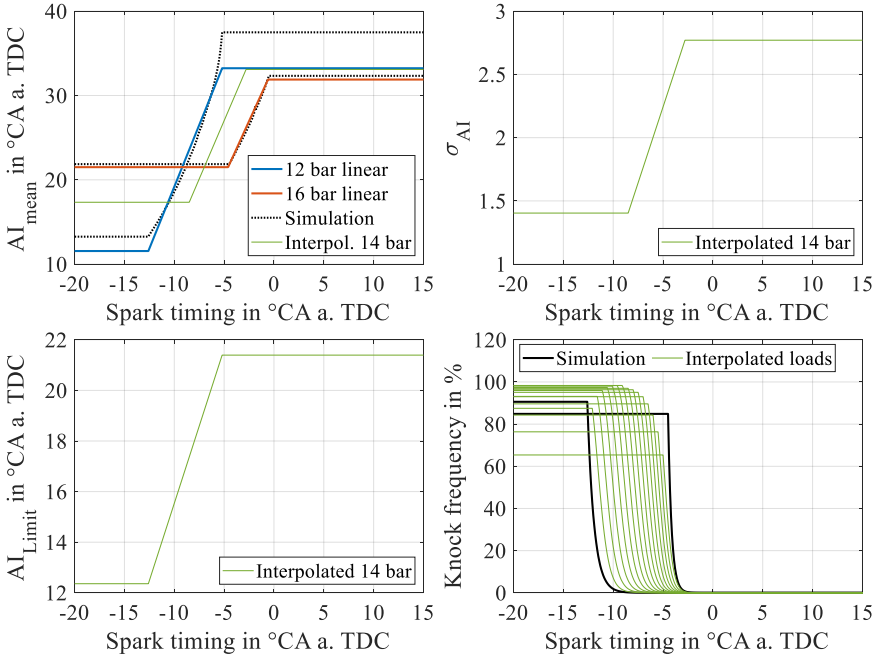

Figure 6.9: Interpolation of AI_{mean}, σ_{AI} and AI_{Limit} to allow knock frequency prediction at engine loads between measured loads.

In the subsequent step, linear interpolation is used to determine the spark timing where the knock frequency should reach 100% and the spark timing range that should cover 0.001% to 100% knock frequency for the specific new engine speed and load. Finally, the linear functions of AI_{mean}, σ_{AI} and AI_{Limit} are evaluated for the respective spark timing range and the values exceeding this range are again kept constant. This provides simplified data for σ_{AI} and AI_{Limit} with a progress as shown by the respective green curves in Figure 6.9 (top right, bottom left), that are included in the lookup tables to increase the resolution.

At the engine loads where measurement and simulation data is available, 12 bar and 16 bar in the presented example, the lookup table for AI_{Limit} and σ_{AI} contains the detailed simulation data and not the linear fits. Only for the additional data covering further engine loads, linear parameters are used. Thus, precise prediction of the knock frequency can be expected for stationary

operation at engine loads that are covered by detailed simulation data for the required parameters. Although for transient loads, due to the linear approach, the prediction will be less accurate, a significant increase in prediction accuracy can be expected compared to knock frequency prediction for transient loads without any additional data between the measured engine loads.

In order to verify the suitability of the extension method, the interpolated values of all three parameters are used to calculate the knock frequencies of all included spark timings. In Figure 6.9 (bottom right) these results are exemplarily presented for various loads between 12 bar and 16 bar at an engine speed of $2500\,\mathrm{min}^{-1}$. The outer curves belong to the engine loads of 12 bar and 16 bar. The curves in between represent the calculated knock frequencies based on the new interpolated data. The varying maximum knock frequencies are attributed to the resolution of the spark timing in 0.1 °CA, possible inaccuracies due to the simple method to determine the spark timing range for 0.001-100% knock frequency that is allocated to the specific loads and due to the simplified linear approach for the underlying three parameters. However, the contained variation of the maximum values is unproblematic, since such high knock frequencies are expected to be rarely or not reached during operation. Hence, the interpolated values to extend the lookup table provide crucial data for precise simulation of knock control during transient operation.

As previously mentioned, measurements of the knock frequency with sufficient resolution across the engine map could significantly reduce the number of interpolations that are required to provide σ_{AI} and AI_{Limit} with appropriate resolutions. Thus, the creation of the engine maps could be simplified to the extrapolation of data to cover larger ranges of knock frequencies at each engine speed and load. The additional interpolation used in this work is required to allow the potential of the controller to be studied as accurately as possible. Finally, it has to be stressed, that the interpolation between the available engine speeds and loads is crucial for the investigation of transient operation but simultaneously does not affect the results and accuracy of the controller during stationary operation. That means the presented setup allows investigation of the new knock frequency based knock controller under stationary and transient operating conditions. In the following chapter, therefore, engine operation using the conventional and the knock frequency based knock controller are compared under various operating conditions, to identify the fuel-saving and emission-reduction potential of the new control approach.

6.3 Evaluation of the Predictive Knock Control Approach

In the first step, the two controllers are compared under stationary engine operation. The conventional controller is tuned to allow operation at a knock frequency of 5%. This is achieved by adjusting the gains respectively. Within the knock frequency based controller this is achieved by setting the target knock frequency to 5%. At each operating point, 500 knock-controlled engine cycles are simulated. During the first 5 cycles of each simulation, the controllers are deactivated to allow the simulation model to converge first. For the 500 simulated cycles at each operating point, the knock event simulation revealed between 24 and 25 knocking events, which refers to a knock frequency of 4.8% and 5% respectively. This confirms appropriate tuning of the gains for the conventional knock controller.

For the new controller, the tolerance frequency is set to 1%, thus allowing a calculated knock frequency of 4-6% without adjusting the spark timing. The two gains for retardation and advance are set to 0.03 and 0.24 respectively. In comparison to the conventional controller, the gains within the knock frequency based controller are independent of each other and account for the exponential rise of the knock frequency over the spark timing. Due to this exponential behavior, only a smaller spark timing adjustment is required to reduce the knock frequency for example from 9% to 5%, than would be required to increase the knock frequency by the same amount from 1% to 5%. Hence, different gains are required to allow fast adjustment to the target in both directions. As the exponential rise is not exactly similar for all operating points, the best results for the gains are achieved by considering all operating points for tuning. This allows best control results for the included different conditions and prevents instabilities or avoidable slow control responses for individual operating points.

In order to investigate not solely the control response under strictly stationary engine operation, two different simulations are set up, where the spark timing is deliberately initialized earlier and later compared to the spark timing referring to 5% knock frequency. With this setup, not only the control over time during stationary operation but also the initial control response can be compared and evaluated. Figure 6.10 shows the progress of the center of combustion at $2500\,\mathrm{min}^{-1}$ and 16 bar IMEP, for late and early initialized spark timing. The

calculated knock frequency contained within the new controller visualized on the second y-axis indicates the low and high knock frequency respectively for the different initialized spark timings before the controllers are activated. The progress of the knock frequency further highlights the fast and precise adjustment of the spark timing and thus the center of combustion towards the target value at 5% knock frequency.

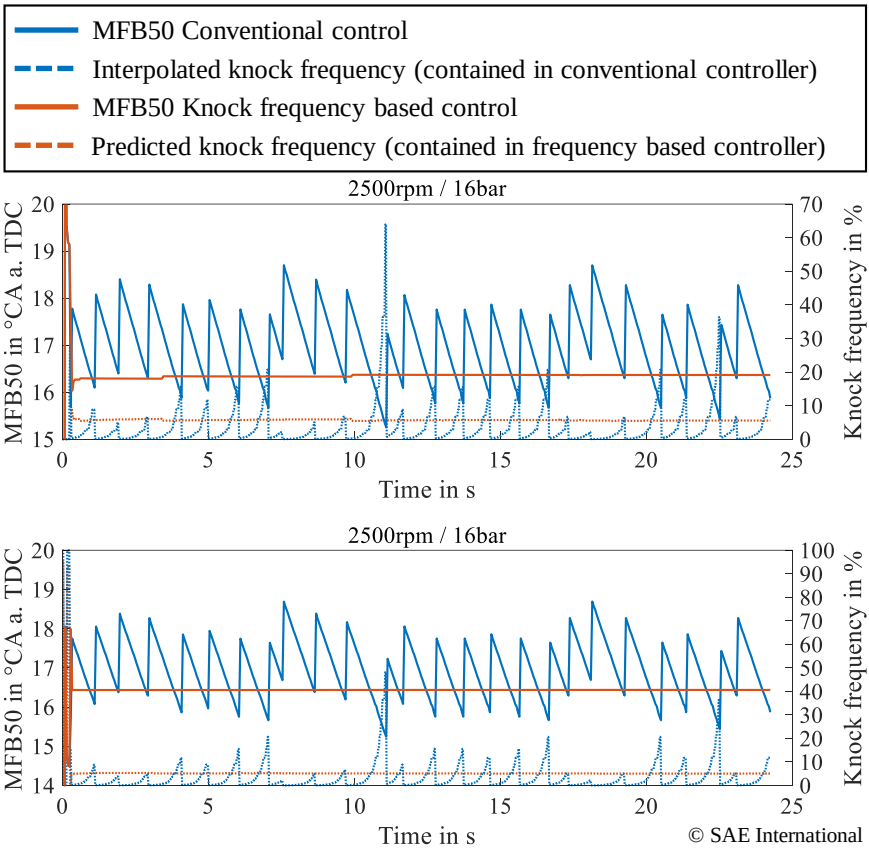

Figure 6.10: MFB50 over time for conventional and knock frequency based knock control and the underlying calculated knock frequency. Simulation initialized and controller activated at a low knock frequency (top) and at a high knock frequency (bottom), according to [77].

For a more detailed analysis of the initial control response, the time difference between both controllers to reach within 0.5 °CA to the center of combustion at 5% knock frequency is evaluated. The results show similar behavior for activation at low and high knock frequency and are presented for one load at each investigated engine speed in Figure 6.11. Results of all engine speeds and loads are summarized in Appendix A.5. As apparent, the knock frequency based controller has a precise and instantaneous response whereas the conventional controller requires several more cycles to reach within 0.5 °CA of the target value. In total, for activation at low knock frequency, the new controller required 6-22 cycles or 0.1-0.8 s less than the conventional controller to reach within 0.5 °CA to the target center of combustion.

For activation at high knock frequency, both controllers retard the spark timing immediately after activation of the controller to avoid engine-damaging high knock frequencies in the following engine cycles. The conventional controller shifts the center of combustion to a safe value at the lower limit of the knock boundary and subsequently advances again by the small increments. The knock frequency based controller more precisely retards the center of combustion to the target value already within the first cycle after activation. Even if, in the first cycle, the center of combustion is retarded further to a low knock frequency, in the subsequent cycles it is rapidly advanced towards the target value. This can be seen for example at an engine speed and load of 2500 min^{-1} and 16 bar in Figure 6.11, where both controllers show similar initial retardation and the new controller immediately advances the center of combustion again close to the target value. This allows the new controller to adjust the center of combustion faster towards the target value compared to the conventional controller. From this behavior, the new controller yields a similar 3-23 cycles or 0.1-0.9 s time advantage for controller activation at a high knock frequency.

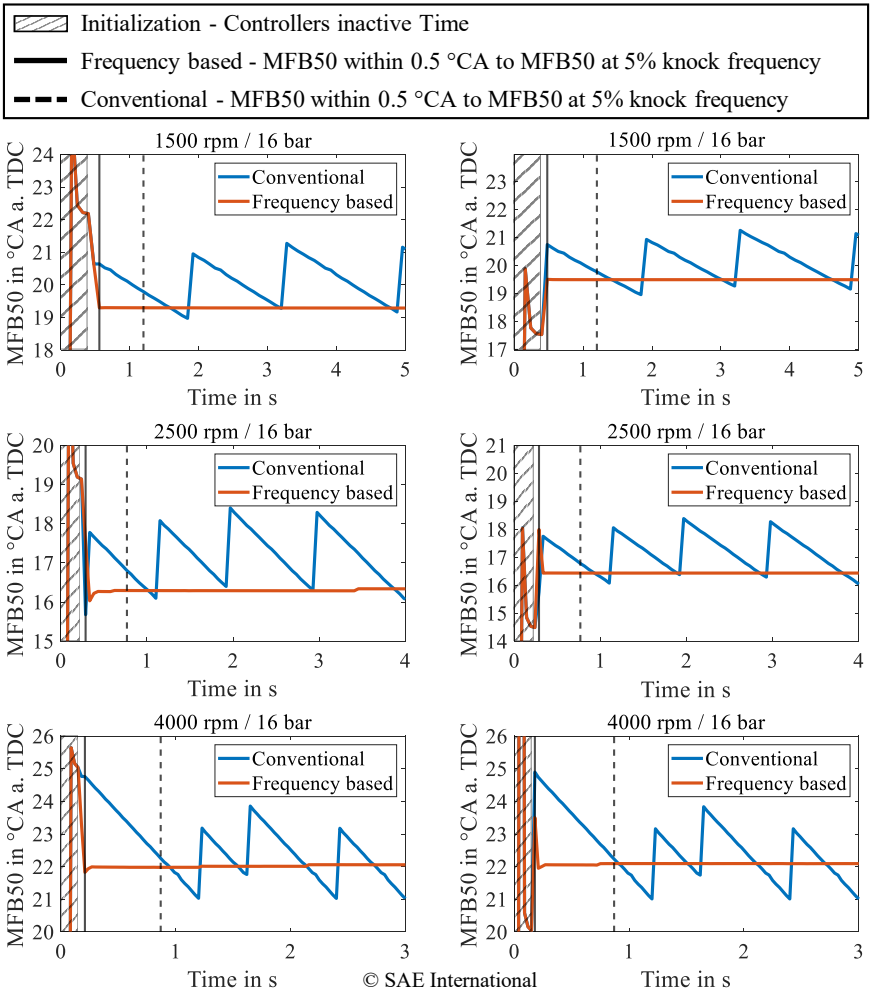

Figure 6.11: Initial controller response for controller activation at low knock frequency (left) and high knock frequency (right), according to [77].

Besides the faster initial response, a further efficiency gain is expected from reduced variability of the center of combustion over time. Therefore, the center of combustion distributions including all 500 engine cycles are investigated. Histograms of the distributions are presented in Figure 6.12 and show the same

operating points as in Figure 6.11, since the general obervations were equal for all OPs. Again results including all OPs are summarized in Appendix A.5.

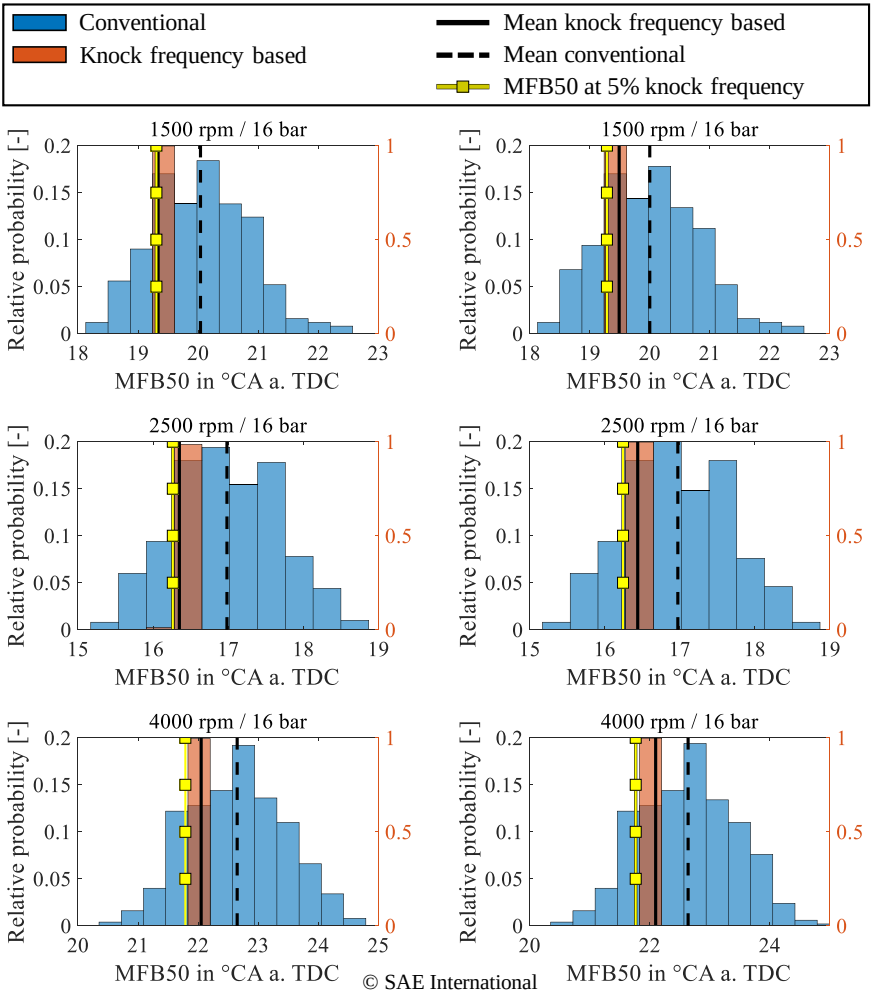

Figure 6.12: MFB50 distribution for controller activation at low knock frequency (left) and high knock frequency (right), according to [77].

As can be seen, the new knock frequency based control approach shows a significantly reduced variation of the contained center of combustion values. Hence, the relative probability for the new controller is given on a second y-axis with different scaling, to allow direct comparison. Moreover, the comparison shows that the mean center of combustion for the new controller is closer to the target center of combustion. The mean value of the conventional controller, as described in Chapter 6.1, deviates further from the target value and is shifted to a later time due to the different increments for spark advance and retardation. Considering all operating points, for controller activation at low knock frequency, the mean value for conventional control deviates by 0.6-0.9 °CA from the target value, whereas the deviation for the knock frequency based controller is 0.02-0.3 °CA. Thus, the maximum deviation could be reduced by almost 67%. The controller activation at high knock frequency reveals an equal reduction of the variability and shift of the mean value closer to the target center of combustion. In total, both effects, the smaller variation and the mean value closer to the target center of combustion improve the efficiency by operating the engine closer to the most efficient conditions with respect to knocking.

In the next step, transient behavior during load steps between the available engine loads 12 bar, 16 bar and 20 bar are investigated (see Figure 6.13). To enable investigation of the new knock control approach under transient conditions imposed wall temperatures instead of a wall temperature solver have to be used. The imposed temperatures enable linear adaption during the transient phase, between the converged wall temperatures under stationary operation. This is required, as all available data and thus all parameters for the knock frequency prediction are solely based on the measurement of stationary operating conditions. The, thereby introduced, simplification of the simulation is, therefore, essential to enable an investigation of transient conditions. Such limitation as well as the requirements regarding an engine application are discussed in the subsequent chapter in further detail.

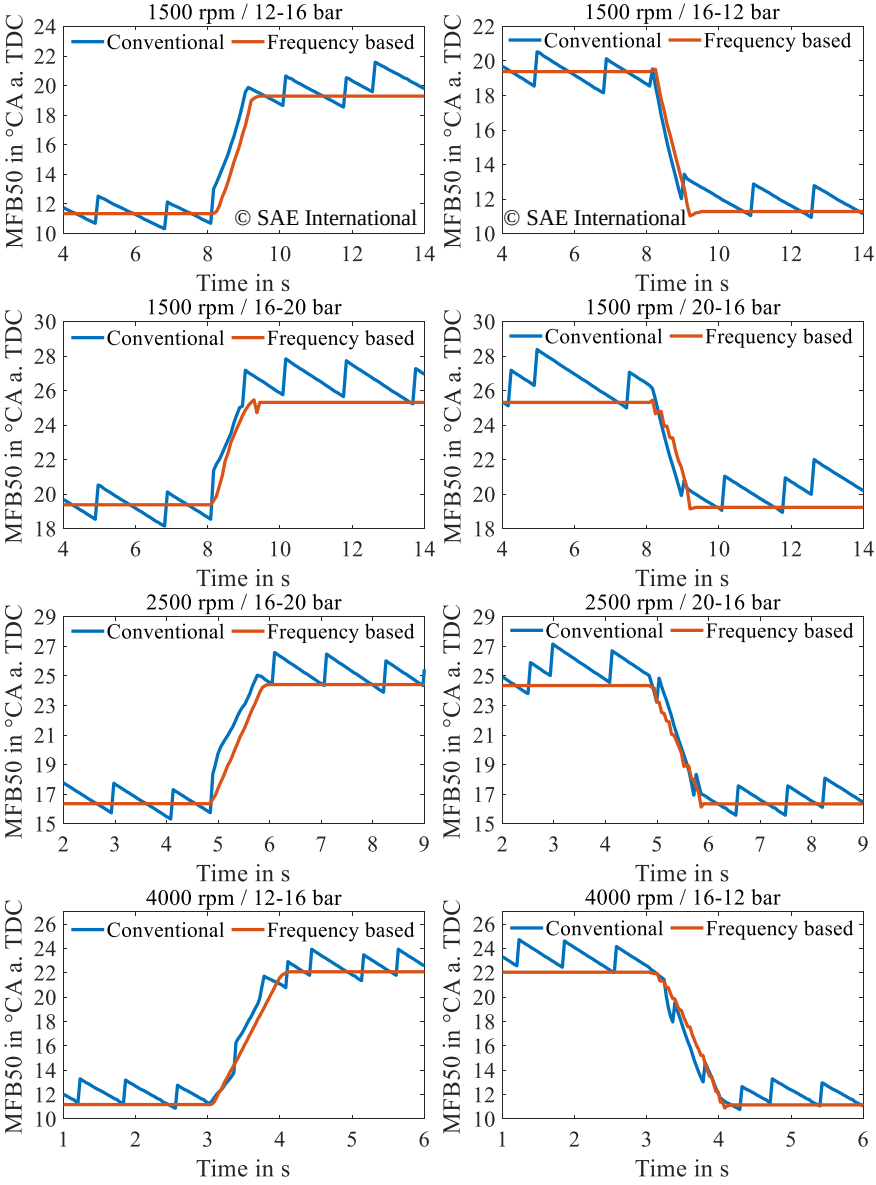

Figure 6.13: Comparison of the control response of conventional and knock frequency based knock controller under transient load change, with data from [77].

During a load increase, both controllers show a fast transient and comparable adjustment of the spark timing with similar rates with which the center of combustion is adjusted during the load increase. Another important observation is the trend of an earlier center of combustion during the transient phase for knock frequency based control compared to conventional control. At first glance, this might suggest control closer to the target knock frequency, since the conventional controller operates close to the lower limit of the knock boundary during the transient phase. The reason for this operation closer to the lower knock boundary limit within the conventional controller is that the spark timing adjustment during the load increase is governed by the varying base map values that represent spark timings at this lower knock boundary limit (ref. to Equation 6.2). Thus, small spark advance increments are not directly apparent due to the larger variation of the base spark timing. The larger spark retardation after a knock event can be directly identified, for example during the transient phase at 4000 min^{-1} and the load increase from 12 bar to 16 bar, but occurs less frequently.

In order to further evaluate the observed trend of the earlier center of combustion during the transient phase for the new controller, a load decrease instead of a load increase is simulated (ref. to the right side of Figure 6.13). As with the load increase, rapid adaption and similar adaption rates of the center of combustion can be observed. In comparison to the load increase, the center of combustion values during the transient phase are even closer together. However, for the load decrease, the center of combustion values for knock frequency based control tend to later values, inversely to what was observed for the load increase. Closer investigation of the calculated knock frequency during a load increase and load decrease in Figure 6.14 reveals that although the knock frequency is kept relatively constant during the transient phase, the constant value deviates from the targeted 5%.

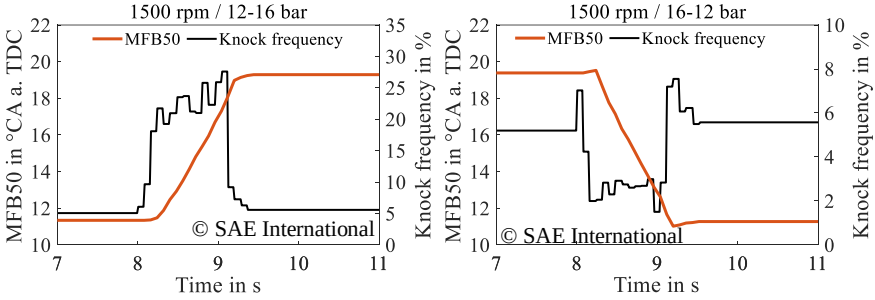

Figure 6.14: Knock frequency prediction during transient load change, according to [77].

One likely reason for this behavior is the already mentioned limitation of the knock frequency estimation for the subsequent cycle. Whereas, AI_{Limit} and σ_{AI} are estimated with respect to the varying load, AI_{mean} is determined for the current load. Thus, a larger variation of AI_{mean} across the load change would result in reduced prediction accuracy of the upcoming knock frequency compared to a load change that contains a smaller AI_{mean} variation. This can be confirmed by the results given in Figure 6.15. The load increase from 12 bar to 16 bar at 1500 min^{-1} includes a variation of the mean auto-ignition onset by 6.3 °CA. The resulting calculated knock frequency during the transient phase is above 20%. The second presented load increase from 16 bar to 20 bar at 2500 min^{-1} includes a smaller AI_{mean} variation of 4.4 °CA. Due to the smaller variation and thus a smaller prediction error, the calculated knock frequency during the transient phase has reduced to values between 10% and 15%.

It is important to note, that as already mentioned in the preceding chapter, the limitation of the AI_{mean} estimation is simulation-specific and not necessarily relevant for an engine application. This is further discussed in the subsequent chapter. In addition, it needs to be mentioned, that this limitation is only relevant for the investigation of transient operation, since the estimated load is almost constant during stationary operation, except for the negligible changes caused by the spark timing adjustments in a confined range of a few degrees of crank angle around the target value. Consequently, also the variation of AI_{mean} is significantly lower.

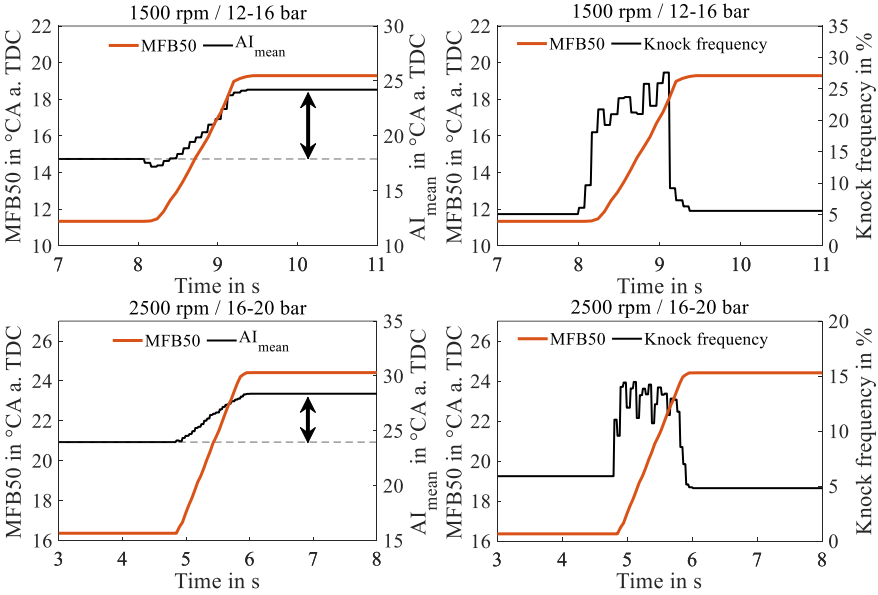

Figure 6.15: Predicted knock frequency for two cases with different variations of AI_{mean} during a transient load change.

For the final assessment of the potential of the new control approach, the stationary results of both controllers are compared to determine the effect on the fuel consumption, the CO_2 emissions and the engine-out temperatures. The results for the covered range of engine speeds and loads are presented in Figure 6.16 and the engine speed and load combinations that have been evaluated are marked. They indicate a reduction potential of the specific fuel consumption and the CO_2 emissions of 0.1-0.9% and 0.2-1.0% respectively. The highest reduction potential was found for the highest investigated engine speed and load. Generally, the CO_2 emission and specific fuel consumption reduction increases with increasing engine speed and load.

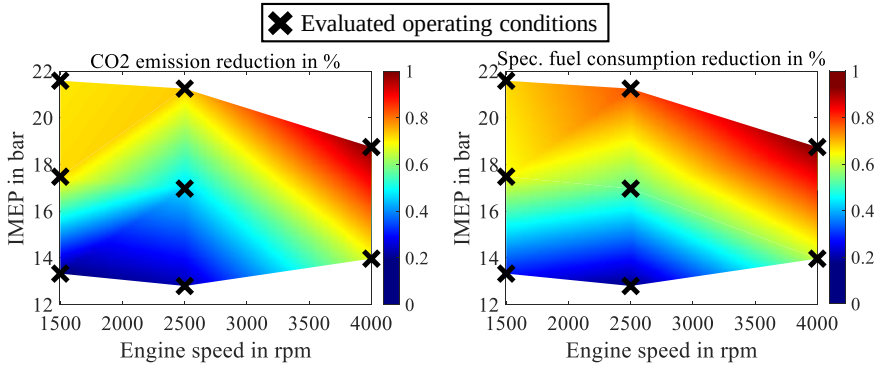

(a) Controllers activated at low initial knock frequency.

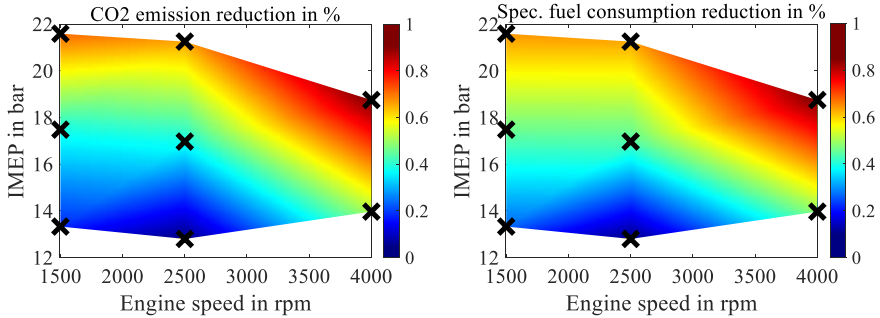

(b) Controllers activated at high initial knock frequency.

Figure 6.16: CO_2 emission and fuel consumption reduction potential with knock frequency based knock control.

Comparison of both parameters for early and late spark timing initialization further reveals similar results, highlighting that the reduced variability and control closer to the desired target center of combustion are the main contributors, whereas the initial controller response has only a small effect. Finally, including all investigated operating points, by applying the knock frequency based control, the average engine out temperature over time could be decreased by approximately 2.3 K, with only a small variation of values between 1.6 K and 2.8 K. Although the decrease is rather marginal, it is a good indicator of increased efficiency and additionally refers to a small reduction of the thermal load of downstream exhaust components such as the exhaust gas turbine.

To sum up, the investigation of the knock frequency based knock controller has revealed a promising reduction of the specific fuel consumption, the CO_2 emissions and the small reduction of the engine-out temperatures. The efficiency gain is achieved mainly by a reduced variation of the center of combustion over time and operation closer to the target value. This is enabled by direct control of the knock frequency instead of a control action based purely on the detection of knock. Further, transient simulations revealed control abilities of the new approach close to those of the conventional controller. The transient operating conditions and their investigation also revealed some limitations of the simulation model and the controller, caused by measurement data on which the controller setup is based. In the following chapter, therefore, the robustness of the controller in general, the limitations identified by the simulative investigations and the requirements concerning an engine application will be discussed.

6.4 Robustness and Requirements for an Engine Application

To provide a suitable basis for further development, in the following, different features of the knock frequency based controller and the simulative investigation are discussed with the focus on engine application of the new controller. This will point out crucial differences that have to be considered for the transition from a simulation model to a controller running on an ECU.

As one crucial requirement, knock relevant parameters during transient operation have to be implemented in the controller, as it is currently solely based on data from stationary operation. Especially the temperature is the most important parameter due to the large influence on the auto-ignition. For an accurate prediction of the auto-ignition onset and thus the knock frequency, not only the inertia of the wall temperatures but also varying intake temperatures would have to be considered. Since the two-stage auto-ignition model used to determine the auto-ignition onset of the mean cycle requires the unburnt temperature as input, knock frequency calculation can be expected to yield good results if these effects are considered within the provided model input. Consequently, further influencing factors such as EGR rate or varying fuel blends could be considered

if the relevant values are available as input to the auto-ignition model and if the dependence of those effects on the cycle-to-cycle variation and thus σ_{AI} and the AI_{Limit} can be correctly modeled.

Further, as previously described, the predictive ability of the model can be improved by consideration of transient conditions not only for the determination of AI_{Limit} and σ_{AI}, but also the estimation of AI_{mean} of the subsequent engine cycle. Within the simulation, the determination of AI_{mean} is limited to the current engine cycle. For an engine application, the determination of AI_{mean} is even more challenging, since the average engine cycle is required, which cannot directly be measured during engine operation. Measurement of the cylinder pressure would require averaging over several cycles to yield a representative mean pressure trace. This is not suitable because it prevents cycle-resolved spark timing adjustment and thus reduces the potential efficiency gain. For that reason, the relevant mean engine cycle has to be provided differently to enable the determination of AI_{mean}.

One simple approach to provide the required pressure could be to reverse the net heat release rate approximation approach based on the cylinder pressure, derived from the first law of thermodynamics. A comprehensive derivation of the formula can be found in [2]. With this approach, the pressure could be approximated based on the heat release. Therefore, the required heat release rates would be modeled operating point specifically by a Vibe approximation [80], with Vibe parameters depending on engine speed, IMEP and spark timing similar to the modeling of AI_{Limit} and σ_{AI}. The additionally required unburnt temperature then could be determined from a polytropic process based on the pressure. It shall be noted, that this is only one possible option for implementation.

There are further conceivable approaches, such as the determination of the pressure and the unburnt temperature traces based on a neural network. This could have multiple advantages. A neural network could be suitable to consider further parameters such as the intake temperature for the prediction of the relevant auto-ignition model input. Additionally, offline training, covering different operating conditions could prove to be helpful to enable high calculation performance while covering many different influencing parameters, especially for the most performance-critical parameter AI_{mean}. This would consequently enhance the real-time capability for a comprehensive range of engine speeds.

These deliberations highlight the difference of the AI_{mean} determination between the simulation and an engine application and show that a successful AI_{mean} estimation is coupled with a suitable prediction of the mean engine cycle.

Another significant finding is the relevance of the load estimation accuracy on the achievable control accuracy during transient operation. This was identified from simulations of similar operating conditions but different durations for the load increase, see Figure 6.17.

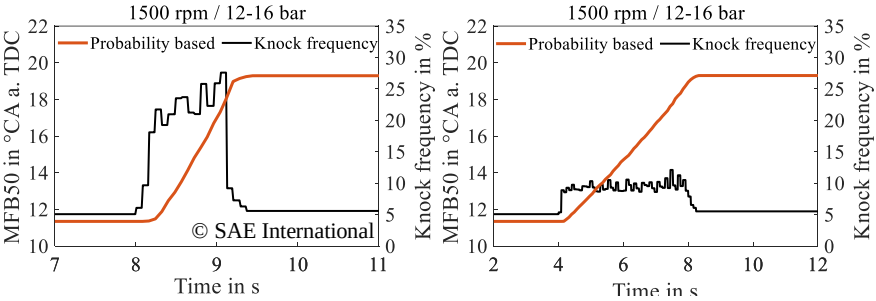

Figure 6.17: Comparison of 1 s [77] and 4 s transient load increase indicating the influence of transient duration on knock frequency prediction capability.

For a longer duration of the load step of 4 s instead of 1 s, the constant deviation of the calculated knock frequency drops from over 20% to a mean value below 10%. The reason for the smaller deviation can be explained by the sensitivity of the knock frequency calculation to the load estimation and exponential increase of the knock frequency over the spark timing, indicated in Figure 6.18.

The curves represent the resulting calculated knock frequency over the spark timing for increasing loads starting at 12 bar. If a similar load increase is performed with different durations, the load increase from one cycle to the next one is larger for the overall load variation in less time. As previously described, the controller predicts the knock frequency for the upcoming cycle under the assumption of an unchanged spark timing. Consequently, the predicted knock frequency for an upcoming cycle during the load change results in a higher value if the transient load increase is performed in less time. This characteristic is visualized in Figure 6.18 by the two markers at similar spark timing but different loads.

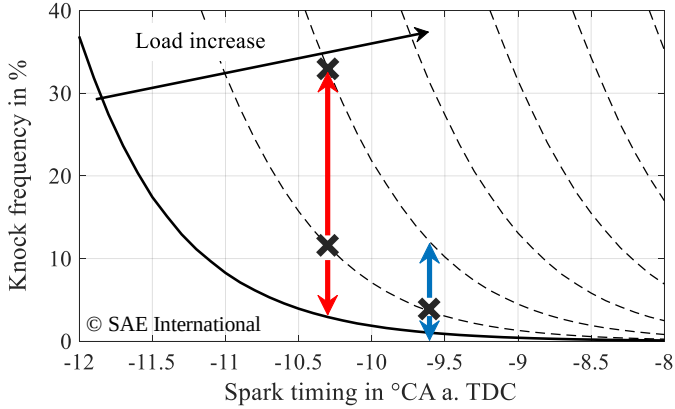

Figure 6.18: Influence of an engine load estimation inaccuracy on the knock frequency prediction, according to [77].

Furthermore, the red and blue arrows show the prediction error for a similar load estimation inaccuracy at different absolute knock frequency values. As can be seen, larger knock frequencies yield larger knock frequency prediction errors and thus larger errors regarding the spark timing adjustment. That means transient conditions, during which the knock frequency increases, contain a larger prediction error compared to transient phases during which the knock frequency decreases. This differentiated influence also explains the smaller deviation of center of combustion values of the new controller to those of the conventional controller during a load decrease compared to a load increase. The red and blue arrows additionally indicate that an overestimation of the engine load compared to an underestimation always results in a larger prediction error, regardless of the absolute value of the knock frequency.

Finally, it shall to be noted that the described effects are limited to transient conditions, as the knock frequency is generally low and the engine load remains almost constant during stationary operation. To summarize, for an engine application, the expected duration of transient loadsteps and the available load estimation accuracy is decisive for the achievable control accuracy within transient conditions.

Regarding conventional knock control, the included adaptive map allows for an adaptation of the controller to consider varying fuel quality but also aging effects of the engine without the necessity of additional tuning or calibration. Although the new control concept can completely relinquish the measurement of knock occurrence, it would be sensible to implement the knock sensor signal to enable similar abilities. A possible integration into the controller is discussed in the following chapter.

Not only the implementation of adaptive capabilities but also the consideration of a multi-cylinder setup is crucial on the way to a serial engine application. Within this project, the measurement data and simulations are constraint to a single-cylinder engine. For a multi-cylinder setup, similarly as for a conventional knock controller, the system could be set up for the entire engine with focus on the most critical cylinder or cylinder-individual. As already stressed, the computational requirements and hardware capabilities play an important role for a successful implementation, which would be even enhanced by a cylinder-individual setup. Thus, not only the possible requirement of multiple knock sensors, depending on the implementation of adaptive capabilities, but also the computational capabilities of the ECU and potential cost increase have to be considered. Moreover, as not covered in this project, a possible cylinder-to-cylinder influence regarding the knock frequency prediction based on the Three-Parameter-Approach should be investigated first, to confirm the suitability of the underlying prediction method or provide the required basis to enable cylinder-individual knock frequency prediction with respect to a multi-cylinder engine design. Then, cylinder-individual application of the new knock control is feasible.

Finally, as previously mentioned, tuning of the gains and the tolerance value should include as many operating points as possible to achieve the best possible results while accounting for the varying shapes of the exponential increase of the knock frequency and preventing instability. While maximizing both gains is the goal during tuning to achieve the best possible results, emphasis should be put on K_{ret} to retard the spark timing. Fast retardation is crucial to prevent any engine damage. As was shown, even a too far initial retardation can be compensated by a very fast spark advance in the subsequent cycles if the controller is tuned appropriately.

6.5 Concept for Knock Sensor Integration

As mentioned above, integration of the knock sensor data within an engine application is useful to allow closed-loop control with online calibration and accounting for further effects such as engine aging, varying fuel blends, and fuel qualities. For the presented simulative investigation of the general control capabilities and the maximum potential of the controller, however, the knock sensor data integration is not useful for three main reasons. Firstly, the new knock frequency based controller is calibrated to precisely match the measured knocking behavior of the investigated engine to allow evaluation of the controller's potential. Secondly, investigating one fuel as a starting point, no fuel variations or aging effects must be considered. Lastly, as discussed for the simulation model of the conventional controller, within a 0D simulation environment, knock sensor data is not directly available. Thus, any modeling approach could potentially contain inaccuracies to the actual sensor data.

In Figure 6.19, a possible knock sensor integration in the control system is presented to provide a suitable basis for this task in the context of an ECU integration. The proposed concept compares the predicted knock frequency within the knock frequency based controller with the measured knock frequency over a specific number of engine cycles to provide a measure for the deviation between the predicted and the actual knock frequency. Therefore, a moving average filter is applied to determine the average predicted knock frequency over the defined number of engine cycles i. The knock sensor signal provides the number of knock events during these engine cycles, which are subsequently summed up and divided by the number of cycles to yield the actual knock frequency. The difference between the actual and predicted knock frequency over a specific number of engine cycles provides a measure for the prediction error and is used as input for a PI or, if required, PID controller. Finally, the resulting control variable is applied to AI_{Limit}, to calibrate the knock frequency prediction accordingly.

Depending on the implementation, different control variables are conceivable. If the control variable were added to AI_{Limit}, values below zero would shift AI_{Limit} to earlier auto-ignition onsets, resulting in lower predicted knock frequencies. Vice versa, positive control variable values would shift the AI_{Limit} to later timings, resulting in higher knock frequencies. In case of multiplication

instead of summation (as depicted in Figure 6.19), the control variable would represent a correction factor and values below one would yield lower knock frequencies and values above one higher knock frequencies.

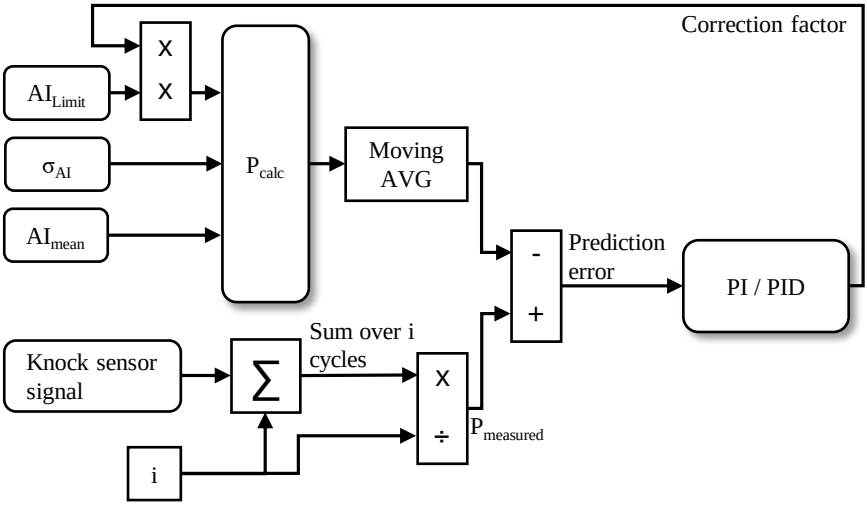

Figure 6.19: Knock sensor integration concept.

Regarding tuning, the number of cycles for averaging plays an important role. A smaller number results in faster adjustment of the correction under varying boundary conditions due to faster change of the average values and the prediction error. However, due to the stochastic nature of the phenomenon, a minimum number of cycles is required to determine the actual knock frequency with sufficient accuracy. Therefore, tuning the feedback loop is a trade-off between transient capabilities and accuracy of the calculated prediction error.

It shall be noted that the proposed concept is only one conceivable method for the knock sensor integration and other methods or variations of the proposed concept might be suitable. For example, one further possibility could be to compare the likelihood ratio determined for a specific number of engine cycles for the predicted and measured knock frequency instead of the average knock frequencies directly. Since the likelihood ratio is also dependent on the number of engine cycles, it might be suitable to improve the trade-off compromise

required for direct comparison of the averaged knock frequencies. Yet, actual ECU integration and testing are required to evaluate a knock sensor integration concept and its performance compared to other possible integration methods comprehensively.

7 Conclusions and Outlook

Various investigations have been performed to improve understanding of the knock phenomenon and the role of cycle-to-cycle variations. The influence of temperature and mixture inhomogeneities on the occurrence of knock was evaluated by globally evaluating regions with the highest temperatures and lowest air-fuel equivalence ratios and locally investigating the temperature and charge velocity of a connected volume around the spark plug gap. For the isolation of the knock-relevant unburnt mixture and the occurrence of low-temperature ignition were identified as the main challenges to allow a suitable inhomogeneity evaluation. They were solved by the introduction of a new separation criterion for the unburnt zone based on chemical species concentrations and a specific distance and restriction of the inhomogeneity evaluation to a time step before the first ignition stage respectively. From all investigations, no direct correlation between inhomogeneities and the occurrence of knock could be observed and cyclic fluctuations of the inhomogeneity has shown to be at small negligible level.

To analyze the role of auto-igniting connected volumes in more detail, following a correlation observed in the literature between the variance of ε and the knock tendency, the reactivity parameter ε of the detonation diagram was applied to a 0D simulation environment. The aim was to investigate if the detonation diagram can be used to evaluate auto-ignitions to successfully identify knock-relevant conditions. Calculation of ε for single working cycles at the time of auto-ignition has proven to be sensitive to the contained hotspot radius. It was shown that a, in the literature used, constant value of 10 mm is not a realistic assumption and not suitable for the determination of ε. Instead, modeling a hotspot size distribution based on various assumptions and several literature values for observed hotspot sizes, yielded more realistic values of ε.

In order to analyze the observed correlation to the knock tendency, a calculation approach from the literature was applied to determine the knock frequency

of an operating point based on the prevailing distribution of ε at the time of auto-ignition. The results revealed that a general tendency of the knock frequency can be predicted, but the overall prediction accuracy is significantly lower compared to the original approach from which the calculation method was adapted. The low accuracy was attributed to a lack of validation possibilities for the implemented hotspot size distribution modeling and is further also suspected to yield from limited applicability of the detonation diagram to a 0D environment. Since the detonation limits represent a range of conditions for transition between two regimes, the detonation diagram is generally expected to be better suited for the evaluation of operating conditions that develop extreme pressure oscillations and show a large variation of the detonation parameters in the course of the auto-ignition. Precise differentiation of operating conditions and their knock-relevance close to the knock boundary, however, has proven to be very challenging, as these conditions are confined to a much smaller range within the detonation diagram.

Further, a method was introduced that allows automated and efficient identification of auto-igniting volumes that are separated from the spark ignited flame front in 3D CFD simulations. Application of this method to results of a large-eddy simulation that includes 100 engine cycles enabled the determination of a hotspot radius distribution. The results indicated that the modeling approach using halved normal distributions are a good first approximation, but better results regarding the knock frequency prediction can be reached by modeling the distributions with a streched beta distribution. Although the knock frequency prediction accuracy could be significantly increased compared to the approach using halved normal distributions, even after identification of a realistic distribution of hotspot sizes at a single operating point and a refined modeling approach, the accuracy remained lower compared to the accuracy demonstrated in the literature for the original knock frequency calculation method. It also showed that the hotspot size determination based on the identified hotspot cells, significantly affects the resulting values. This contributes to the challenge of realistically modeling a hotspot size distribution.

Nevertheless, the method provides an excellent tool to identify local parameters during auto-ignition that can be used to gain further understanding of the knocking phenomenon and consequently improve the engine development process. Besides the hotspot radius or general size of hotspots, the method can be used to investigate further properties such as their location and distribution

of locations in the combustion chamber and in relation to the flame front, the cylinder walls and valves. Additionally, depending on the respective numerical grid and traceability of charge motion over time, it is conceivable to investigate physical or chemical properties such as pressure, temperature, air-fuel equivalence ratio or the ignition delay time over the duration of the combustion at the location where the hotspot auto-ignites. Results of these investigations could yield fundamental information regarding the occurrence of knock and the associated knock intensity.

For further evaluation of the influence of cycle-to-cycle variations on knocking, the calculation approach to determine the knock frequency based on auto-ignition onset distributions, has been applied to simulations. Therefore, single working cycles, correctly reproducing the cycle-to-cycle variations, had to be simulated. This was realized by two different simulation approaches. The results revealed that, based on a simulative prediction of the cycle-to-cycle variations and determination of the auto-ignition onset of the simulated single working cycles, an actual prediction of the knock frequency with high accuracy is possible. The two simulation approaches additionally revealed a significant difference in required computational effort, due to the different number of cycles that have to be simulated and due to different degrees of implementation in the utilized simulation tool.

Following the successful knock frequency prediction, a new concept for knock control was introduced, that is characterized by direct control of the knock frequency. This direct control, rather than a reactive control based on the detection of knock is enabled by a predictive calculation of the knock frequency. For further development towards an engine application, an important factor is to ensure sufficient performance for the determination of the knock frequency and therefore also the three underlying parameters. For the simulative investigation, performance was increased by providing two of the three parameters via engine maps instead of a phenomenological determination and modifying the definition of the third parameter slightly. These measures allowed a cycle-synchronous knock frequency prediction without simulations of multiple single working cycle for one knock controlled engine cycle.

Two simulation models were created for conventional and knock frequency based knock control to compare them under various stationary and transient conditions to identify the potential of the new control approach. During

stationary operation, as expected, the new controller is characterized by a significantly reduced variation of the center of combustion over time, with precise adjustment very close to the desired target center of combustion. During transient conditions, the new controller is characterized by a fast adjustment of the center of combustion, with a comparable response to the conventional controller. An observed deviation of the predicted knock frequency to the target value during transient conditions could be explained by the simulation-specific restriction of one underlying parameter of the knock frequency prediction to the current engine cycle as well as the varying sensitivity of the knock frequency prediction to a load estimation inaccuracy at different absolute knock frequencies. Thus, the results provide crucial information about the model sensitivity and where special emphasis has to be put on regarding an engine application.

Overall, the simulative investigation confirmed the initial idea of an efficiency gain due to a reduced variation of the spark timing and operation closer to the target center of combustion. Both, specific fuel consumption and CO_2 emissions could be reduced by a maximum of about 1%, with the highest reduction potential identified at highest investigated engine loads and engine speeds. Thus, engine efficiency was increased, essentially without an increase of the prevailing knock tendency. The final discussion of the simulation-specific setup of the controller and additional requirements concerning an ECU application provides a comprehensive basis for further development and application to an engine.

Therefore, to sum up, the project results provide important new insights into the knocking phenomenon in general and include a new knock control concept and the first simulative investigation. Especially, considering the ongoing necessity to reduce emissions, with increasingly strict regulations and further development of synthetic fuels, knocking remains a topic of interest. The gained knowledge contributes to the efforts to conform to the new regulations and to limit CO_2 emissions, as it provides vital information for the development of new generation combustion engines but also provides a promising knock control approach that might be retrofitted to existing engines.

A Appendix

A.1 Temperature inhomogeneity

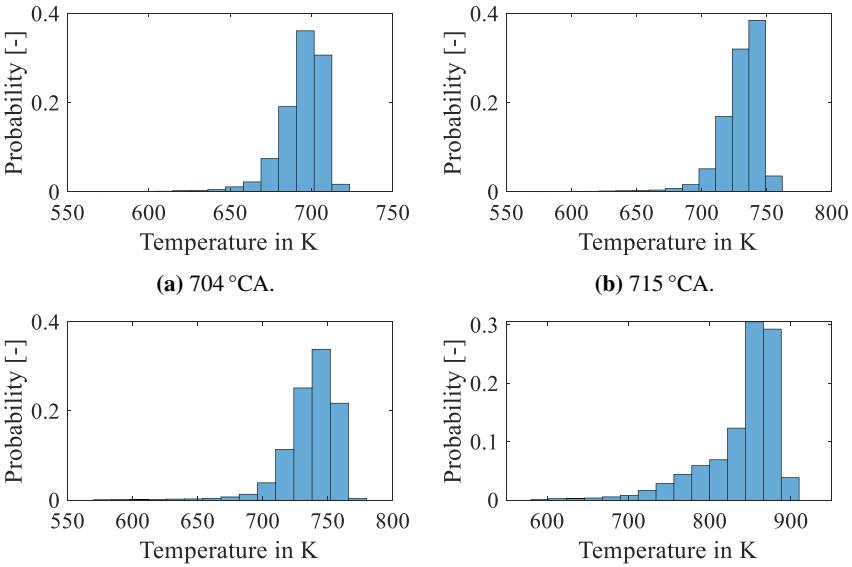

(a) 704 °CA. **(b)** 715 °CA.

(c) 725 °CA. **(d)** 735 °CA.

Figure A.1.1: Absolute temperature distribution at the time steps displayed in Figure 3.7.

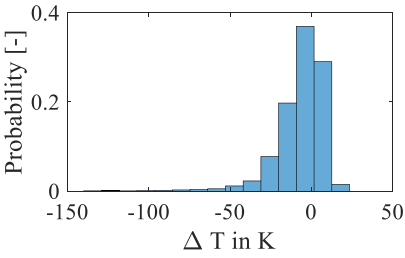

(a) 704 °CA.

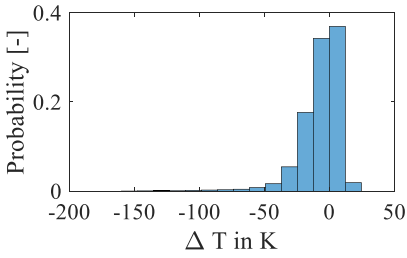

(b) 710 °CA.

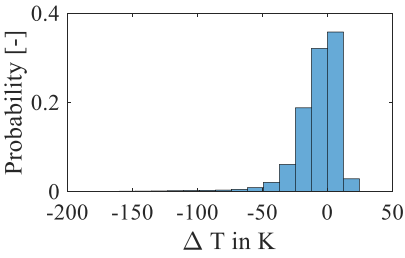

(c) 715 °CA.

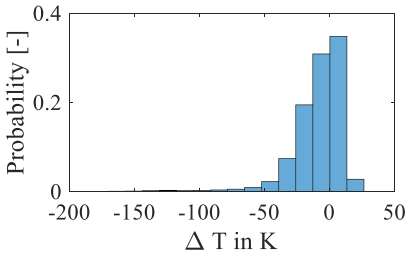

(d) 720 °CA.

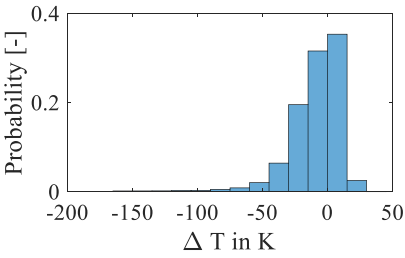

(e) 725 °CA.

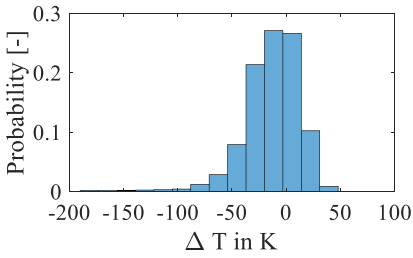

(f) 730 °CA.

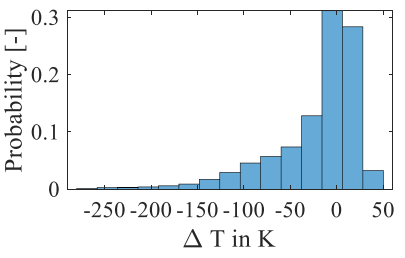

(g) 735 °CA.

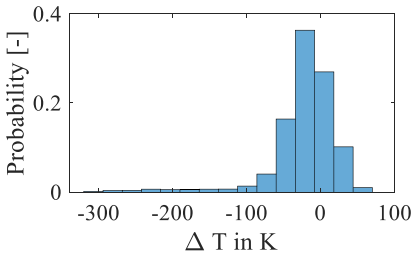

(h) 740 °CA.

Figure A.1.2: Relative temperature distribution at the time steps displayed in Figure 3.8.

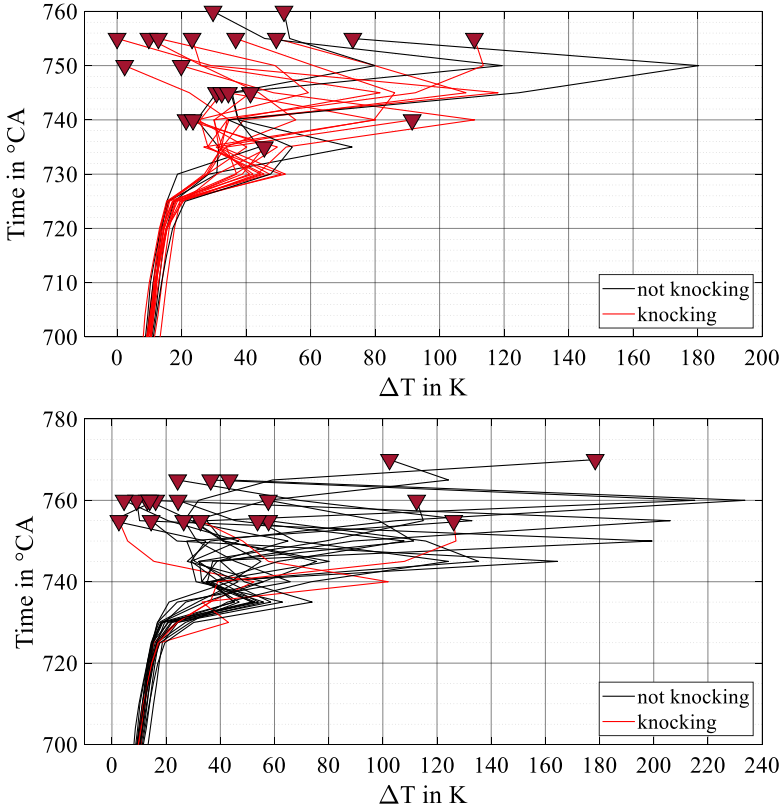

Figure A.1.3: Temperature inhomogeneity for 5% mass definition over the entire duration, for OP 1 (top) and OP 2 (bottom).

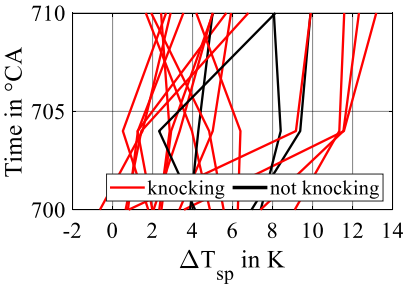

(a) OP 1, radius = 2 mm.

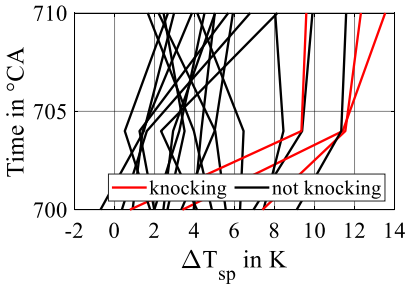

(b) OP 1, radius = 5 mm.

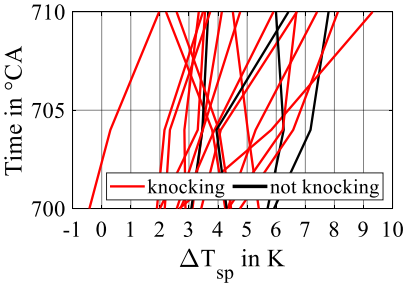

(c) OP 1, radius = 15 mm.

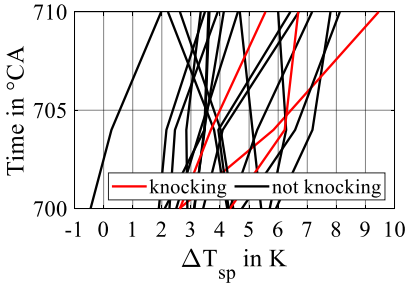

(d) OP 2, radius = 2 mm.

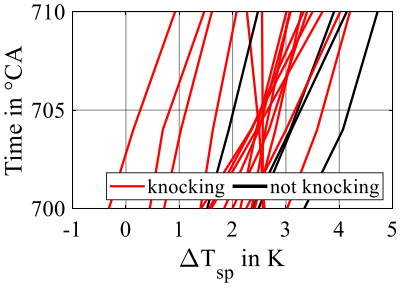

(e) OP 2, radius = 5 mm.

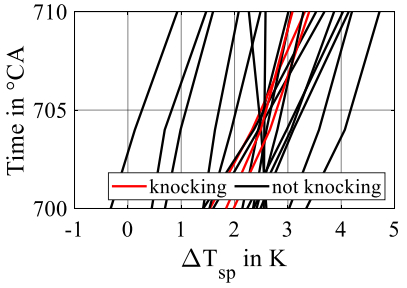

(f) OP 2, radius = 15 mm.

Figure A.1.4: Temperature inhomogeneity for spherical volume around the spark plug gap, varying radii.

A.2 Excitation time

Table A.2.1: Excitation time lookup table – reduced form with limited pressure and temperature resolution and constant λ = 1, EGR = 4%.

Pressure in bar	Temperature in K	Excitation time in s
20	600	4.010E-06
20	700	2.152E-06
20	800	1.863E-06
20	900	1.825E-06
20	1000	1.541E-06
20	1100	1.333E-06
20	1200	1.141E-06
20	1300	9.604E-07
20	1400	8.423E-07
20	1500	7.555E-07
40	600	3.260E-06
40	700	1.574E-06
40	800	1.432E-06
40	900	1.273E-06
40	1000	1.128E-06
40	1100	9.422E-07
40	1200	7.800E-07
40	1300	6.644E-07
40	1400	5.605E-07
40	1500	4.761E-07
60	600	1.441E-05
60	700	1.355E-06
60	800	1.207E-06
60	900	1.090E-06
60	1000	9.412E-07
60	1100	7.848E-07
60	1200	6.530E-07
60	1300	5.373E-07
60	1400	4.505E-07
60	1500	3.791E-07

80	600	1.121E-05
80	700	1.233E-06
80	800	1.138E-06
80	900	1.006E-06
80	1000	8.595E-07
80	1100	7.097E-07
80	1200	5.874E-07
80	1300	4.765E-07
80	1400	3.949E-07
80	1500	3.271E-07
100	600	9.570E-06
100	700	1.154E-06
100	800	1.043E-06
100	900	9.301E-07
100	1000	7.976E-07
100	1100	6.657E-07
100	1200	5.364E-07
100	1300	4.370E-07
100	1400	3.515E-07
100	1500	2.907E-07

A.3 Epsilon – constant radius

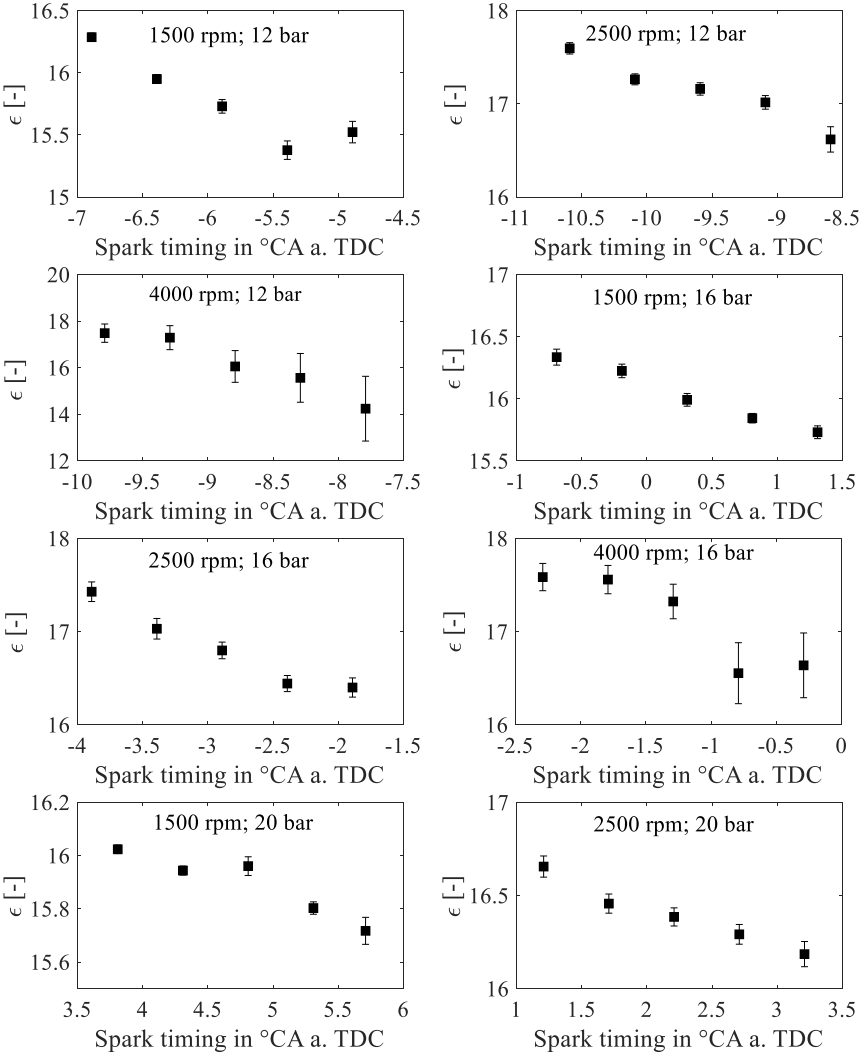

Figure A.3.1: Mean and variance of ε for ε_{geom} = 10.76 and hotspot radius assumed with 10 mm constant.

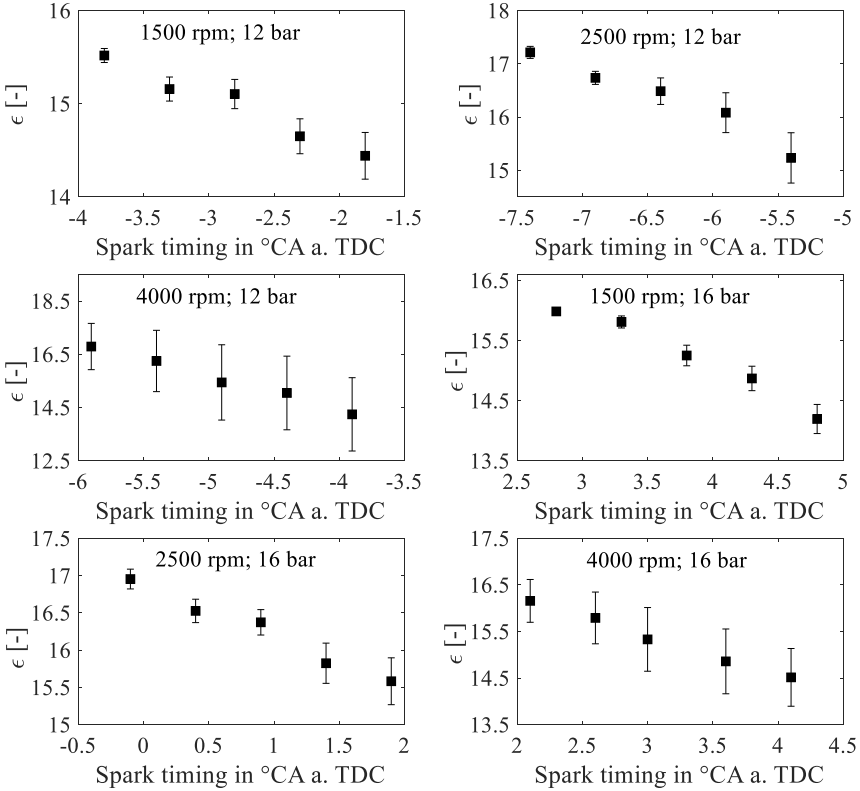

Figure A.3.2: Mean and variance of ε for ε_{geom} = 11.8 and hotspot radius assumed with 10 mm constant.

A.4 Epsilon – modeled radius

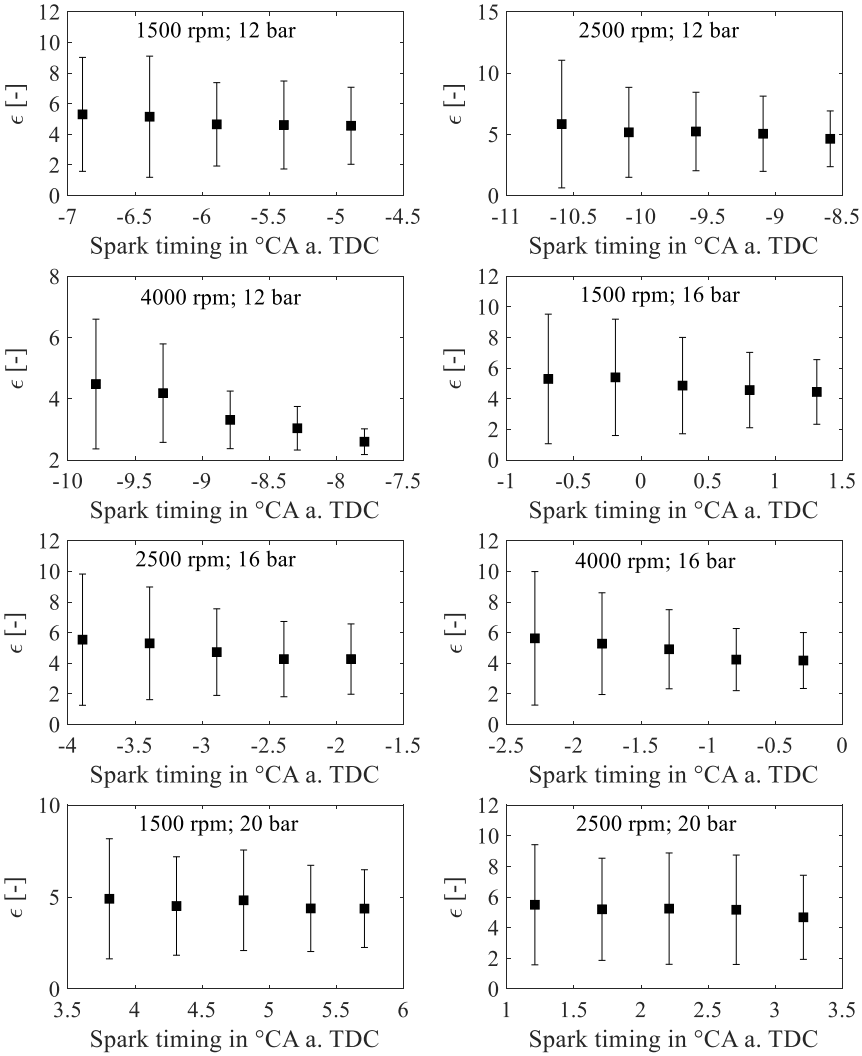

Figure A.4.1: Mean and variance of ε for $\varepsilon_{geom} = 10.76$ and modeled hotspot radius.

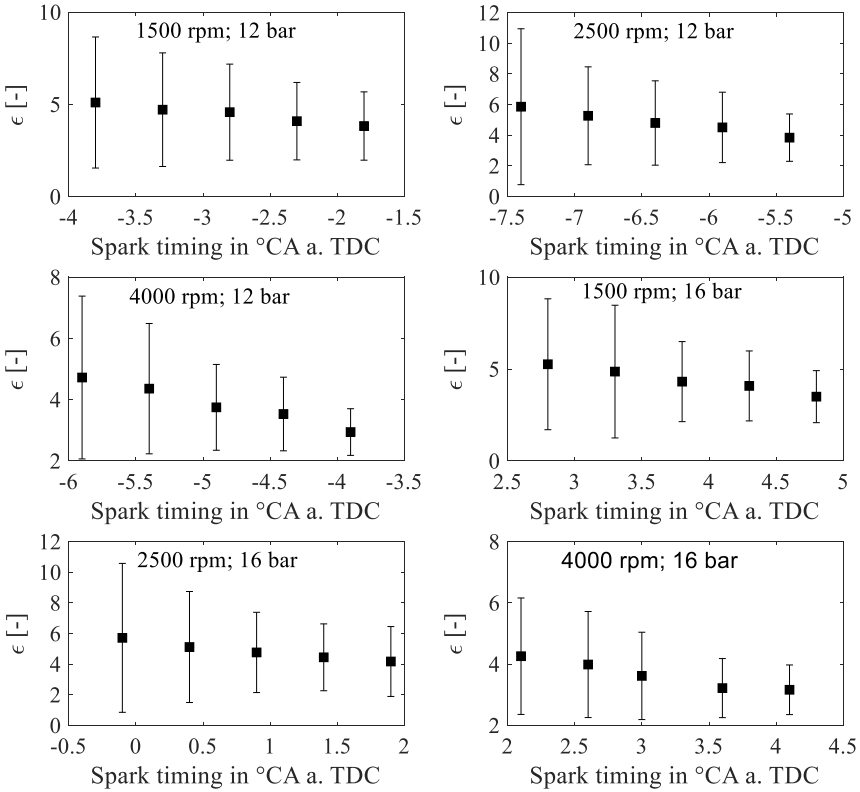

Figure A.4.2: Mean and variance of ε for ε_{geom} = 11.8 and modeled hotspot radius.

A.5 Simulative controller comparison

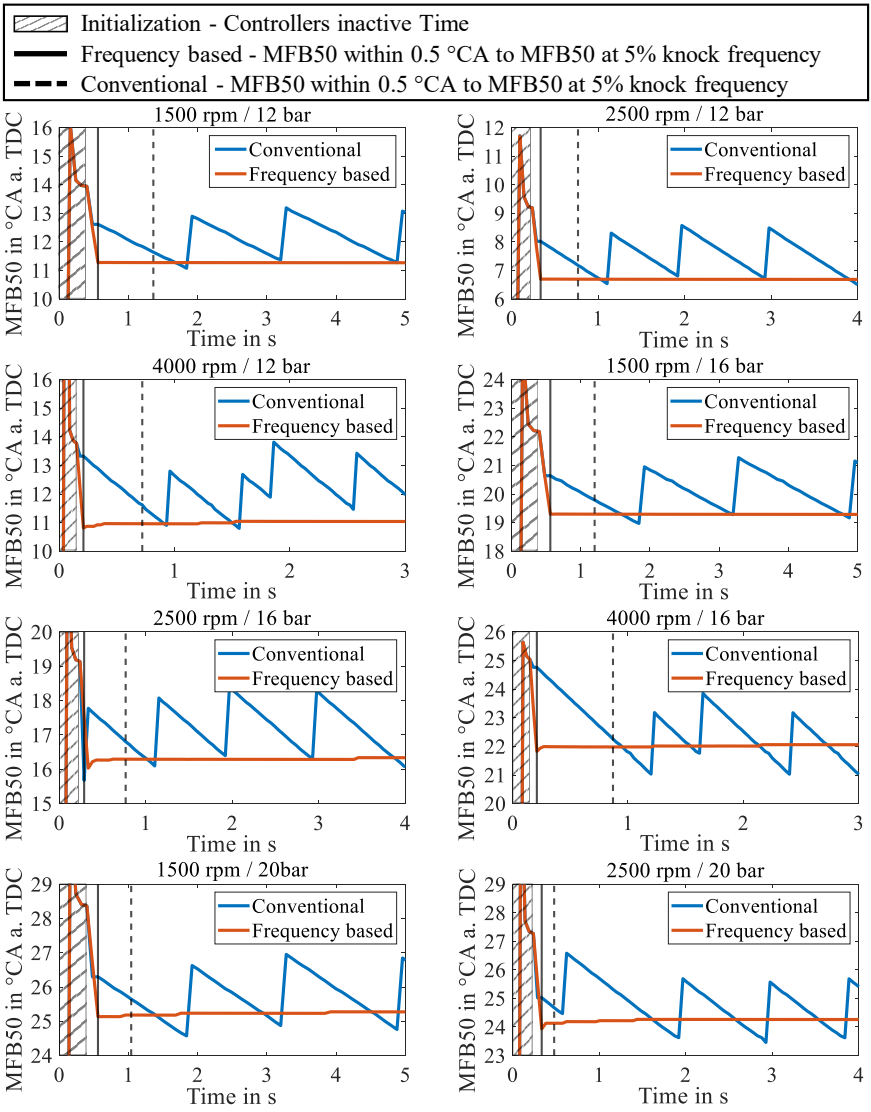

Figure A.5.1: Initial controller response for activation at low knock frequency.

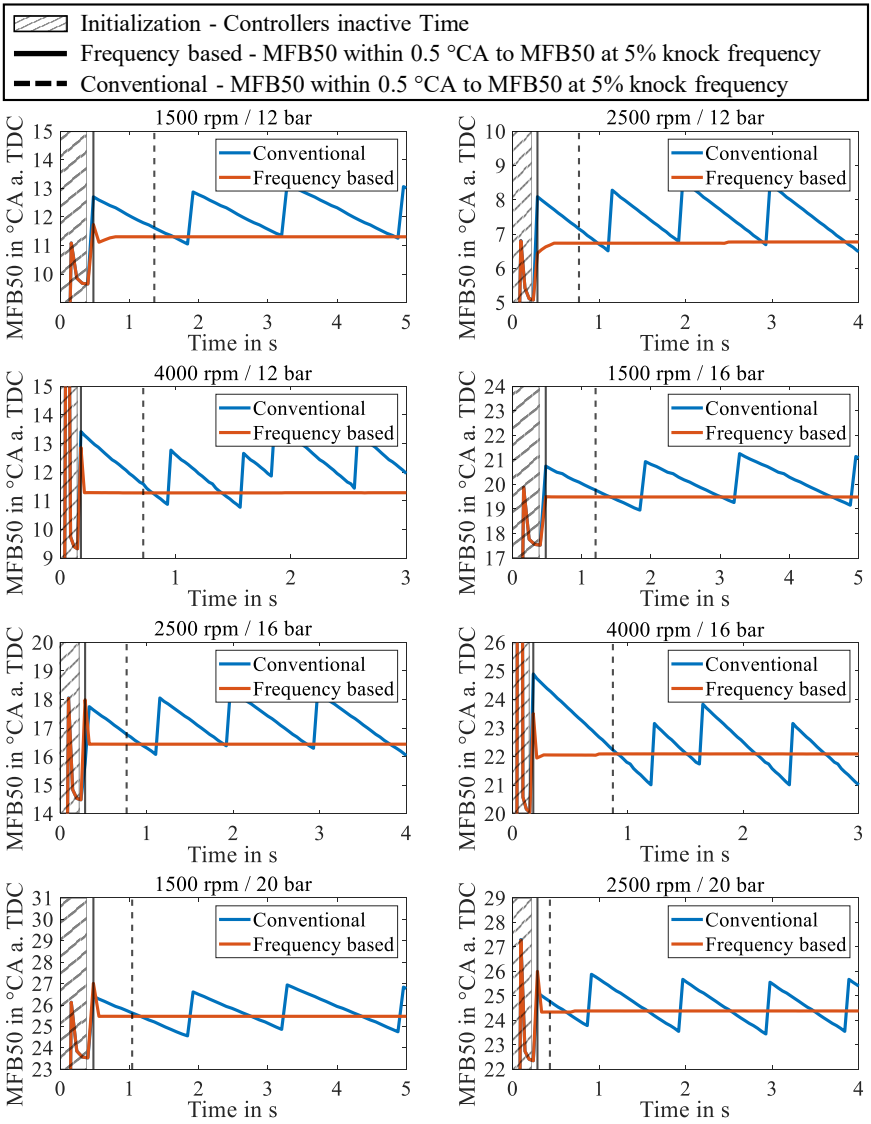

Figure A.5.2: Initial controller response for activation at high knock frequency.

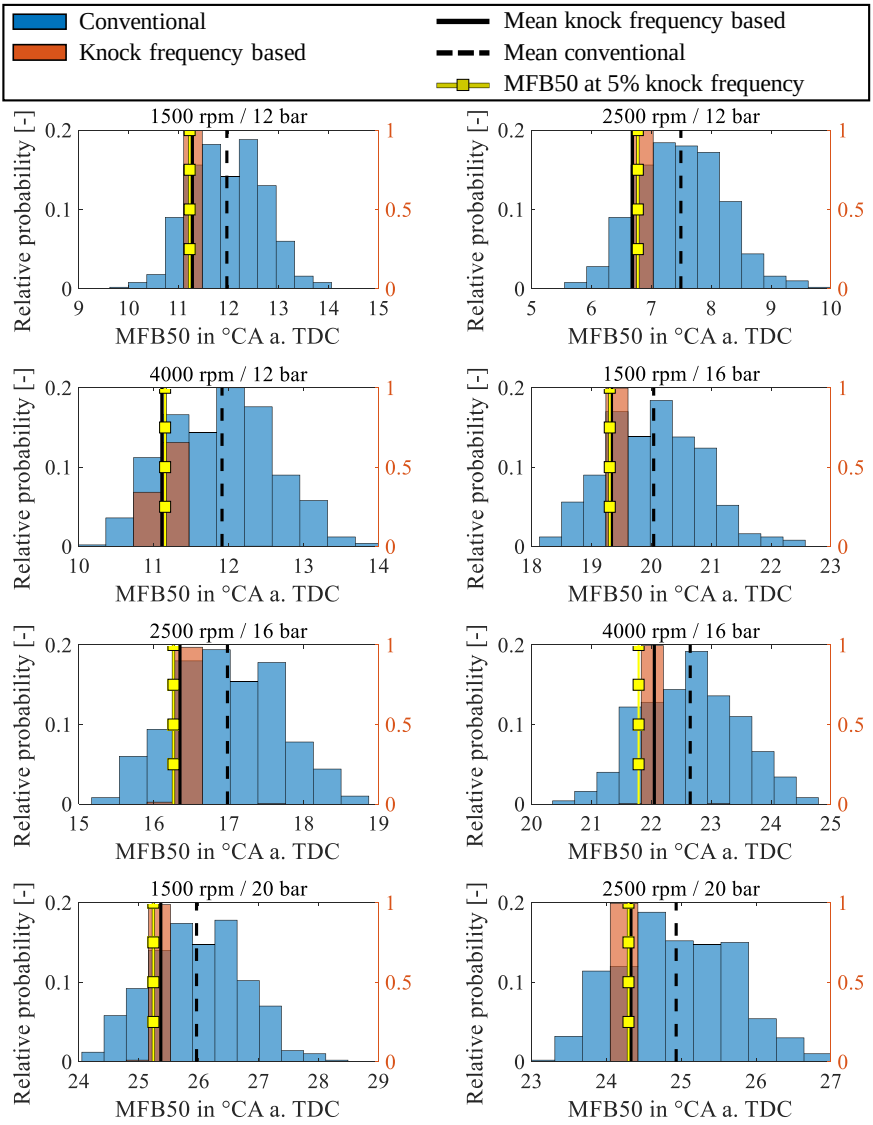

Figure A.5.3: Comparison for MFB50 distribution for activation at low knock frequency.

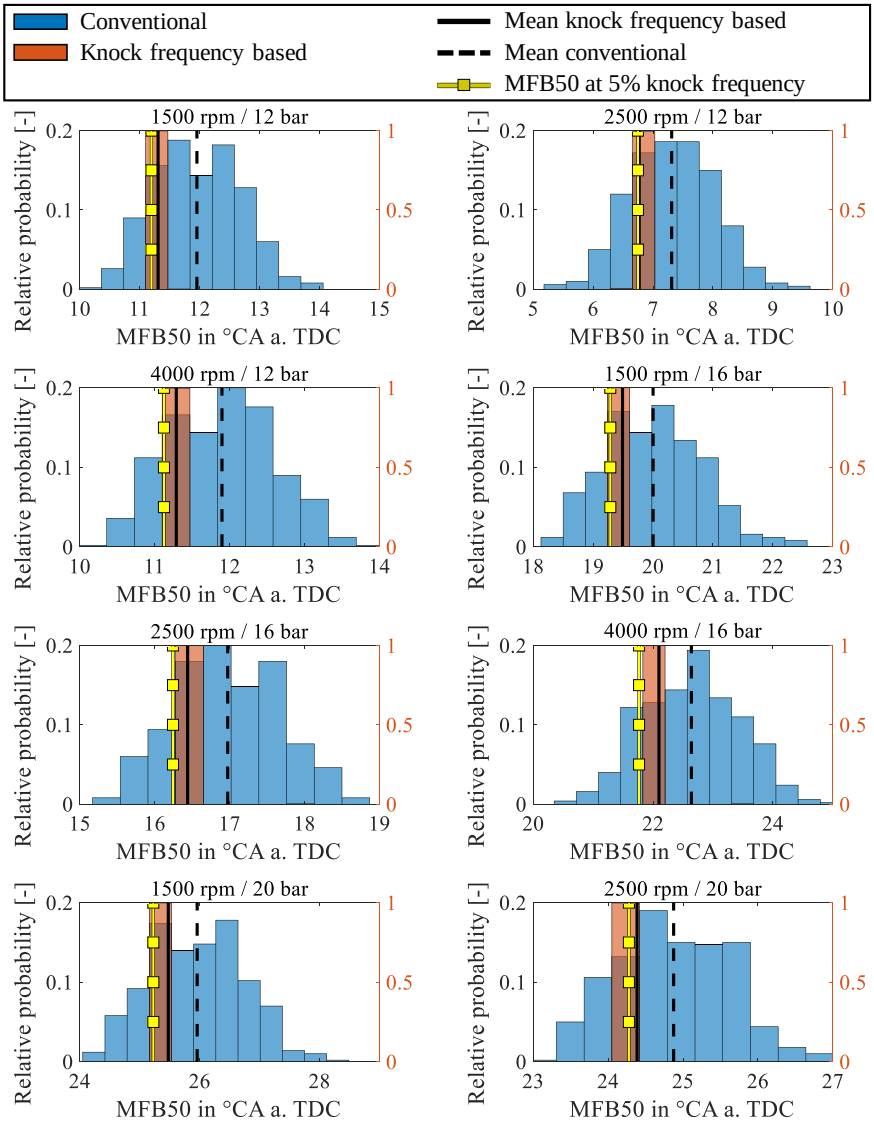

Figure A.5.4: Comparison for MFB50 distribution for activation at high knock frequency.

Bibliography

[1] M. Blomberg, N. Fajt and L. Leyens. *Fast Knocking Prediction for Gasoline Engines*. Final Report on FVV Project 1370. Research Association for Combustion Engines (FVV) e.V. 2022.

[2] J. B. Heywood. *Internal combustion engine fundamentals*. USA: McGraw-Hill, Inc., 1988. ISBN: 978-0070286375.

[3] S. Curry. "A Three-Dimensional Study of Flame Propagation in a Spark Ignition Engine". *SAE Technical Paper Series 630487*. Jan. 1963. DOI: 10.4271/630487.

[4] R. Maly and G. Ziegler. "Thermal Combustion Modeling — Theoretical and Experimental Investigation of the Knocking Process". *SAE Technical Paper Series 820759*. Feb. 1982. DOI: 10.4271/820759.

[5] U. Spicher. "Klopfen — das (un)bekannte Phänomen". *3. Tagung Ottomotorisches Klopfen*. Berlin. 2006.

[6] J. Warnatz, U. Mass and R. W. Dibble. *Combustion: Physical and Chemical Fundamentals, Modeling and Simulation, Experiments, Pollutant Formation*. Springer Berlin Heidelberg New York, 2006. ISBN: 978-3-540-25992-3.

[7] R. Worret and U. Spicher. *Entwicklung eines Kriteriums zur Vorausberechnung der Klopfgrenze*. Final Report on FVV Project 700. Research Association for Combustion Engines (FVV) e.V. 2002.

[8] C. S. Draper. "Pressure Waves Accompanying Detonation in the Internal Combustion Engine". *Jounal of the Aeronautical Sciences*. Vol. 5. 6. Apr. 1938. DOI: 10.2514/8.590.

[9] L. Nielsen U. Kiencke. *Automotive Control Systems: For Engine, Driveline, and Vehicle*. Springer-Verlag GmbH, Apr. 2005. ISBN: 3-540-23139-0.

[10] K. Reif. *Ottomotor-Management im Überblick*. Springer-Verlag GmbH, July 2015. 258 pp. ISBN: 978-3-658-09524-6.

[11] X. Zhen et al. "The engine knock analysis – An overview". *Applied Energy*. Vol. 92. Apr. 2012, pp. 628–636. DOI: 10.1016/j.apenergy.2011.11.079.

[12] I. Z. Syed, A. M. and J. Naber. "Numerical Simulation of Autoignition of Gasoline-Ethanol/Air Mixtures under Different Conditions of Pressure, Temperature, Dilution, and Equivalence Ratio". *SAE Technical Paper Series 2011-01-0341*. Apr. 2011. DOI: 10.4271/2011-01-0341.

[13] H. Machrafi, S. Cavadias and P. Guibert. "An experimental and numerical investigation on the influence of external gas recirculation on the HCCI autoignition process in an engine: Thermal, diluting, and chemical effects". *Combustion and Flame*. Vol. 155. 3. Nov. 2008, pp. 476–489. DOI: 10.1016/j.combustflame.2008.05.001.

[14] A. Fandakov. "A Phenomenological Knock Model for the Development of Future Engine Concepts". PhD thesis. University of Stuttgart, 2018.

[15] M. Blomberg, M. Hess, R. Hesse and P. Morsch. *Engine Knock Model*. Final Report on FVV Project 1313. Research Association for Combustion Engines (FVV) e.V. 2021.

[16] M. Hess, M. Grill, M. Bargende and A. Kulzer. "Knock Model Covering Thermodynamic and Chemical Influences on the Two-Stage Auto-Ignition of Gasoline Fuels". *SAE Technical Paper Series 2021-01-0381*. Apr. 2021. DOI: 10.4271/2021-01-0381.

[17] L. Bates, D. Bradley, G. Paczko and N. Peters. "Engine hot spots: Modes of auto-ignition and reaction propagation". *Combustion and Flame*. Vol. 166. Apr. 2016, pp. 80–85. DOI: 10.1016/j.combustflame.2016.01.002.

[18] X.J. Gu, D.R. Emerson and D. Bradley. "Modes of reaction front propagation from hot spots". *Combustion and Flame*. Vol. 133. 1-2. Apr. 2003, pp. 63–74. DOI: 10.1016/s0010-2180(02)00541-2.

[19] W. Kleinschmidt. "Selbstzündung im Klopfgrenzbereich von Serienmotoren". *Klopfregelung für Ottomotoren II*. 2006. ISBN: 978-3816926740.

[20] G. Konig and C. G. W. Sheppard. "End Gas Autoignition and Knock in a Spark Ignition Engine". *SAE Technical Paper Series 902135*. Oct. 1990. DOI: 10.4271/902135.

[21] G. König, R. R. Maly, D. Bradley, A. K. C. Lau and C. G. W. Sheppard. "Role of Exothermic Centres on Knock Initiation and Knock Damage". *SAE Technical Paper Series 902136*. Oct. 1990. DOI: 10.4271/902136.

[22] A. Fandakov, M. Grill, M. Bargende and A. C. Kulzer. "A Two-Stage Knock Model for the Development of Future SI Engine Concepts". *SAE Technical Paper Series 2018-01-0855*. Apr. 2018. DOI: 10.4271/2018-01-0855.

[23] M. Hess, M. Grill, M. Bargende and A. Kulzer. "New Criteria for 0D/1D Knock Models to Predict the Knock Boundary for Different Gasoline Fuels". *SAE Technical Paper Series 021-01-0377*. Apr. 2021. DOI: 10.4271/2021-01-0377.

[24] J. C. Peyton Jones, K. R. Muske, J. Frey and D. Scholl. "A Stochastic Knock Control Algorithm". *SAE Technical Paper Series 2009-01-1017*. Apr. 2009. DOI: 10.4271/2009-01-1017.

[25] J. C. Peyton Jones, J. M. Spelina and J. Frey. "Likelihood-Based Control of Engine Knock". *IEEE Transactions on Control Systems Technology*. Vol. 21. 6. Nov. 2013, pp. 2169–2180. DOI: 10.1109/tcst.2012.2229280.

[26] D. Bradley, C. Morley, X. J. Gu and D. R. Emerson. "Amplified Pressure Waves During Autoignition: Relevance to CAI Engines". *SAE Technical Paper Series 2002-01-2868*. Oct. 2002. DOI: 10.4271/2002-01-2868.

[27] Y. B. Zeldovich, V. B. Librovich, G. M. Makhviladze and G. I. Sivashinsky. "On the development of detonation in a non-uniformly preheated gas". *Astronautica Acta*. Vol. 15. 1970, pp. 313–321.

[28] Y. B. Zeldovich. "Regime classification of an exothermic reaction with nonuniform initial conditions". *Combustion and Flame*. Vol. 39. 2. Oct. 1980, pp. 211–214. DOI: 10.1016/0010-2180(80)90017-6.

[29] J. Warnatz. "Chemistry of Stationary and Non-Stationary Combustion". *Modelling of Chemical Reaction Systems*. Springer Berlin Heidelberg, 1980, pp. 162–188. DOI: 10.1007/978-3-642-68220-9_12.

[30] G.M. Makhviladze and D.I. Rogatykh. "Nonuniformities in initial temperature and concentration as a cause of explosive chemical reactions in combustible gases". *Combustion and Flame*. Vol. 87. 3-4. Dec. 1991, pp. 347–356. DOI: 10.1016/0010-2180(91)90118-u.

[31] A. E. Lutz, R. J. Kee, J. A. Miller, H. A. Dwyer and A. K. Oppenheim. "Dynamic effects of autoignition centers for hydrogen and C1,2-hydrocarbon fuels". *Symposium (International) on Combustion*. Vol. 22. 1. Jan. 1989, pp. 1683–1693. DOI: 10.1016/s0082-0784(89)80181-x.

[32] D. Bradley. "Burning velocities, markstein lengths, and flame quenching for spherical methane-air flames: A computational study". *Combustion and Flame*. Vol. 104. 1-2. Jan. 1996, pp. 176–198. DOI: 10.1016/0010-2180(95)00115-8.

[33] Y. Ju, H. Guo, K. Maruta and F. Liu. "On the extinction limit and flammability limit of non-adiabatic stretched methane–air premixed flames". *Journal of Fluid Mechanics*. Vol. 342. July 1997, pp. 315–334. DOI: 10.1017/s0022112097005636.

[34] G. T. Kalghatgi and D. Bradley. "Pre-ignition and 'super-knock' in turbo-charged spark-ignition engines". *International Journal of Engine Research*. Vol. 13. 4. Feb. 2012, pp. 399–414. DOI: 10.1177/1468087411431890.

[35] C. Netzer. "Simulation and Assessment of Engine Knock Events". PhD thesis. University of Technology Cottbus - Senftenberg, 2019.

[36] N. Peters. "Mega-knock in super-charged gasoline engines interpreted as localized developing detonation". *4th conference knocking gasoline engines*. IAV Automotive Engineering GmbH, Berlin, 2013, pp. 23–40.

[37] C. Netzer et al. "Engine Knock Prediction and Evaluation Based on Detonation Theory Using a Quasi-Dimensional Stochastic Reactor Model". *SAE Technical Paper Series 2017-01-0538*. Mar. 2017. DOI: 10.4271/2017-01-0538.

[38] A. Gogan, B. Sundén, H. Lehtiniemi and F. Mauss. "Stochastic Model for the Investigation of the Influence of Turbulent Mixing on Engine Knock". *SAE Technical Paper Series 2004-01-2999*. Oct. 2004. DOI: 10.4271/2004-01-2999.

[39] M. Pasternak, F. Mauss, F. Xavier, M. Rieß, M. Sens and A. Benz. "0D/3D Simulations of Combustion in Gasoline Engines Operated with Multiple Spark Plug Technology". *SAE Technical Paper Series 2015-01-1243*. Apr. 2015. DOI: 10.4271/2015-01-1243.

[40] M. Grill, T. Billinger and M. Bargende. "Quasi-Dimensional Modeling of Spark Ignition Engine Combustion with Variable Valve Train". *SAE Technical Paper Series 2006-01-1107*. Apr. 2006. DOI: 10.4271/2006-01-1107.

[41] M. Grill and M. Bargende. "The Development of an Highly Modular Designed Zero-Dimensional Engine Process Calculation Code". *SAE International Journal of Engines*. Vol. 3. 1. Apr. 2010, pp. 1–11. DOI: 10.4271/2010-01-0149.

[42] M. Wenig. "Simulation der ottomotorischen Zyklenschwankungen". PhD thesis. University of Stuttgart, 2013.

[43] Mahir Tim Keskin. *Modell zur Vorhersage der Brennrate in der Betriebsart kontrollierte Benzinselbstzündung*. Springer Fachmedien Wiesbaden, 2016. DOI: 10.1007/978-3-658-15065-5.

[44] M. Bargende. "Ein Gleichungsansatz zur Berechnung der instationären Wandwärmeverluste im Hochdruckteil von Ottomotoren". PhD thesis. Technische Hochschule Darmstadt, 1991.

[45] P. Kožuch. *Untersuchung des Zusammenhangs zwischen thermodynamischen Analysegrößen und optischen Lichtmesssignalen beim DE-Dieselmotor*. Final Report on FVV Project 769. Research Association for Combustion Engines (FVV) e.V. 2001.

[46] C. Bossung, M. Bargende, O. Dingel and M. Grill. "A quasi-dimensional charge motion and turbulence model for engine process calculations". *15th Stuttgart International Symposium*. Springer Vieweg, 2015. DOI: 10.1007/978-3-658-08844-6_68.

[47] C. Bossung. *Turbulenzmodellierung für quasidimensionale Prozessrechnung*. Final Report on FVV Project 1067. Research Association for Combustion Engines (FVV) e.V. 2014.

[48] S. Hann, M. Grill and M. Bargende. "Reaction Kinetics Calculations and Modeling of the Laminar Flame Speeds of Gasoline Fuels". *SAE Technical Paper Series 2018-01-0857*. Apr. 2018. DOI: 10.4271/2018-01-0857.

[49] S. Hann, L. Urban, M. Grill and M. Bargende. "Influence of Binary CNG Substitute Composition on the Prediction of Burn Rate, Engine Knock and Cycle-to-Cycle Variations". *SAE International Journal of Engines*. Vol. 10. 2. Mar. 2017, pp. 501–511. DOI: 10.4271/2017-01-0518.

[50] M. Wenig, M. Grill and M. Bargende. “A New Approach for Modeling Cycle-to-Cycle Variations within the Framework of a Real Working-Process Simulation”. *SAE International Journal of Engines*. Vol. 6. 2. Apr. 2013, pp. 1099–1115. DOI: 10.4271/2013-01-1315.

[51] F. Bozza, V. De Bellis, F. Minarelli and D. Cacciatore. “Knock and Cycle by Cycle Analysis of a High Performance V12 Spark Ignition Engine. Part 2: 1D Combustion and Knock Modeling”. *SAE International Journal of Engines*. Vol. 8. 5. Sept. 2015, pp. 2002–2011. DOI: 10.4271/2015-24-2393.

[52] L. Cai, A. Fandakov, M. Mally, A. Ramalingam and H. Minwegen. *Knock with EGR at full load*. Final Report on FVV Project 6301. Research Association for Combustion Engines (FVV) e.V. 2017.

[53] E. Moses, A. L. Yarin and P. Bar-Yoseph. “On knocking prediction in spark ignition engines”. *Combustion and Flame*. Vol. 101. 3. May 1995, pp. 239–261. DOI: 10.1016/0010-2180(94)00202-4.

[54] A. Fandakov, M. Grill, M. Bargende and A. C. Kulzer. “Two-Stage Ignition Occurrence in the End Gas and Modeling Its Influence on Engine Knock”. *SAE International Journal of Engines 2017-24-0001*. Vol. 10. 4. SAE International, Sept. 2017, pp. 2109–2128. DOI: 10.4271/2017-24-0001.

[55] J.C. Livengood and P.C. Wu. “Correlation of autoignition phenomena in internal combustion engines and rapid compression machines”. *Symposium (International) on Combustion*. Vol. 5. 1. Jan. 1955, pp. 347–356. DOI: 10.1016/s0082-0784(55)80047-1.

[56] A. Fandakov, M. Grill, M. Bargende and A. C. Kulzer. “Investigation of thermodynamic and chemical influences on knock for the working process calculation”. *17th Stuttgart International Symposium*. Springer Fachmedien Wiesbaden, 2017, pp. 107–122. DOI: 10.1007/978-3-658-16988-6_13.

[57] S. Tanaka, F. Ayala, J. C. Keck and J. B. Heywood. “Two-stage ignition in HCCI combustion and HCCI control by fuels and additives”. *Combustion and Flame*. Vol. 132. 1-2. Jan. 2003, pp. 219–239. DOI: 10.1016/s0010-2180(02)00457-1.

[58] G. A. Weisser. “Modelling of Combustion and Nitric Oxide Formation for Medium-Speed DI Diesel Engines: A Comparative Evaluation of Zero- and Three-Dimensional Approaches”. PhD thesis. Swiss Federal Institute of Technology Zürich (ETHZ), 2001.

[59] C. Elmqvist, F. Lindström, H.-E. Ångström, B. Grandin and G. Kalghatgi. “Optimizing Engine Concepts by Using a Simple Model for Knock Prediction”. *SAE Technical Paper Series 2003-01-3123*. Oct. 2003. DOI: 10.4271/2003-01-3123.

[60] D. E. Franzke. “Beitrag zur Ermittlung eines Klopfkriteriums der ottomotorischen Verbrennung und zur Vorausberechnung der Klopfgrenze”. PhD thesis. Technical University of Munich, 1991.

[61] M. Hess, M. Grill and M. Bargende. “0D/1D Knock Criterion to Predict the Knock Boundary of SI Engines”. *6th International Conference on Knocking in Gasoline Engines*. 2022.

[62] K. F. H. M. Steuers. “Cycle-resolved analysis and modeling of knock in a homogeneous charge spark ignition engine fueled by ethanol and iso-octane”. PhD thesis. Swiss Federal Institute of Technology Zürich (ETHZ), 2014.

[63] R. Schießl and U. Maas. “Analysis of endgas temperature fluctuations in an si engine by laser-induced fluorescence”. *Combustion and Flame*. Vol. 133. 1-2. Apr. 2003, pp. 19–27. DOI: 10.1016/s0010-2180(02)00538-2.

[64] R. Schießl, A. Schubert and U. Maas. “Temperature Fluctuations in the Unburned Mixture: Indirect Visualisation Based on LIF and Numerical Simulations”. *SAE Technical Paper Series 2006-01-3338*. Oct. 2006. DOI: 10.4271/2006-01-3338.

[65] L. Zhao et al. “Examining the role of flame topologies and in-cylinder flow fields on cyclic variability in spark-ignited engines using large-eddy simulation”. *International Journal of Engine Research*. Vol. 19. 8. Sept. 2017, pp. 886–904. DOI: 10.1177/1468087417732447.

[66] A. Robert, S. Richard, O. Colin and T. Poinsot. “LES study of deflagration to detonation mechanisms in a downsized spark ignition engine”. *Combustion and Flame*. Vol. 162. 7. July 2015, pp. 2788–2807. DOI: 10.1016/j.combustflame.2015.04.010.

[67] M. Hess, M. Grill, M. Bargende and A. C. Kulzer. "Two-Stage 0D/1D Knock Model to Predict the Knock Boundary of SI Engines". *21th Stuttgart International Symposium*. Springer Fachmedien Wiesbaden, 2021, pp. 514–530. DOI: 10.1007/978-3-658-33466-6_37.

[68] R. Worret, S. Bernhardt, F. Schwarz and U. Spicher. "Application of Different Cylinder Pressure Based Knock Detection Methods in Spark Ignition Engines". *SAE Technical Paper Series 2002-01-1668*. May 2002. DOI: 10.4271/2002-01-1668.

[69] N. Fajt, M. Grill and M. Bargende. "Knock Probability Prediction and its Potential for a Knock Control Application". *6th international conference on knocking gasoline engines*. 2022.

[70] B. n Pla, P. Bares, I. Jiménez, C. Guardiola, Y. Zhang and T. Shen. "A fuzzy logic map-based knock control for spark ignition engines". *Applied Energy*. Vol. 280. Dec. 2020. DOI: 10.1016/j.apenergy.2020.116036.

[71] J. C. Peyton Jones, S. Shayestehmanesh and J. Frey. "A dual-threshold knock controller". *International Journal of Engine Research*. Vol. 18. 8. Nov. 2016, pp. 837–846. DOI: 10.1177/1468087416676756.

[72] S. Shayestehmanesh, J. C. Peyton Jones and J. Frey. "Computing the closed-loop characteristics of a generalized multi-threshold knock controller". *International Journal of Engine Research*. Vol. 19. 9. Oct. 2017, pp. 952–962. DOI: 10.1177/1468087417736693.

[73] X. Shen, Y. Zhang, T. Shen and C. Khajorntraidet. "Spark advance self-optimization with knock probability threshold for lean-burn operation mode of SI engine". *Energy*. Vol. 122. Mar. 2017, pp. 1–10. DOI: 10.1016/j.energy.2017.01.065.

[74] J. C. Peyton Jones, J. Frey and K. R. Muske. "A Statistical Likelihood Based Knock Controller". *6th IFAC Proceedings Volumes*. Vol. 43. 7. July 2010, pp. 809–814. DOI: 10.3182/20100712-3-de-2013.00035.

[75] Y. Y. Ham, K. M. Chun, J. H. Lee and K. S. Chang. "Spark-Ignition Engine Knock Control and Threshold Value Determination". *SAE Technical Paper Series 960496*. Feb. 1996. DOI: 10.4271/960496.

[76] M. Penese, C. F. Damasceno, A. Bucci and G. Montanari. "Sigma® on knock phenomenon control of Flexfuel engines". *SAE Technical Paper Series 2005-01-3990*. Nov. 2005. DOI: 10.4271/2005-01-3990.

[77] N. Fajt, M. Grill, M. Bargende and A. Kulzer. “Knock Frequency based Knock Control”. *SAE Technical Paper Series 2022-01-5043*. 2022. DOI: 10.4271/2022-01-5043.

[78] Gamma Technologies. GT-Suite. 2022. URL: https://www.gtisoft.com/gt-suite.

[79] FKFS Research in Motion. FKFS UserCylinder®. 2021. URL: https://www.fkfs.de/en/competencies/virtual-development/virtual-engine-development.

[80] I. I. Vibe. *Brennverlauf und Kreisprozess von Verbrennungsmotoren*. Berlin: VEB-Verlag Technik, 1970.